SECTION II. TASK 2. SUBMODEL DEVELOPMENT AND EVALUATION

Objectives

The objectives of this task are to develop or adapt advanced physics and chemistry submodels for the reactions of coal in an entrained-bed and a fixed-bed reactor and to validate the submodels by comparison with laboratory scale experiments.

Task Outline

The development of advanced submodels for the entrained-bed and fixed-bed reactor models will be organized into the following categories: a) Coal Chemistry (including coal pyrolysis chemistry, char formation, particle mass transfer, particle thermal properties, and particle physical behavior); b) Char Reaction Chemistry at high pressure; c) Secondary Reactions of Pyrolysis Products (including gas-phase cracking, soot formation, ignition, char burnout, sulfur capture, and tar/gas reactions); d) Ash Physics and Chemistry (including mineral characterization, evolution of volatile, molten and dry particle components, and ash fusion behavior); e) Large Coal Particle Effects (including secondary reactions within the particle and in multiple particle layers; f) Large Char Particle Effects (including oxidation); g) SO_x-NO_x Submodel Development (including the evolution and oxidation of sulfur and nitrogen species); and h) SO_x and NO_x Model Evaluation.

II.A. SUBTASK 2.a. - COAL TO CHAR CHEMISTRY SUBMODEL DEVELOPMENT AND EVALUATION

Senior Investigators - David G. Hamblen and Michael A. Serio
Advanced Fuel Research, Inc.
87 Church Street, East Hartford, CT 06108
(203) 528-9806

Objective

The objective of this subtask is to develop and evaluate, by comparison with laboratory experiments, an integrated and compatible submodel to describe the organic chemistry and physical changes occurring during the transformation from coal to char in coal conversion processes.

Accomplishments

During the past year, work was done on using the set of rank dependent kinetic parameters obtained from low heating rate experiments to predict high heating rate data from pyrolysis experiments in our Transparent Wall Reactor (TWR) and Heated Tube Reactor (HTR). Simulations were also done of high heating rate pyrolysis data from the literature such as the heated grid experiments of Gibbins, the wire grid experiments of Fong and coworkers of MIT, and the TWR experiments of Fletcher at Sandia.

Work continued on testing the fluidity model in conjunction with the changes in the FG-DVC model discussed above. For certain coals, such as Illinois No. 6 and Pocahontas, it is difficult to provide very good fits to both the fluidity and pyrolysis data. The fluid behavior of low rank coals which soften when heated to very high heating rates was also not well predicted. However, we have achieved excellent agreement with the majority of data obtained so far.

Work also continued on the swelling model. The changes in the FG-DVC model discussed above result in better predictions of the Free Swelling Index (FSI) for the majority of coals. There are still problems in fitting the FSI for the Pocahontas coal, which has a high FSI and a low Geissler fluidity. A single bubble version of the swelling model was developed for comparison to data on the

Pocahontas coal, which is the most difficult coal to model with respect to the swelling behavior at high heating rates. A numerical problem which made the predictions sensitive to the size of the time step was fixed. This gave better swelling predictions for the Pocahontas coal, which had been the most difficult case, but somewhat worse predictions for Pittsburgh. A possible solution may be to adjust the gas diffusivity or include a nonuniform bubble wall thickness.

Work was nearly completed on a version of the swelling model for integration into PCGC-2. The model is actually a submodel of FG-DVC since it uses information from this model as well as a second submodel for coal fluidity. The primary inputs to the model are the initial particle size, initial bubble size, time-temperature history, gas evolution rate (from FG-DVC), and the viscosity. The primary outputs are the particle size due to swelling and the porosity. The model parameters are the initial bubble size, gas diffusivity, critical wall stress, and surface tension.

During the past year, work was also done on using the FG-DVC model to simulate mild gasification processes. The model was modified to include a hydrocarbon cracking routine which describes the cracking of long chain paraffin and olefin species down to smaller hydrocarbons (C_1-C_3's). The model was applied to data obtained from pyrolysis of Illinois No. 6 coal in the IGT mild gasification Process Research Unit (PRU) under essentially isothermal conditions.

Work continued on the sulfur and nitrogen submodel. The first step was to run the series of Argonne coals in the TG-FTIR apparatus with the post-oxidizer attached. This allows detection of species that are not easily detected in the IR, such as H_2S (oxidizes to SO_2). Runs have now been done with all eight Argonne coals in the TG-FTIR system using the post-oxidizer attachment and a wide-band MCT detector (in order to measure HCN).

The preliminary data from the Argonne coals suggest that the ratio of NH_3/HCN is much higher than what is observed in pyrolysis at higher temperatures. However, most of the previous data has been taken in systems where secondary cracking of the tar to produce HCN is a possibility. Most of the current models for NO_x formation assume the coal nitrogen is volatilized as HCN rather than HCN, so this is an important question. The calibrations for both NH_3 and HCN are being redone in order to verify these data.

During the past year, a quantitative char reactivity submodel was developed. After examination of several possible approaches, a decision was made to use the Random Pore Model of Bhatia and Perlmutter to describe the reaction under the kinetic control regime. Compared to other possible approaches, such as those of Gavalas or Simons, it is mathematically simpler (fewer parameters) and has been tested against a wider variety of data. It is able to describe the variation of surface area with conversion based on an analytical expression with a single adjustable parameter which describes the initial pore structure. The recent progress has been in fitting the reactivity model to both isothermal and non-isothermal data for chars produced from the Argonne coals and developing a set of values for the kinetic rate parameters (A, E_o, σ), the active site concentration (β) and the char structural parameter (Ψ) for the random pore model. Reactivity experiments were done on various chars in order to further develop the model. Based on the results of these experiments, a decision was made to use the Random Pore Model for medium and high rank coals (reactivity dependent on internal surface area) and a volumetric model for low rank coals (catalytic reaction). In order to complete the reactivity model, an estimate of the active site concentration, β, is required. A relationship was developed to describe the functional form of the active site concentration, β, with respect to changes in coal rank, mineral content, and the degree of pyrolysis. This relationship was based on measured values of the reactivity index, T_{crit}, obtained for a range of coals (Zap lignite, Montana Rosebud subbituminous, Illinois bituminous, and Pittsburgh bituminous) from a variety of pyrolysis experiments where measurements of the char elemental composition were also made. Subsequently, these correlations were incorporated into two separate expressions (one for high rank and one for low rank coals) for reactivity (dX/dt) which depend on temperature, char hydrogen concentration (H_{char}), coal oxygen concentration (O_{coal}), and the concentration of organically dispersed calcium (Ca_d).

A table of optical properties for pulverized sized-coal particles was sent to BYU for a sensitivity analysis of PCGC-2 to the optical properties values. The results from the study at BYU suggest that there is no need for a detailed submodel in PCGC-2 for coal optical properties.

FG-DVC Model

During the past year, work was done on using the set of rank dependent kinetic parameters obtained from low heating rate experiments to predict high heating rate data from pyrolysis experiments in our Transparent Wall Reactor (TWR) and Heated Tube Reactor (HTR). Simulations were also done of high heating rate pyrolysis data from the literature such as the heated grid experiments of Gibbins, the wire grid experiments of Fong and coworkers of MIT, and the TWR experiments of Fletcher at Sandia.

Some problems were obtained in predicting the changes in the tar yield and tar molecular weight distributions with heating rate for low rank coals using the current version of the model. In addition, we could not predict the extractables yields for the high heating rate data of Fong and coworkers on the Pittsburgh Seam coal with the current kinetic parameters. It was decided to re-examine the assumptions on the model input parameters, such as 1) the bridge breaking rate, 2) the crosslinking efficiencies, 3) the tar vaporization law, and 4) the ΔP parameter. It was found that a modest change in the activation energy for the bridge breaking rate (from 25 to 27 kcal/mole) allowed for good predictions of the Fong data. Changes in the crosslinking efficiencies were thoroughly evaluated and found to be largely unnecessary. A decision was made to use 10^{14} sec^{-1} for the bridge breaking pre-exponential and values of the crosslinking efficiencies = 1. The final set of rank dependent parameters is summarized in Table II.A-1 of the 18th Quarterly Report.

The effects of the tar vaporization law and the ΔP parameter were found to be very important. The change in the original vaporization law from the expression proposed by Suuberg to a factor of 10 higher was found to be mainly responsible for the inability to predict the high heating rate Zap data. By changing to Suuberg X1, and allowing ΔP to be the sole adjustable parameter, the predictions are much better. A decision was initially made to use the law proposed by Fletcher, since it had been subjected to a rather thorough validation with model compounds. However, in the intermediate molecular weight range where the model is sensitive to the vaporization law, the two models are comparable. Therefore, either Fletcher or Suuberg XI can be employed. The main unresolved question is the appropriate choice for ΔP and how this could be functionalized. It appears that the model predictions of the FIMS data are very sensitive to the

choice of this parameter. At low heating rates, a choice of $\Delta P = 0$ gives the best prediction of the tar yield. A choice of $\Delta P = 0.2$ gives the best prediction of the tar MWD. Possible solutions would be to: 1) parameterize Δ; 2) improve the description of the external transport of tar to resolve the problem of the higher molecular weight tars coming out earlier than expected. It was decided that it was best to use ΔP as an adjustable parameter of the model. The other choice was to develop a new external transport model for tar. This was not thought to be the best option at this stage of the contract.

The process of defining the deliverable submodels was completed during the past month. Under this subtask, submodels will be completed for swelling, sulfur and nitrogen evolution, char reactivity and optical properties. The swelling model is an extension of the recently completed fluidity model.

Mild Gasification

During the past month, work was done on using the FG-DVC model to simulate mild gasification processes. The model was modified to include a hydrocarbon cracking routine which describes the cracking of long chain paraffin and olefin species down to smaller hydrocarbons (C_1-C_3's). The model was applied to data obtained from pyrolysis of Illinois No. 6 coal in the IGT mild gasification Process Research Unit (PRU) under essentially isothermal conditions. The PRU is a combination of a fluidized-bed and an entrained-bed reactor operated at temperatures from 1000-1400 °F (550-750 °C) and pressures close to atmospheric. A schematic of the IGT PRU is shown in Fig. II.A-1. Simulations were also done of pyrolysis data from a two-stage circulating bed reactor at Battelle obtained at temperatures from 1200-1650 °F (650-900°C), ~ 1 atm pressure, also for Illinois No. 6 coal. A schematic of the Battelle system is shown in Fig. II.A-2. In general, good agreement was obtained for the effect of temperature on the yields of char and gas, as shown in Figs. II.A-3 and II.A-4 for the IGT and Battelle data, respectively. In the case of the tar, the model did not predict the fall-off in the tar yield at high temperature (> 1200 °F) for the IGT data. However, the Battelle data did not show this fall-off in the tar yield and were in good agreement with the model predictions for tar, gas and char.

A parameter in the model was the gas-phase residence time. A value of 2 sec. was used for the IGT reactor; while a value of 0.8 sec. was used for the

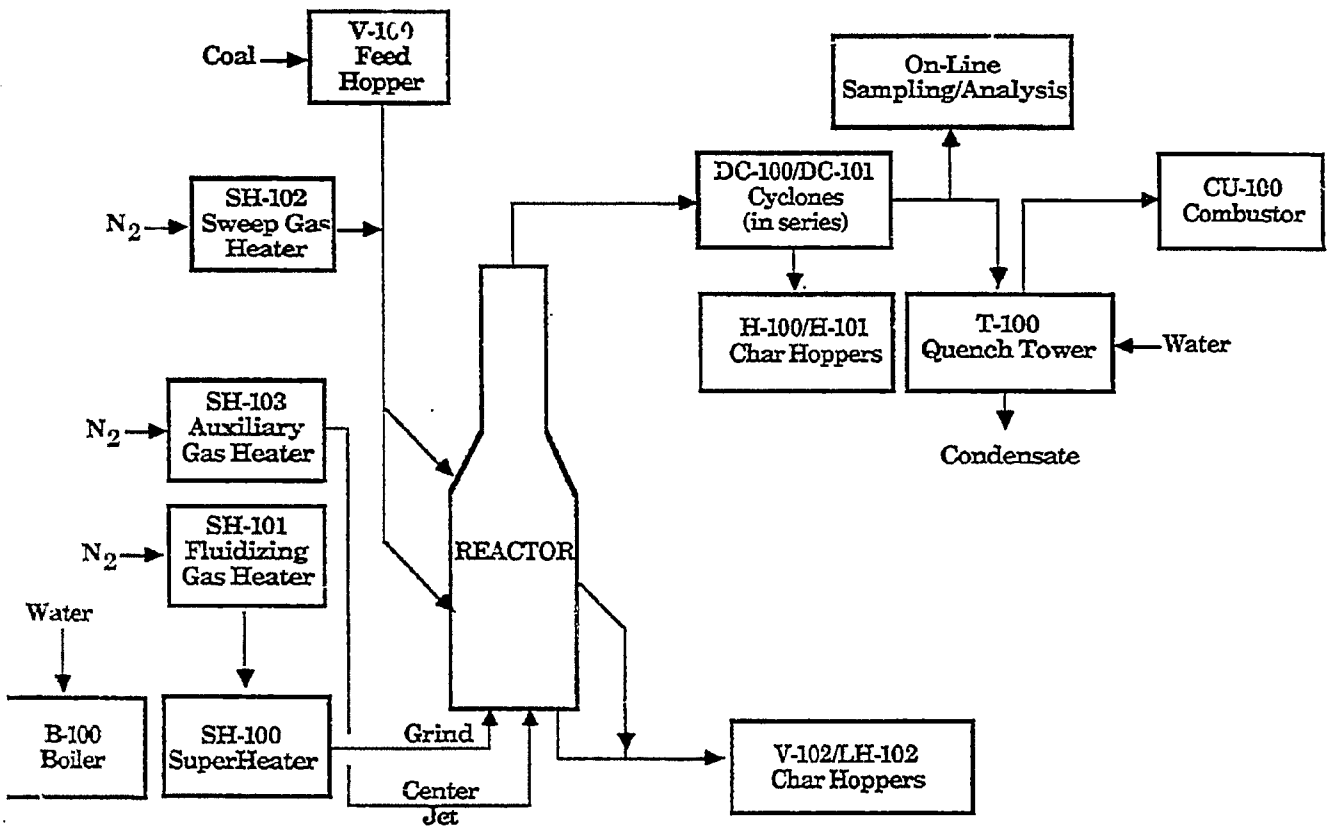

Figure II.A-1. Schematic Diagram of PRU System at IGT.

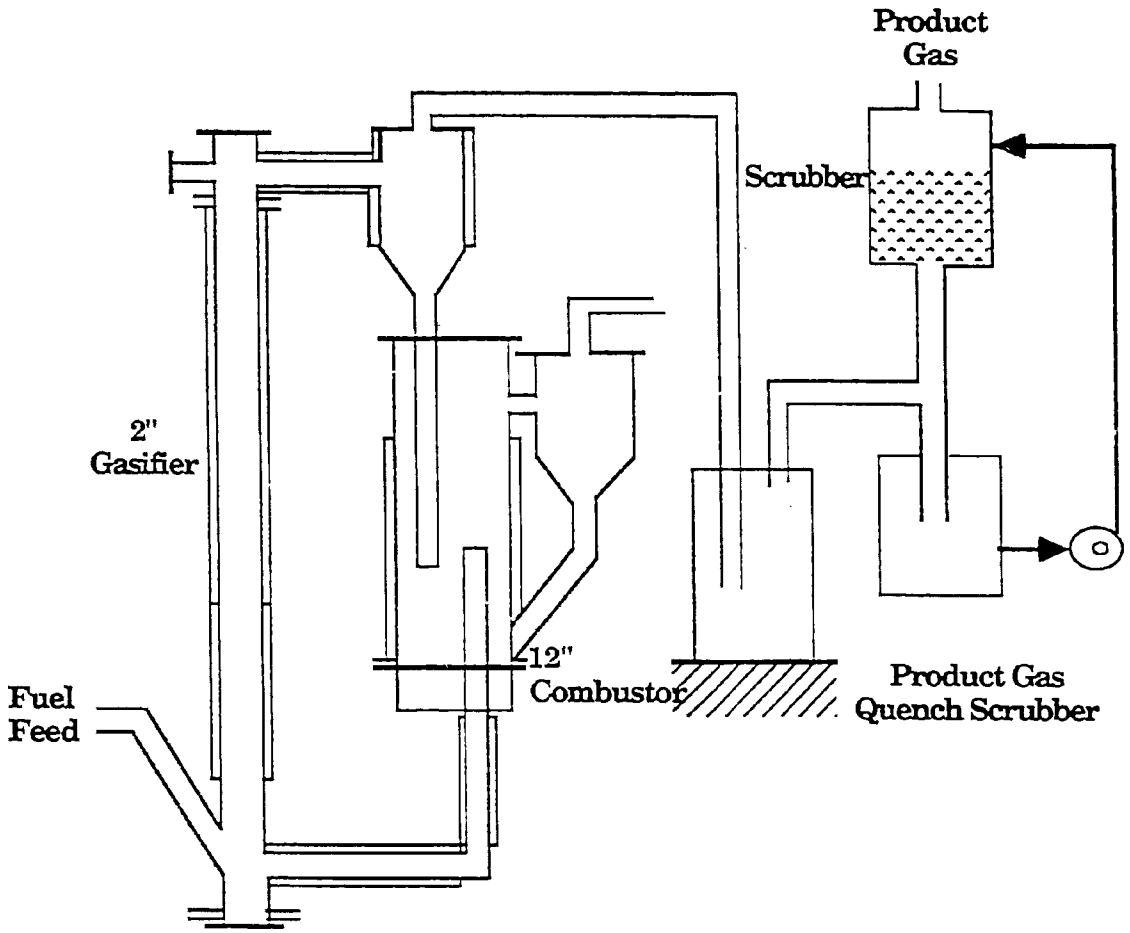

Figure II.A-2. Battelle Small, Integrated Gasification Unit.

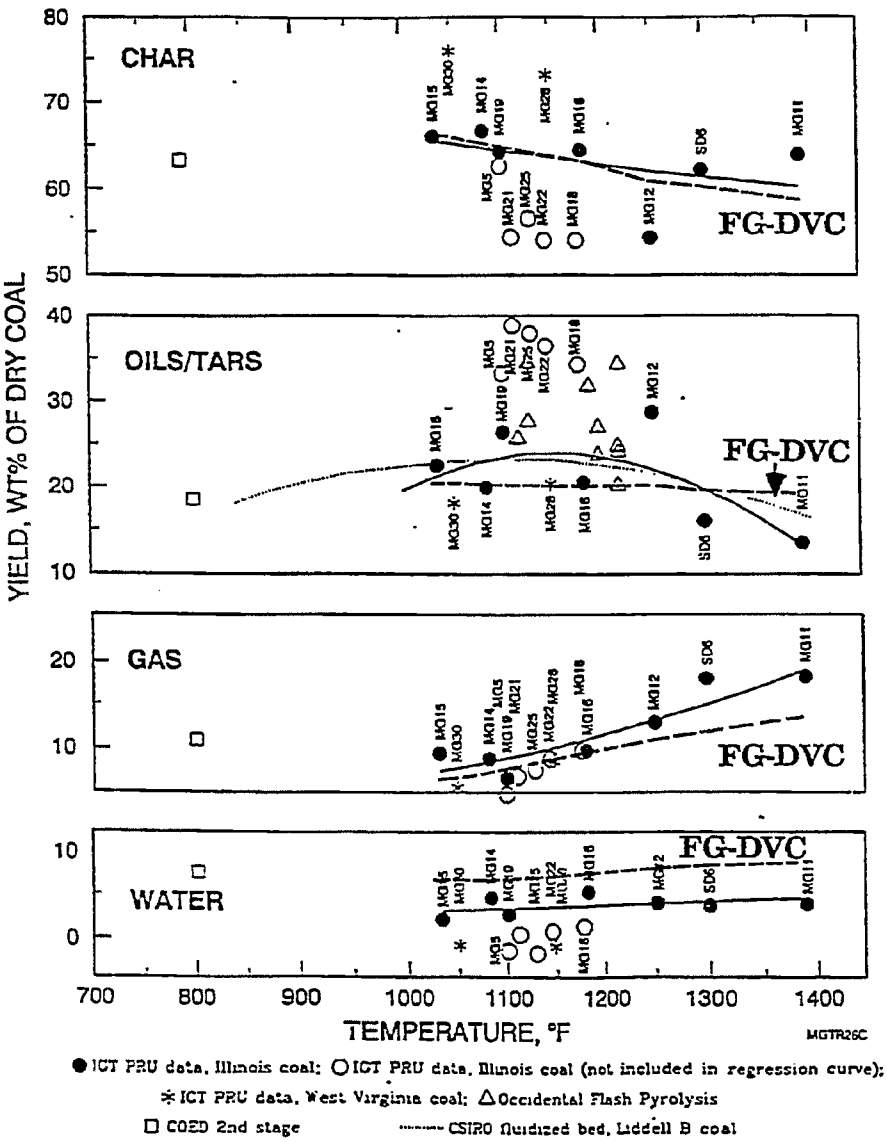

Figure II.A-3. Comparison of FG-DVC Mild Gasification Model Predictions (--) and Experimental Data from IGT for Overall Product Yields.

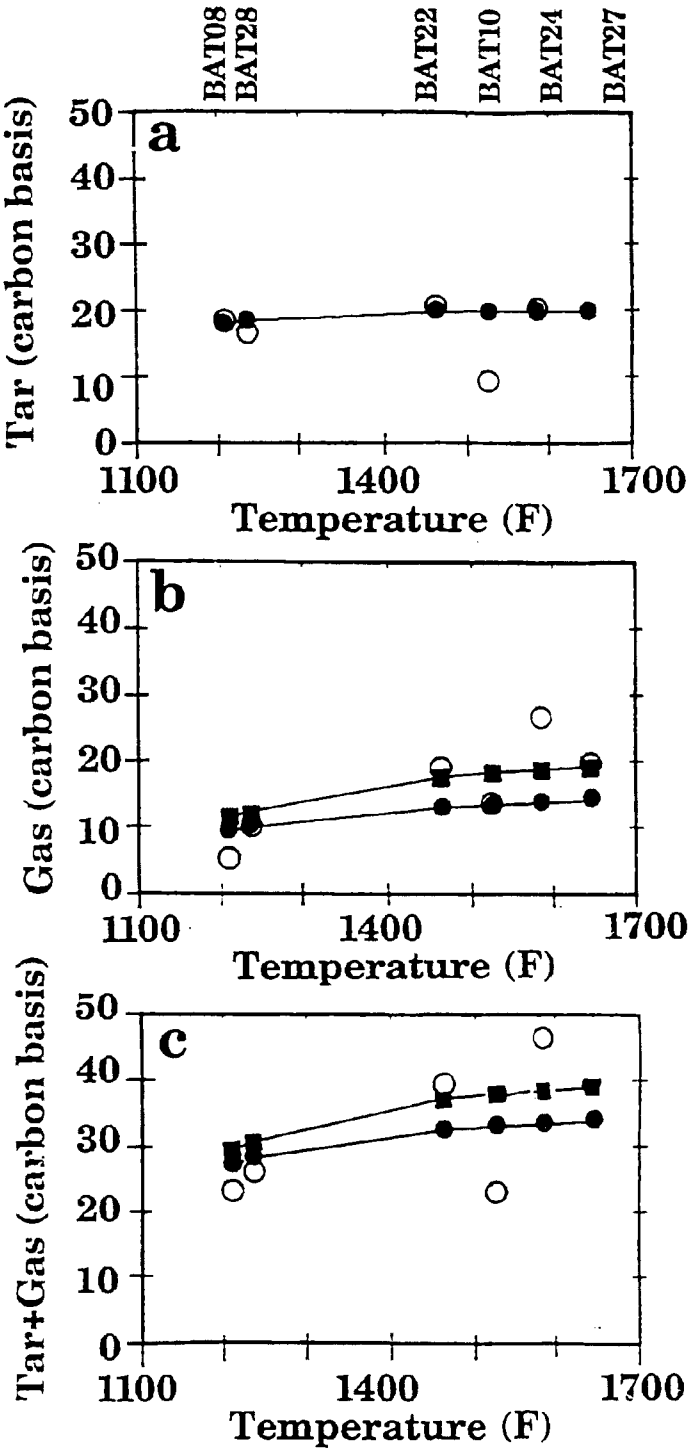

Figure ILA-4. Comparison of Standard (●-●) and Equilibrium (■-■) FG-DVC Mild Gasification Model Predictions and Experimental Data from Battelle (o).

Battelle reactor. These values were based on estimates of the gas hold up in the system provided by the respective companies. The average solids residence time was in the range of 20-30 minutes for the IGT system and - 1 sec. for the Battelle reactor.

In the case of individual gases, good agreement was obtained for H_2, CH_4, C_2's and CO data from the IGT PRU (see Fig. II.A-5). The amount of CO_2 was somewhat underpredicted (see Fig. II.A-5b). Better agreement was obtained using a partial equilibrium model for the gas phase. Data on individual gas species yields were not available from the Battelle study.

Fluidity Model

The work on the fluidity model was nearly completed. The first draft of a paper was also completed.

Swelling Model

Model Validation

An outline of the swelling submodel which includes the inputs, outputs and key model parameters is given in Figure II.A-6. An issue that needs to be addressed is how the swelling behavior is affected by the presence of oxygen.

In order to validate the model, swelling data on chars from work done at AFR and elsewhere was compiled. SEM photographs were obtained for chars produced in entrained flow reactor (EFR) experiments at 700 °C. These are being compared to model predictions.

A single bubble version of the swelling model is now being developed for comparison to data on the Pocahontas coal, which is the most difficult coal to model with respect to the swelling behavior at high heating rates. The basis for the problem is that the fluidity for the Pocahontas coal was predicted to decline at high heating rates, which is not the case for the other Argonne coals and which is not consistent with the swelling data.

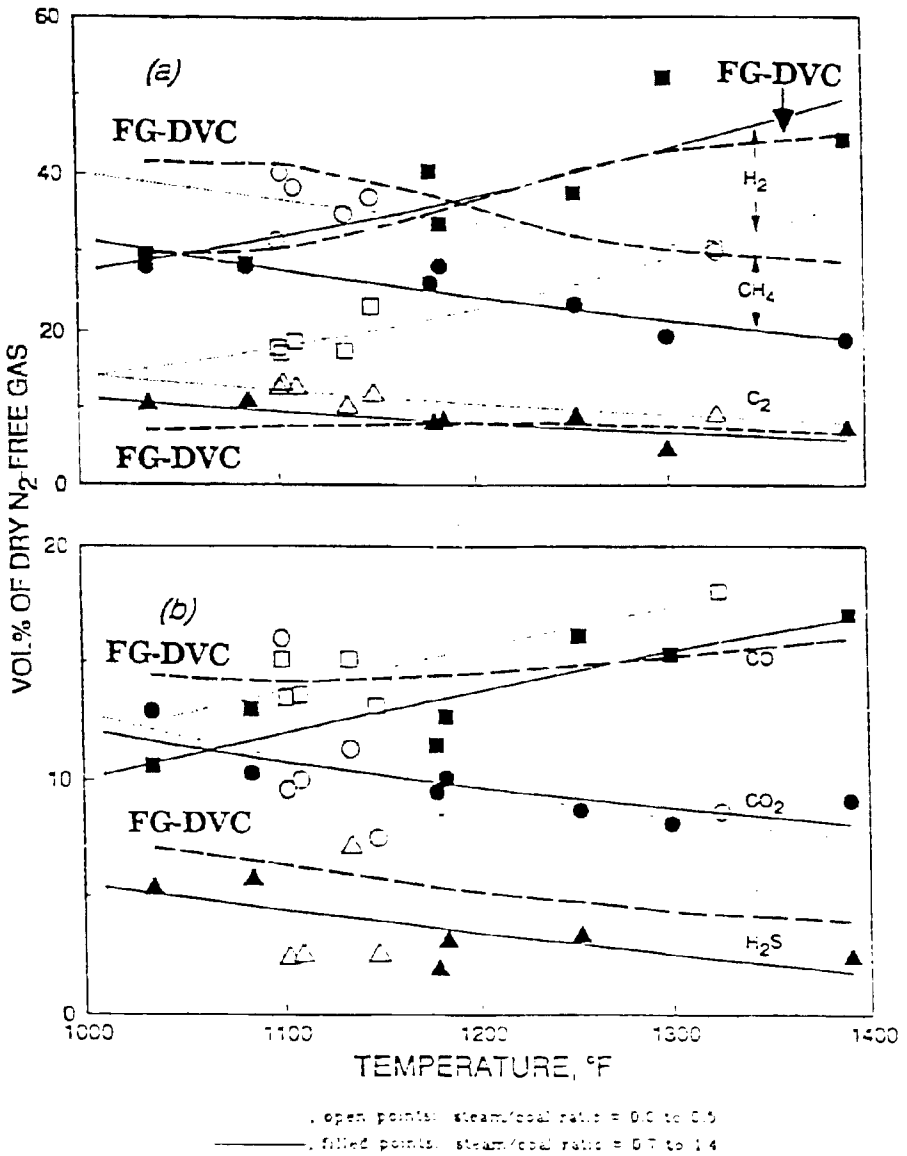

Figure II.A-3. Comparison of FG-DVC Mild Gasification Model Predictions (--) and Experimental Data from IGT for Individual Gas Product Yields.

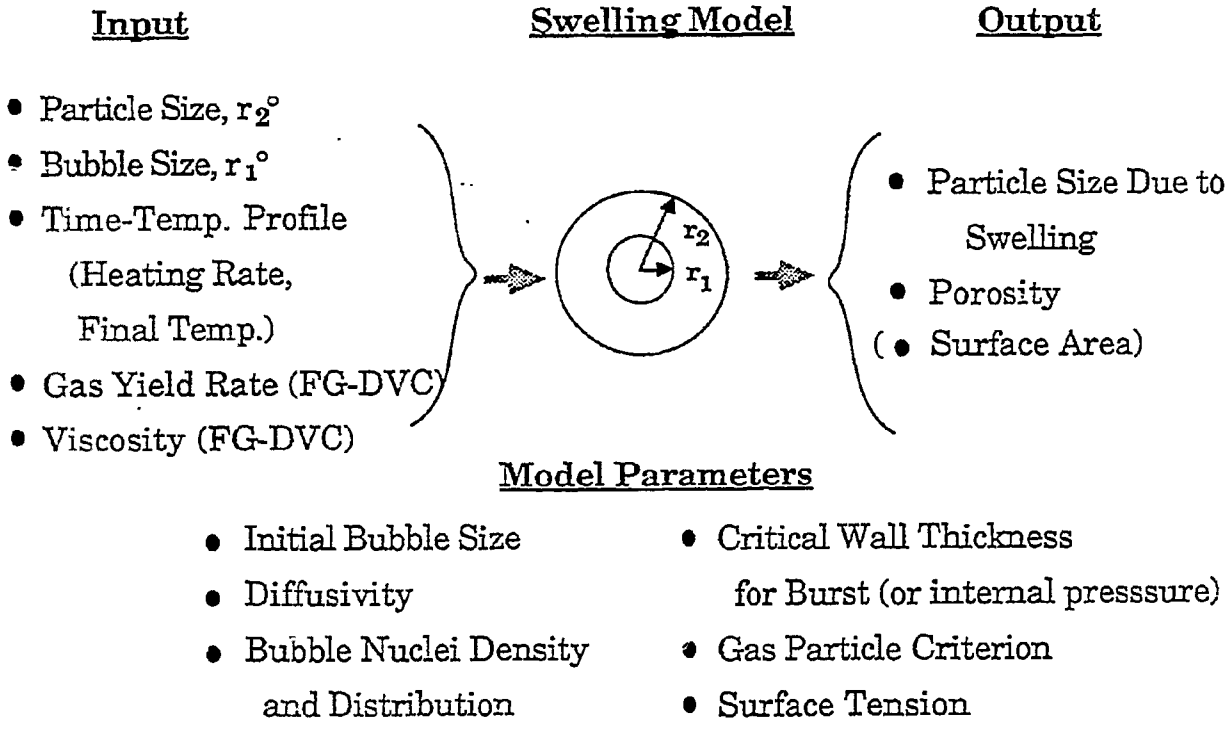

Figure II.A-6. Outline of Particle Swelling Submodel

One solution was to adjust the kinetic rates for bridge breaking and crosslinking which are important in the onset and decay of fluidity. However, this approach was constrained by simultaneously fitting the pyrolysis data. A more successful approach was to change the partition of CH_4 into loose and tight pools. By shifting more CH_4 into the loose pool (out of the tight pool) the fluidity predictions were reasonable (no decline at high heating rates). However, the amount of swelling was still underpredicted under this conditions. It appears that it is necessary to introduce a delay into the swelling model, so that there is more time for the bubble to stretch out during the period of high fluidity. When a change was introduced into the model which delayed the drop in fluidity from its peak value, an improvement was observed in the comparison of the swelling predictions to the data. However, the required delay was too long to be realistic. We briefly investigated the possibility of a non-Newtonian behavior of the coal liquid, which behavior is not unexpected (van Krevelen, 1976) and has been observed at high shear rates for coal liquid (Waters, 1962). It is an option that we choose not to include at this time.

It was later found that at high heating rates the coal stayed fluid for only a short time. If the time-step of our model was too large, the model could step over the window of fluidity without properly accounting for it. Changing to smaller time steps, until a still smaller time step produced no observable change, gave predictions of swelling more in line with observed values.

Swelling Submodel for PCGC-2

Work was nearly completed on a version of the swelling model for integration into PCGC-2. The model is actually a submodel of FG-DVC since it uses information from this model as well as a second submodel for a coal fluidity, as shown in Fig. II.A-6. The model uses the gas collection rate inside a bubble to calculate the internal bubble pressure which is then used to calculate the rate of expansion of the bubble and the swelling ratio of the particle. The model is sensitive to the assumptions of the gas diffusivity in the melt and the initial bubble radius. Experimental data from AFR and the literature will be used to guide the choice of reasonable values for these parameters. The primary inputs to the model are the initial particle size, initial bubble size, time-temperature history, gas evolution rate (from FG-DVC), and the viscosity. The primary outputs are the particle size due to swelling and

the porosity. The model parameters are the initial bubble size, gas diffusivity, critical wall stress, and surface tension. The model does not predict the internal surface area since this is primarily in the micropores and the net surface area in these pores does not change much from swelling.

Relationship of Swelling to Char Reactivity

Char reactivity depends on active surface area. This section deals with the question of the relationship between swelling and reactivity, via surface area. It is a chronicle of reasons why a thorough knowledge of char swelling will not lead to predictions of reactivity.

From the point of view of experiment, Zygourakis (1989) has examined sectioned chars microscopically, using image processing techniques to deduce porosity, swelling, and surface area. His optical technique has resolution only down to 0.5 μm, and with this he deduces a maximum surface area of about 0.08 m^2/cc of particle. But this is two orders of magnitude less than those measured by BET and other gas adsorption techniques (Gan et al., 1972). Consequently, it is concluded that most of the surface area of a char is in micropores. However, the swelling model predicts no swelling for pores as small as micropores, as gas collection is low and the surface tension is high. Therefore, swelling cannot be a direct major factor in the development of pore surface area or reactivity.

Sulfur and Nitrogen Submodel

An outline of the sulfur and nitrogen submodel is shown in Figure II.A-7. The sulfur and nitrogen evolution submodel is essentially already part of the FG-DVC model. What is needed is a set of species evolution data from pyrolysis experiments with the Argonne coals for model validation. This work is being done in a TG-FTIR apparatus which has been outfitted with a special detector for this purpose and which has a post-oxidizer attachment. The post-oxidizer converts H_2S to SO_2, the latter of which has a much stronger IR absorbance. Runs have now been done with all eight Argonne coals in the TG-FTIR system using the post-oxidizer attachment (in order to measure H_2S) and a wide-band MCT detector.

The preliminary data from the Argonne coals suggests that the ratio of NH_3/HCN is much higher than what is observed in pyrolysis at higher temperatures.

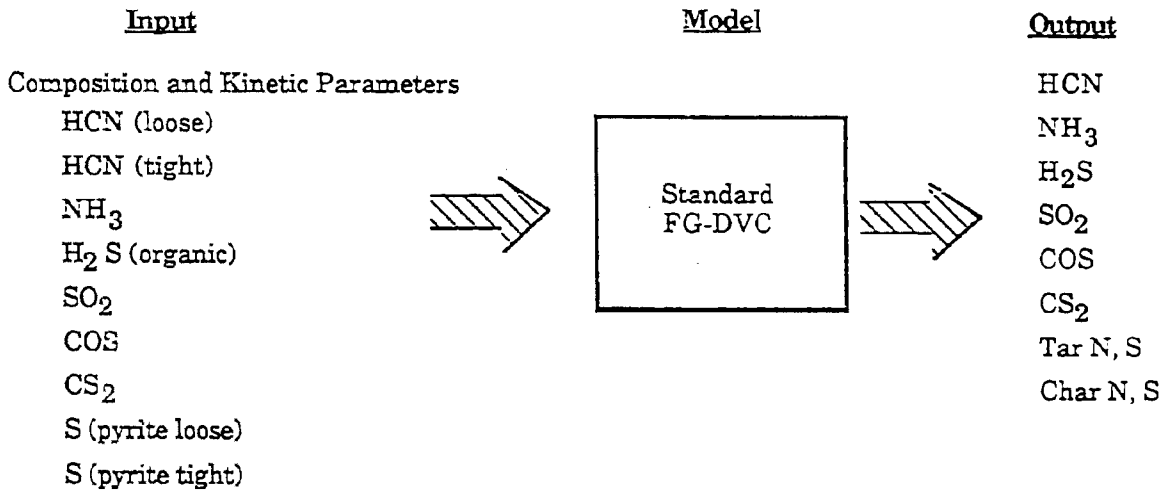

Figure II.A-7. Outline of Sulfur And Nitrogen Submodel

However, most of the previous data has been taken in systems where secondary cracking of the tar to produce HCN is a possibility. Most of the current models for NO_x formation assume the coal nitrogen is volatilized as HCN rather than HCN, so this is an important question. The calibrations for both NH_3 and HCN are being redone in order to verify these data.

Both the HCN and NH_3 evolutions show a consistent variation with rank. For NH_3, there are two distinct peaks. The low temperature peak is believed to result from decomposition of amine groups. The source of the high temperature peak is unknown, but it could be a secondary reaction product resulting from ring decomposition and condensation reactions since it occurs in the temperature range where hydrogen is evolved.

As discussed above, the relatively large amount of NH_3 for these low heating rate experiments was surprising since HCN is the dominant product in high heating rate experiments. This result suggests that the HCN found in the latter experiments may be a secondary product from tar cracking. An experiment was done to test this idea by the use of a post-pyrolysis zone. In this case, some additional HCN was formed from tar cracking while the NH_3 evolution was largely unchanged. Because of the importance of the NH_3/HCN question with respect to the pollutant submodels in PCGC-2, additional experiments will be done to control the opportunity for secondary reactions.

Optical Properties

An outline of the proposed optical properties submodel is shown in Figure II.A-8. In the case of the optical properties submodel, it is not clear yet how much impact this model will have on the predictions of PCGC-2. Consequently, a sensitivity analysis is now underway. The optical properties for different size particles of Zap lignite were calculated and sent to BYU for input into PCGC-2. The results from the study of BYU suggest that there is no need for a detailed submodel in PCGC-2 for coal optical properties.

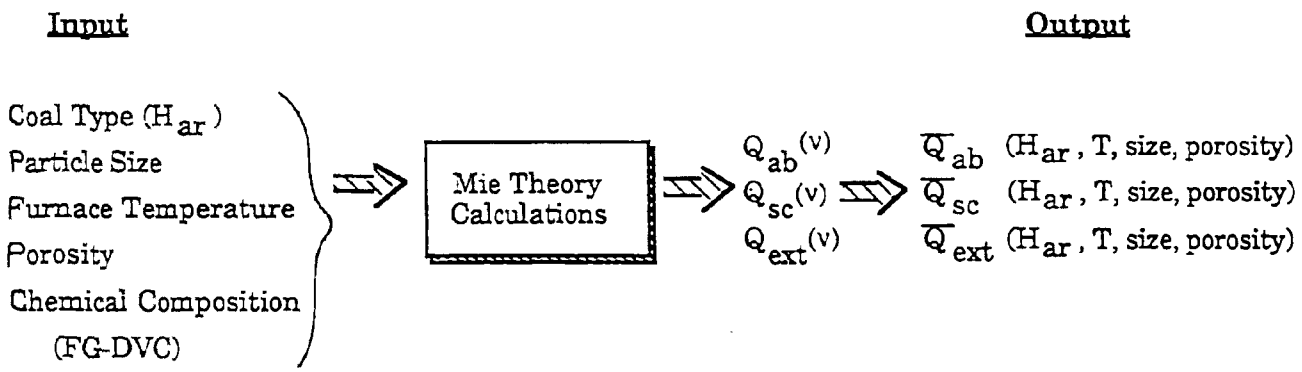

Figure II.A-8. Outline of Submodel for Optical Properties of Coals and Chars.

Char Reactivity

Objective of the Model

The objective of the char reactivity model is to develop a submodel of the FG-DVC model to describe the initial reactivity and burnout of char particles. The burnout of the char often dictates the overall time scale for many practical combustion and gasification systems. In the case of a fixed-bed reactor the char reactivity will dictate the location of the maximum temperature zone. In the case of mild gasification, the production of a highly reactive char can be critical to the success of a process. An outline of the model is shown in Fig. II.A-9.

In order to accurately describe char reactivity, one must be able to account for the effect of 1) rank; 2) degree of pyrolysis; 3) char burnoff; 4) minerals and 5) char morphology. The relative effect of those factors may be different for various coals and various conditions, and are usually difficult to estimate accurately. However, we can differentiate the effect of rank and degree of pyrolysis, which can have an impact on the maximum value of the reactivity, from the changes in reactivity with char burnoff. It is believed that minerals and char morphology have an effect on both the maximum value and the degree of change in reactivity with burnoff. From the accumulated data obtained at AFR and by others, it is concluded that:

- For all coals, the degree of pyrolysis (obtained from different heat treatment temperatures or heating rates) affects the molecular order of the char, and consequently the maximum reactivity. The more severe treatments decrease reactivity.

- For high rank coals, changes in reactivity as a function of burnoff are dependent on changes in available surface area and/or the distribution of active sites. The amount of initial surface area does not, however, always correlate with the reaction rate, which means that other factors (molecular order for example) have proportionally more impact on reactivity than surface area.

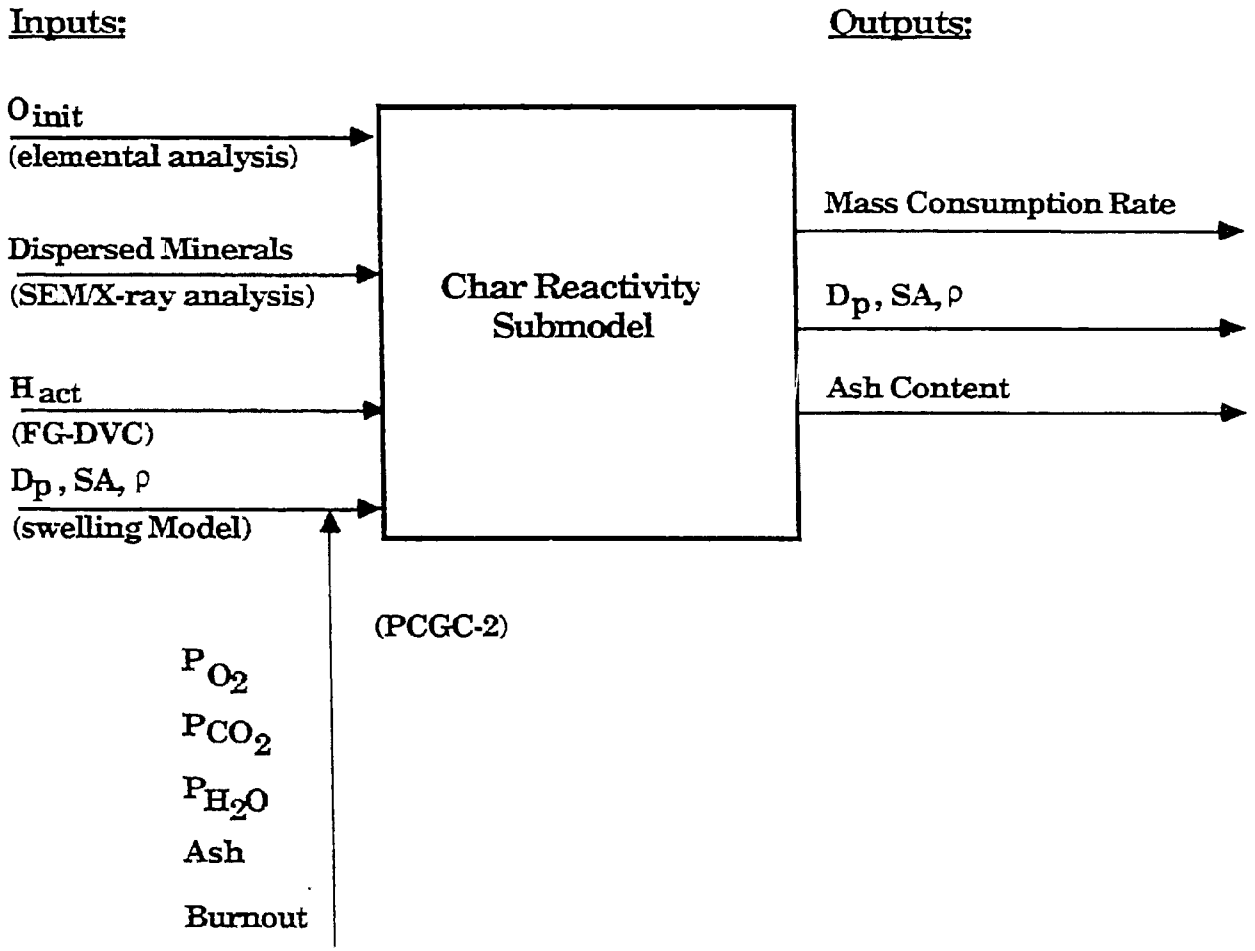

Figure II.A-9. Outline of Char Reactivity Submodel.

- For low rank coals, changes in catalytic activity, and not in surface area, are the major factors influencing reactivity as a function of burnoff. The magnitude of the initial reactivity is also a strong function of catalytic content, and does not depend strongly on total available surface area.

The reactivity model that is being developed will account for these effects. For high rank coals, the predictions of the changes in surface area versus burnoff will be obtained using a Random Pore Model. For low rank coals, the intrinsic reactivity is primarily dependent on catalytic effects and a simple volumetric model is used. Potential changes in activation energy with burnoff due to a change in the active site distribution will also be considered if necessary.

Features of the Model

The char reactivity model will be integrated with the FG-DVC model, which has the information on the starting coal oxygen concentration and the char hydrogen concentration. These are important parameters in determining char reactivity. The other ingredients in this model are a description of the mineral contribution to reactivity and the char morphology. Incorporating the internal pore structure of the char into a model is the most difficult and least understood aspect of char reactivity.

During Phase I of this program, extensive characterizations were performed on char reactivity and its relationship to coal rank, heating rate, extent of pyrolysis and mineral constituents. This work has suggested that a model with the input/output structure shown in Fig. II.A-9 would be appropriate. The desire is to relate the char reactivity to properties of the starting coal and quantities that can be predicted by the FG-DVC model and the viscosity and swelling models.

The actual hydrogen (H_{act}) content of the char has been found to be a good predictor of the effects of annealing on char reactivity. This quantity can be obtained directly from the FG-DVC pyrolysis model. For low rank coals (above 10% O content), the dispersed ion-exchanged calcium (Ca_d) content was found to be a good predictor of the effects of minerals on char reactivity. This can be input

from SEM/x-ray analysis of the starting coal. Other highly dispersed minerals which may be important contributors to reactivity for coals outside the Argonne set can also be obtained by this analysis.

For high rank coals (below 10% O content), the degree of ordering of the coal is an important parameter. This is well predicted by the starting oxygen concentration (O_{init}) obtained from an elemental analysis. The above three parameters (H_{act}, Ca_d, O_{init}) will provide a good description of reactivity up to about 50% burnout. The prediction of higher levels of burnout will be part of the remaining work and will depend on reactivity data on chars collected from coal flame experiments which have not yet been fully analyzed.

A second part of the remaining research is how to incorporate a description of the char morphology into the reactivity model. The current PCGC-2 code does not explicitly account for pore diffusion effects which are important under many practical combustion and gasification conditions. For fluid coals, the char swelling submodel will provide predictions of the porosity which can be input into the reactivity submodel.

Other effects, which can be considered second order, include the combined effects of fluidity and pyrolysis heating rate on char reactivity. This can be important for certain highly fluid coals such as the Upper Freeport and Pittsburgh.

The model will explicitly predict the reactivity to O_2 and CO_2. The reactivity of H_2O can be approximated to be the same as CO_2. The reactivity of H_2 is sufficiently low to be negligible except for very high pressure processes and will not be considered.

Predictions of Changes in Reactivity with Burnoff

Random Pore Model Description (kinetic control, high rank coals) - The modeling of the reaction rate as a function of burnoff for high rank coals is based on the Random Pore Model of Bhatia and Perlmutter (1980) and Gavalas (1980). This model predicts the reaction rate and the available surface area as a function of burnoff. Several studies (Mahajan et al. (1978), Tseng and Edgar (1984) have previously shown that, for the same char, burnoff versus time plots

for different conditions (temperature, oxygen pressure) can be normalized into a single characteristic curve which depends only on the physical structure of the char. Rate variations are then simply controlled by physical structural changes during reaction. The random pore model estimates those structural changes by assuming an arbitrary pore size distribution in the reacting solid. The reaction surface is considered as the result of the random overlapping of a set of cylindrical surfaces of a certain size distribution. As a function of burnoff, the reaction surface initially exhibits an increase due to growing surfaces, and later a decrease because of intersections and overlapping surfaces. The initial distribution of the pores is represented by one parameter Ψ which is itself a function of the structural parameter S_o (pore surface area), L_o (pore length), and ϵ_o (porosity). Theoretically, Ψ can be determined experimentally through measurements of S_o, L_o and ϵ_o. However, due to possible uncertainties in the evaluation of these values, Ψ controls the value of the maximum reaction surface, and its position as a function of burnoff.

The reaction rate, following Bhatia and Perlmutter, can be expressed as:

$$\frac{dX}{dt} = \left(\sum_i A_i \exp\frac{-E_i}{RT}\right)(1-X)\, S_o \frac{1}{1-\epsilon_o}\, \sqrt{1-\psi \ln(1-X)}$$

or

$$\frac{dX}{dt} = A \exp\frac{-E}{RT}(1-X)\, S_o \frac{1}{1-\epsilon_o} \sqrt{1-\psi \ln(1-X)} \qquad \text{(II.A-1)}$$

With X = burnoff, S_o = reaction surface in cm^2/cm^3 at burnoff X = 0. Using this formulation, the reaction surface area, S, at conversion, X, is equal to:

$$S = S_o \frac{1}{1-\epsilon_o} \sqrt{1-\psi \ln(1-X)} \qquad \text{(II.A-2)}$$

This model assumes no significant closed pore volume and no diffusional resistance. It is used to represent combustion under chemical reaction controlled conditions (zone I). An extension of this study, done by the same authors (Bhatia and Perlmutter, 1981), presents numerical calculations of reaction rate under boundary layer, intraparticle and product layer diffusional resistance control.

Volumetric model (kinetic control, low rank coals) - For low rank coals, the volumetric model gives the rate

$$\frac{dX}{dt} = \left(\sum_i A_i \exp\frac{-E_i}{RT}\right)(1-X)\, S_o\, \frac{1}{1-\epsilon_o}$$

or

$$\frac{dX}{dt} = A \exp\frac{-E}{RT}(1-X)\, S_o\, \frac{1}{1-\epsilon_o} \qquad \text{(II.A-3)}$$

The factor $\frac{1}{1-\epsilon_o}$ was introduced to be consistent with the random pore model.

Comparison of the Pore Model with Literature Data - The main concern in using literature data is to make sure that it was taken in the kinetic regime, since the random pore model is only valid under those conditions. Using data carefully obtained in that regime (or at least minimizing diffusion limitations by choosing an appropriate reaction temperature, oxygen pressure and char amount), several authors have tested the model. In all cases, the technique used was to model the mass loss using TGA (thermogravimetric analysis). Bhatia and Perlmutter (1980) carried out preliminary testing by fitting the experimental data of Hashimoto and Silveston (1973).

Miura and Silveston (1989) compared different models, including Bhatia's Random Pore Model, a volumetric reaction model and a grain model. They concluded that the Random Pore Model provided the best fit for non-isothermal char oxidation data of a demineralized bituminous coal (taken at low temperature to be in the kinetic regime) at different heating rates. They obtained values of Ψ in the range of 10 to 30.

Su and Perlmutter (1985) also successfully applied the Random Pore Model to fit isothermal char oxidation data for different chars obtained from anthracite and bituminous coals. They observed a reasonable agreement between the calculated values of Ψ (using measured values of S_o, L_o and ϵ_o) and the value of Ψ needed to fit the experimental data. A typical value of Ψ, from their study, was 10. This gives a maximum reaction rate of 1.5 times the initial rate at X=0, and happens at a value of burnoff of about 0.35. They also compared reaction rate and pore surface area versus conversion at different reaction

temperatures and observed a good agreement between the two normalized curves, which implies that surface area changes are responsible for reactivity changes. This also justifies the use of the Random Pore Model.

Gavalas (1980) compared the results from the model with isothermal data from Mahajan et al. (1978) and Dutta and Wen (1977), and found a very good agreement up to 70% burnoff. At high values of burnoff (> 80%) the model seems to generally overpredict the oxidation rate. This can be due to the possible disintegration of the particle at high conversions or a change in activation energy. In the first case, the model is inapplicable. For the second case, a distribution of activation energies may need to be used for the modeling. Gavalas fitted the data using values of Ψ higher than those found by other authors, i.e., 30 and 150.

In the current study, the predictions of the Random Pore Model were also compared with isothermal data for lignite char from Tseng and Edgar (1984) and good agreement was observed. Interestingly, Tseng's data shows a small, progressive variation in the shape of the characteristic curve with temperature, mainly for low burnoff values. In that region, the reaction rate is found to be higher at low temperature. The authors explained this as follows: at low temperature, the reactant gas has enough time to diffuse into the ultramicropores, the size of which are near that of the gas molecule. At higher temperature, the ultramicropores cannot be reached by the reactant gas. The same phenomenon has also been reported by Radovic et al. (1983), who claim that the portion of the burnoff plot of increasing slope could be eliminated in most cases by decreasing the reaction temperature. They also attribute the effect to diffusional limitations and opening of previously partially closed pores. This demonstrates the difficulty in obtaining pure kinetic data, even at very low temperature. Gutierrez et al. (1987) also point out the fact that diffusion limitations can exist even if the experimental characteristic curves fall on the same curve. Tseng and Edgar (1985), in a study of bituminous and anthracite coals, examined the influence of diffusion limitations on the characteristic curve. They showed that kinetically limited characteristic curves have a maximum rate at a conversion of roughly 40%, while diffusion limited curves, depending on the degree of diffusion limitations, peak at lower conversions, i.e. between

0 and 30%. They also showed that, with an increasing diffusion resistance, the curves tended to the pore diffusion controlled characteristic curve, when the reaction is limited to the outside surface of the shrinking particle.

Data was analyzed from Ballal and Zygourakis (1987) for lignite, Pittsburgh #8 and Illinois #6 chars. This data represents an example of a mixed kinetic-diffusion limited system, where the peak of the characteristic curve changes with temperature (moving to higher conversion for lower reaction temperature), and typically occurs between 5 and 30%. The Random Pore Model was, however, used by the authors to fit the experimental data with a reasonable agreement. This shows that the model, derived for the kinetically controlled regime, can be used, to a certain extent, in situations where some diffusion resistance is present. Zygourakis also observed the variations in the shape of the characteristic curve with different reacting gases (O_2, CO_2).

Another important aspect of the analysis of combustion data concerns the measurement of oxygen chemisorbed on the surface. Floess et al. (1988) and Radovic et al., (1988) showed that, in the case of reaction in oxygen, substantial amounts of oxygen complexes can be present on the surface of the char. The rate of weight loss given by TGA is then the result of carbon loss through combustion and oxygen gain by chemisorption. Those authors showed that, for the chars they studied, by taking the oxygen weight gain into account the rate of weight loss was steadily decreasing with conversion, without an intermediate maximum. Lizzio et al. (1988) made measurements of carbon loss (through CO and CO_2 gases) using infrared detectors which showed the same features and matched reasonably well the oxygen corrected curve. Consequently, one has to be careful in attributing the change in rate as measured with TGA to effective changes in available surface area, as TGA results may not always give an accurate representation of those variations.

From these observations, we can conclude that experimental conditions (temperature, pressure and flow rate of oxygen, sample size) are important in order to define the type of reaction regime, i.e., kinetic or diffusion limited, and have a direct influence on the shape of the reaction rate vs. conversion, i.e., on the value of Ψ. Moreover, TGA analysis needs to be employed with caution, since it does not always reflect the "true" carbon loss but is the result of simultaneous carbon loss and oxygen gain.

Implementation of the Models at AFR - Our approach has been to use the Random Pore Model and volumetric model together with, if necessary, the implementation of either a continuous distributed rate or discrete multiple Arrhenius rates. This choice is based on the fact that active sites may have different activation energies, and that char becomes less reactive at high degrees of burnoff. Such a concept has been introduced following several TPD studies (Temperature Programmed Desorption) by Calo and Perkins (1987) and Du et al. (1990). These studies showed that there is a distribution of activation energies for oxygen complex desorption. It is reasonable to assume a possible distribution in activation energies of the sites which are active during combustion. However, it is believed that not all the sites containing an oxygen complex are active sites which will participate in the reaction. This makes TPD results difficult to implement directly for combustion conditions.

In the case of the need of such a distribution in activation energy (i.e. changes in reactivity which could not be attributed to surface area change), the parameters for the distribution will be determined by fitting both isothermal and non-isothermal data. However, up to this point we are using a single Arrhenius rate.

The coding, using a single Arrhenius rate, has been completed and tested over data and calculations provided (for the Random Pore Model) by Miura and Silveston (1989). The option for a distributed rate has been included in the coding, although, for a first approximation, a single activation energy will be used.

Experimental Work - A TG-FTIR apparatus was used. which combines a TGA (Thermogravimetric Analyzer) with an on-line FT-IR spectrometer. The simultaneous measurements of the weight loss from TGA and the amount of gas evolved from FT-IR gives the mass loss (TGA), carbon loss (FT-IR), and, by difference, the amount of oxygen complex on the surface. This approach allows a calculation of the "true" reaction rate.

Isothermal and non-isothermal data are currently being obtained. From the isothermal experiments, information can be obtained on the surface area changes and, possibly, on the activation energy distribution. One way to retrieve this information is to plot dW/dt versus W (W=amount of material left) for each data

point. This value corresponds to the instantaneous reaction rate k, assuming a first order reaction. Changes in k during an isothermal experiment indicate either a change in activation energy or a variation in available surface area.

Conditions: Control of the experimental conditions is important in order to make sure that no temperature gradients or diffusion limitations are present in the experiment. Small coal samples ($\leq$10 mg), an adequate oxygen flow (maximum 40 cc/min oxygen flow with a 250 cc/min helium flow, equivalent to 13% oxygen), and low temperatures are used. The low temperature and low pressure of oxygen insures a slow reaction rate (itself inversely proportional to the time constant $\tau_{0.5}$ = time of 50% burnoff), and a slow reaction limits the potential heat up of the sample (Tseng and Edgar, 1984). It also limits the diffusion resistance, since oxygen has enough time to reach even the smallest pores. Using small samples insures that no film diffusion resistance across the sample pan is present. However, problems resulted in both TGA reliability and homogeneity of the sample with the use of very small samples (<10 mg). As a compromise, 10 mg coal samples are being used. It is assumed that, although some external diffusion may be present because of the thickness of the bed, this does not have any influence on the results other than reducing the reactivity by a constant factor (Fig. II.A-10). Additional verification of this assumption will be performed.

Results (isothermal): Data were obtained over a wide range of temperatures, and with various types of chars. The rate of evolution of carbon from CO and CO_2 measurements using FT-IR was compared to the rate of mass loss using TGA. In general, both showed a similar shape of rate vs. conversion, which means that in the case of the chars studied, the effect of the weight of oxygen chemisorbed on the surface (usually less than 4% on coal basis) is not important when discussing changes in the curve's shape. Consequently, TGA measurements as well as FT-IR measurements can be used for the determination of kinetic rates of char oxidation. The amounts of evolved gases measured with FT-IR and of weight loss measured with TGA compare reasonably well, i.e., within 5% on coal basis. The difference mainly comes from SO_x, NO_x and other gases which are not accounted for by the FT-IR measurements.

In order to assess the experimental conditions under which kinetic control is obtained, a series of experiments were done with a 900°C Pittsburgh #8 char.

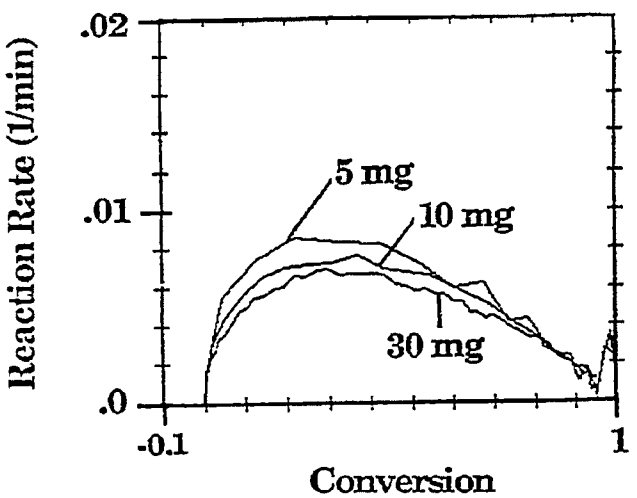

Figure II.A-10. Influence of the Sample Size on the Reaction Rate Measured with TGA at 480°C.

Initially, a reaction temperature of 560°C was used, which is 35°C lower than the value of T_{crit} from standard non-isothermal measurements. Under those conditions, the characteristic curve exhibits a maximum early in conversion (roughly 20%) followed by an almost linear decrease of the rate, which may be a sign of diffusion limitations. After reducing the reaction temperature down to 500°C, a characteristic curve with a maximum at 30% conversion was obtained . At 480°C, the maximum moved up to 35% conversion. At this temperature, the reaction rate is very low (0.01 min^{-1}), and the data are scattered, which necessitates an averaging over several data points. Since the maximum rate occurs at a conversion close to the 40% found by Tseng and Edgar (1985), it is likely that the reaction is kinetically controlled at that temperature.

For further proof, experiments were run with different coal particle sizes (100X200 mesh and -325 mesh) at the two temperatures of 480 °C and 560 °C. At 480 °C, as shown in Fig. II.A-11, the rate versus conversion curves overlay for the two particle sizes, while at 560 °C, as shown in Fig. II.A-12, the smaller particle size showed a higher rate and a slightly later peak in conversion than for the larger particle size. This confirms our suspicion that, at 480 °C, the reaction is kinetically limited and that, at 560 °C, diffusion limitations are present. These conclusions assume that the char particle size is correlated with the starting coal particle sizes which will require verification by optical inspection of the char particles. Further experiments will also be performed with a very large particle coal size cut (20X48 mesh) at these temperatures. Also, data at lower temperatures (440°C and 460°C) will be obtained in order to estimate the activation energy in the kinetic regime.

Data obtained with a 600°C Pittsburgh #8 char showed a different behavior, with a maximum at 35% conversion for the three temperatures used (500°C, 440°C and 420°C) and a characteristic curve identical in the three cases. However, in order to assess without any doubt the type of regime, additional runs will be performed with different particle sizes and in a larger temperature range. The fact that the characteristic curve does not vary may imply a basic difference between the 600°C char pore structure and the pore structure in higher temperature chars. Su and Perlmutter (1985) studied the pore structure of different types of chars and effectively found that more macropores, mesopores

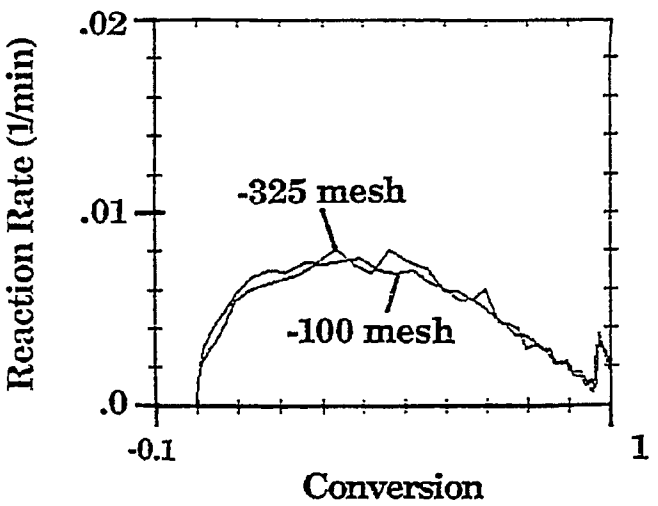

Figure II.A-11. Influence of the Particle Size on the Reaction Rate Measured with TGA at 430°C.

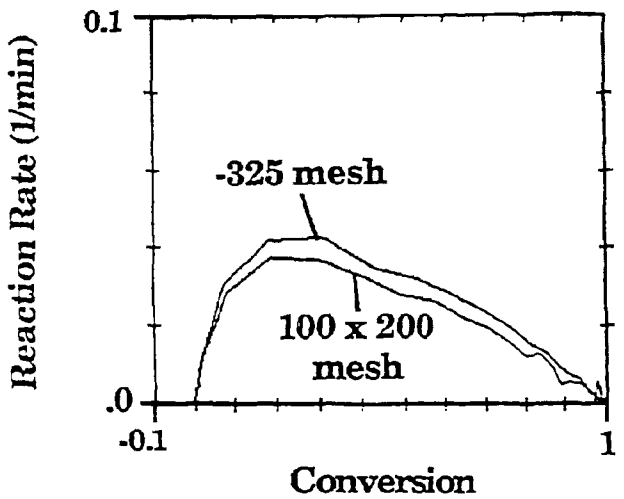

Figure II.A-12. Influence of the Particle Size on the Reaction Rate Measured with TGA at 560°C.

and micropores are present in low temperature chars. As a result, diffusion limitations may not be as important than for low porosity chars, even at higher temperature.

Isothermal reactivity data of 900°C chars of Zap, Illinois #6 and pocahontas were also obtained at reaction temperatures of 25°C lower than T_{crit}. For Illinois #6 and Pocahontas, the characteristic curves looked very similar to that of Pittsburgh #8, with a maximum at 15-20% conversion (i.e. some diffusion limitations are present). Oxidation of the Zap lignite resulted in a curve with no maximum at all, which is either representative of the pure diffusion limited regime (reaction limited to the external surface), or the result of a highly porous structure, with no diffusion limitations. Another possibility, which is thought to be the most probable, is that the catalytic influence of minerals is the major factor affecting reactivity of the lignite. Literature studies (Du et al., 1990) show that, in this case, reactivity is proportional to the amount of dispersed minerals, with no effect from surface area.

Results (Non-isothermal): From non-isothermal experiments, the T_{crit} of samples with different degrees of burnoff will be measured, which will also provide information on the available surface area and possibly the activation energy distribution. Chars with different degrees of burnoff (0% to 100%) will be produced isothermally. The temperature of the char burnoff experiments will be at least 100°C lower than the critical temperature measured by non-isothermal experiments in order to be under chemical reaction control and to have a reasonable time scale.

Modeling of AFR data (kinetic control) - The Random Pore Model is used to fit kinetically limited systems, i.e. isothermal or non-isothermal experiments at low temperatures, and *for coals for which surface area changes are the main cause of reactivity variations, i.e., medium and high rank coals.*

Surface Area: Data of a Kentucky coal were obtained over a large range of burnoff (0% to 95%). Measurements of surface area (N_2 and CO_2) in m^2/g based on the initial amount of char showed an initial increase up to about 25% burnoff followed by a continuous decrease. The fit of surface area using the Random Pore Model as shown in Fig. II.A-13 led to a good agreement between data and theory for $\Psi = 10$. Data of calculated surface area based on changes in T_{crit}

measurements with burnoff (normalized to appear on the same scale than measured values) are also shown in Fig. II.A-13. A good correlation is found between the relative variations of the calculated values and those of the experimental data. This result supports the use of T_{crit} data to evaluate relative variations in reactivity and estimate the functions f, g and h.

Low-temperature char: As mentioned above, the characteristic curve of the reactivity as a function of burnoff for low-temperature Pittsburgh #8 char was found to be similar over a large range of temperature. As presented in Fig. II.A-14, the curve was very well fitted at all temperatures with a value of Ψ of 50 and an activation energy of 30 kcal. This agrees with the value of activation energy found by Tseng and Edgar (1985) in a similar study using bituminous coals.

High-temperature char: This type of char has been found to be very sensitive to diffusion limitations. This is probably due to a lower macro and micro porosity than for chars produced at less severe conditions. Consequently, only oxidation data obtained at very low temperatures will be used for these chars to make sure that the reaction is kinetically limited.

Reactivity predictions: Although T_{crit} is probably measured in the diffusion limited regime, it was shown above that it still accurately represents relative variations in reactivity. Using the large database of measured T_{crit} values for different coals and chars, the functions f, g, h of the model will be determined.

Predictions of Reactivity Level

In order to predict the reactivity level, the measurement and evaluation of the number of active sites on char surfaces have been the object of extensive work. However, the current methods (TPD, TGA, FTIR, ...) do not allow a direct measurement of the number of active sites. In the absence of any accurate method of determination of active site concentration, AFR's approach has been to develop correlations of reactivity with known parameters of coal and chars.

In order to establish trends in reactivity, numerous measurements of T_{crit} values were performed for various coals and chars. Although the measurement of T_{crit} is thought to occur at the limit of the diffusion limited regime, it is

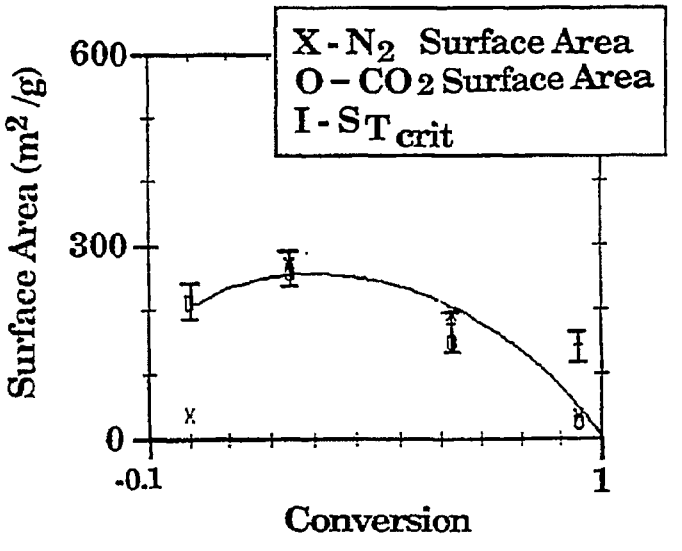

Figure II.A-13. Comparison of CO_2 Surface Area (X), N_2 Surface Area (O) and the Calculated Surface Area from T_{crit} Measurements (I) with Model Predictions of Surface Area (—) as a Function of Conversion.

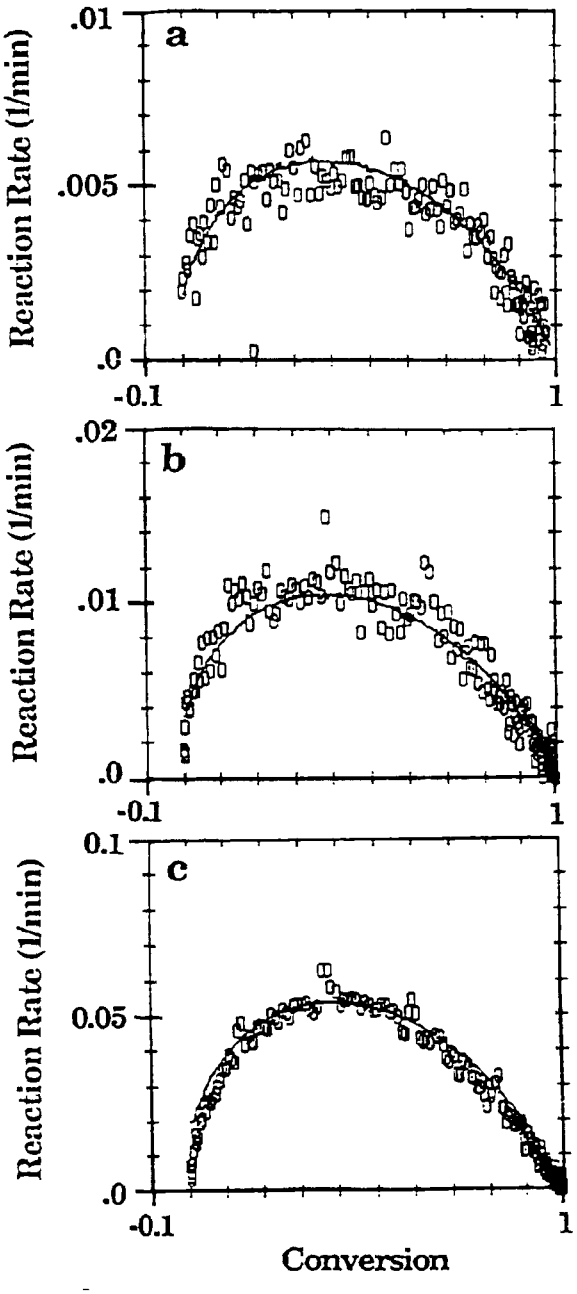

Figure II.A-14. Comparison of TGA Data (O) and Model Prediction (—) for the Reaction Rate of 600°C Pittsburgh No. 8 Char as a Function of Conversion. a) 420°C, b) 440°C, and c) 500°C.

believed that it still provides a valuable estimate of differences in active site concentrations. Correlations of T_{crit} as a function of mineral content, oxygen content and hydrogen content of the char have been observed. Those correlations reflect the fact that the amount of active sites is dependent on the following:

- The degree of pyrolysis of the char (or arrangement or graphitization), which can be characterized by the hydrogen content of the char.

- The coal rank, which can be characterized by the oxygen content.

- The amount of catalytic impurities present in the coal, which overcome the influence of the intrinsic reactivity, and can be characterized by the mineral content (Ca in particular).

Correlations can be used to evaluate differences in active site concentrations, which can be in turn included in a model to predict reactivity as a function of temperature and burnoff.

The reactivity model developed at AFR is based on a Random Pore Model for high rank coals (reactivity dependent on internal surface area) and a volumetric model for low rank coals (catalytic reaction). Although the model has been developed for the kinetic regime, it is believed that ratios between relative reaction rates remain the same under regime I (kinetic regime) or regime II (diffusion limitations),i.e. it is assumed that all coals are affected in a similar manner by diffusion limitations. This should allow the use of the model to compare different values of T_{crit}. Uncertainties about the magnitude of the reaction rate under zone II conditions will be lumped into a multiplying factor.

Using a single activation energy, the reaction rate given by the model can be written as expressed in Eq. II.A-1 for medium and high rank coals and as expressed in Eq. II.A-3 for low rank coals.

In order to account for the large differences in reactivity between different coals and different chars from the same coal, we introduced in the

preexponential factor, A, a dependence on the oxygen and mineral content of the coal as well as on the degree of pyrolysis of the char estimated using the amount of hydrogen contained in the char. A can be written as follows:

$$A = A_{HRC}\, f(H_{char})\, g\,(O_{coal}) \qquad \text{(II.A-4)}$$

for high rank coals

$$A = A_{LRC}\, f(H_{char})\, g\,(O_{coal})\, h\,(Ca_d) \qquad \text{(II.A-5)}$$

for low rank coals

with H_{char} = hydrogen content of the char
O_{coal} = oxygen content of the coal
Ca_d = dispersed calcium content of the coal
f,g,h = functions to be determined using correlations

The reaction rate is then given by:

$$\frac{dX}{dt} = A_{HRC}\, f\,(H_{char})\, g\,(O_{coal})\ \exp\frac{-E}{RT}\,(1-X)\,S_o\,\frac{1}{1-\epsilon_o}\,\sqrt{1-\psi\ Ln(1-X)} \qquad \text{(II.A-6)}$$

for high rank coals

$$\frac{dX}{dt} = A_{LRC}\, f(H_{char})\, g(O_{coal})\, h(Ca_d)\, \exp\frac{-E}{RT}\,(1-X)\,S_o\,\frac{1}{1-\epsilon_o} \qquad \text{(II.A-7)}$$

for low rank coals

$F(H_{char})$, $g(O_{coal})$, $h(Ca_d)$ are functions which can be estimated using correlations.

Development of Correlations - F, g and h are expected to be positive functions of the char hydrogen content, coal oxygen content and coal calcium content, respectively. Since T_{crit} is inversely proportional to the reactivity (the higher T_{crit}, the less reactive the coal), $1/T_{crit}$ is a more appropriate quantity to use to find correlations.

H_{char} correlation: Good linear correlations of $1/T_{crit}$ vs H_{char} were obtained for all coals, as shown in Fig. II.A-15. The curves all showed very similar slopes, which implies that the influence of the degree of pyrolysis of the char is the same for all coals. The data also seems to show a plateau for values higher than 3.5% H_{char}, which was included in the modeling.

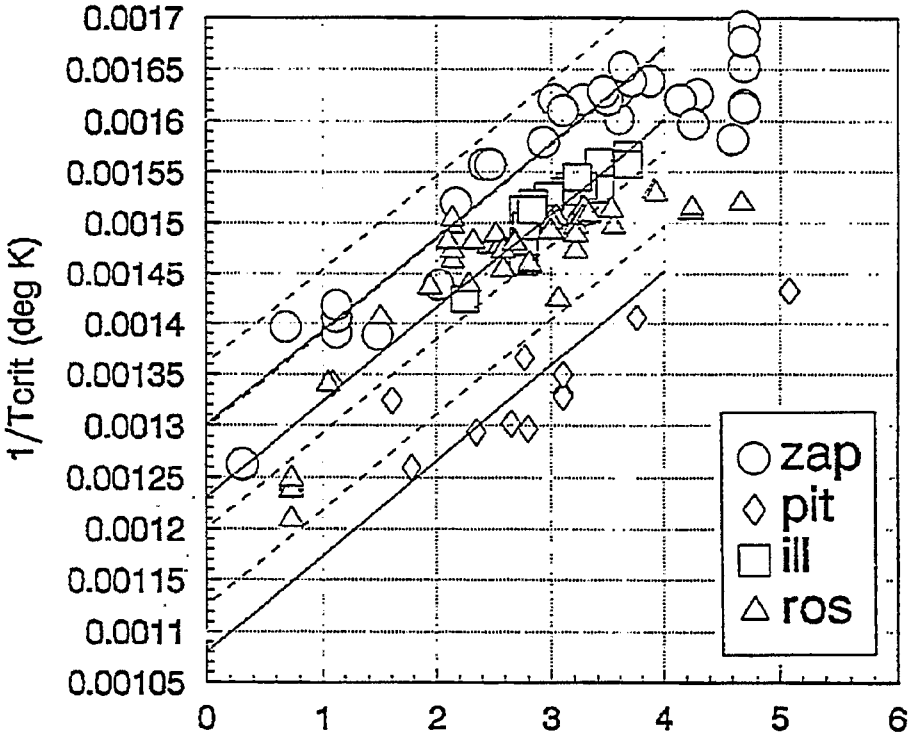

Figure II.A-15. Correlation of $1/T_{crit}$ with the Hydrogen Content of Char (H_{char}). The Solid Dashed Lines Correspond to the Model with No Adjustable Parameters. The Solid Lines to One Adjustable Parameter.

O_{coal} correlation: For identical values of H_{char}, the value of $1/T_{crit}$ for different coals gives an idea of the influence of coal rank on reactivity, and should be roughly correlated with oxygen and/or mineral content. Plots of $1/T_{crit}$ (using 900°C chars) as a function of the coal oxygen content also showed a reasonable correlation (Figure II.A-16) and could be used concurrently with the more extensive database of T_{crit} from chars from different coals.

The observations described above imply that one can clearly separate the influence of the degree of pyrolysis from that of the coal rank (as measured by oxygen content) and from the mineral catalytic effect. These will appear in the model as distinct parameters used to calculate the active site concentration.

Mineral correlation: Since mineral concentration is important only for low rank coals, a correlation was obtained using coals of oxygen content higher than 13%. As for the other correlations, a linear fit gave a good representation of the data (Figure II.A-17). For low rank coals the influence of minerals needs to be clearly separated from the effect of coal rank as measured by oxygen content. Since demineralized low rank coals show a reactivity similar to the one of medium rank coals (of oxygen content approximately 13%), the mineral content is a more reliable parameter than coal rank to define reactivity. In order to account for that in the model, the value of O_{coal} will be kept constant and equal to 13% for coals of oxygen content higher than 13%.

The correlations of $1/T_{crit}$ with H_{char}, O_{coal} and M gave the equations:

$$1/T_{crit} = a \cdot H_{char} + b \cdot O_{coal} + d \quad \textit{for high rank coals} \qquad \text{(II.A-8)}$$

$$1/T_{crit} = a \cdot H_{char} + b \cdot O_{coal} + c \cdot Ca_o + d' \quad \textit{for low rank coals} \qquad \text{(II.A-9)}$$

with $a=9.3 \times 10^{-5}$, $b=1.58 \times 10^{-5}$, $c=1.03 \times 10^{-4}$, $d=1.00 \times 10^{-3}$ and $d'=1.26 \times 10^{-3}$.

As discussed above, for low rank coals the parameter O_{coal} was kept constant at a value of 13%.

Following the procedure below, one can then derive the form of the correlation functions f, g and h. It is implicitly assumed that 1-X is relatively

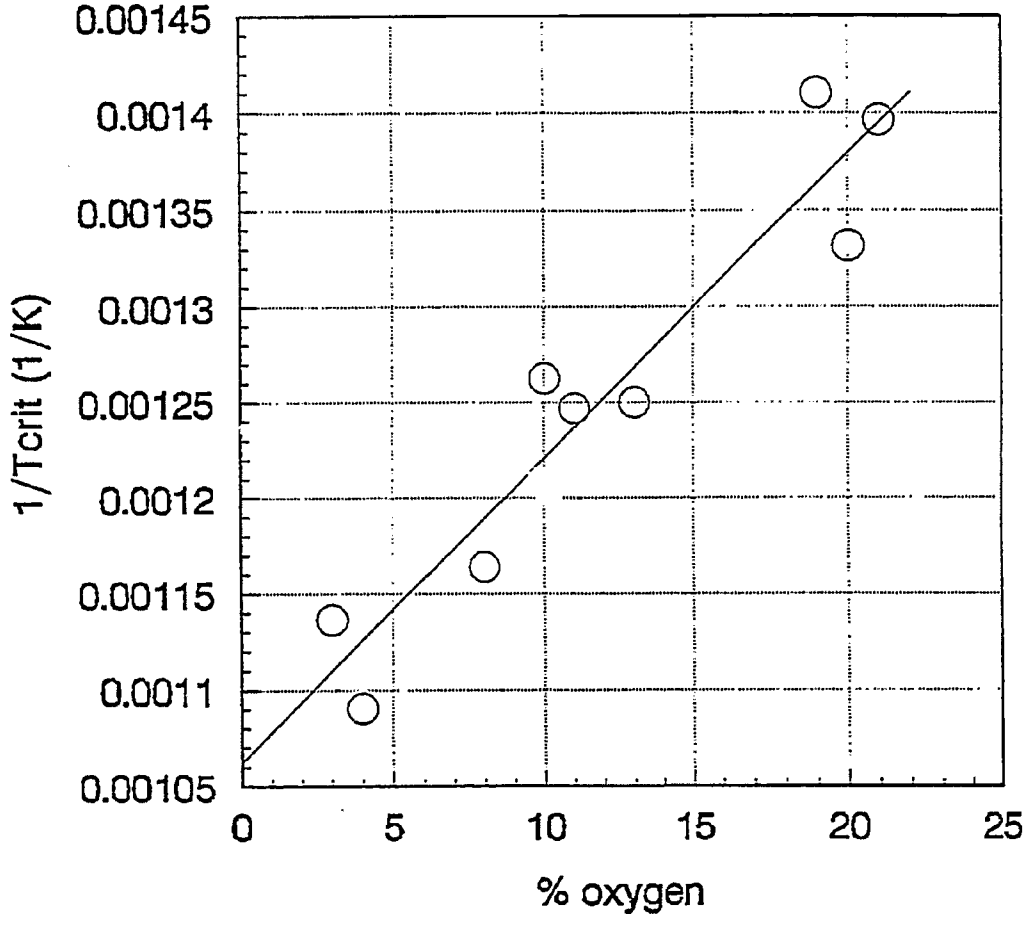

Figure II.A-16. Correlation of of $1/T_{crit}$ with the Coal Oxygen Content (O_{coal}).

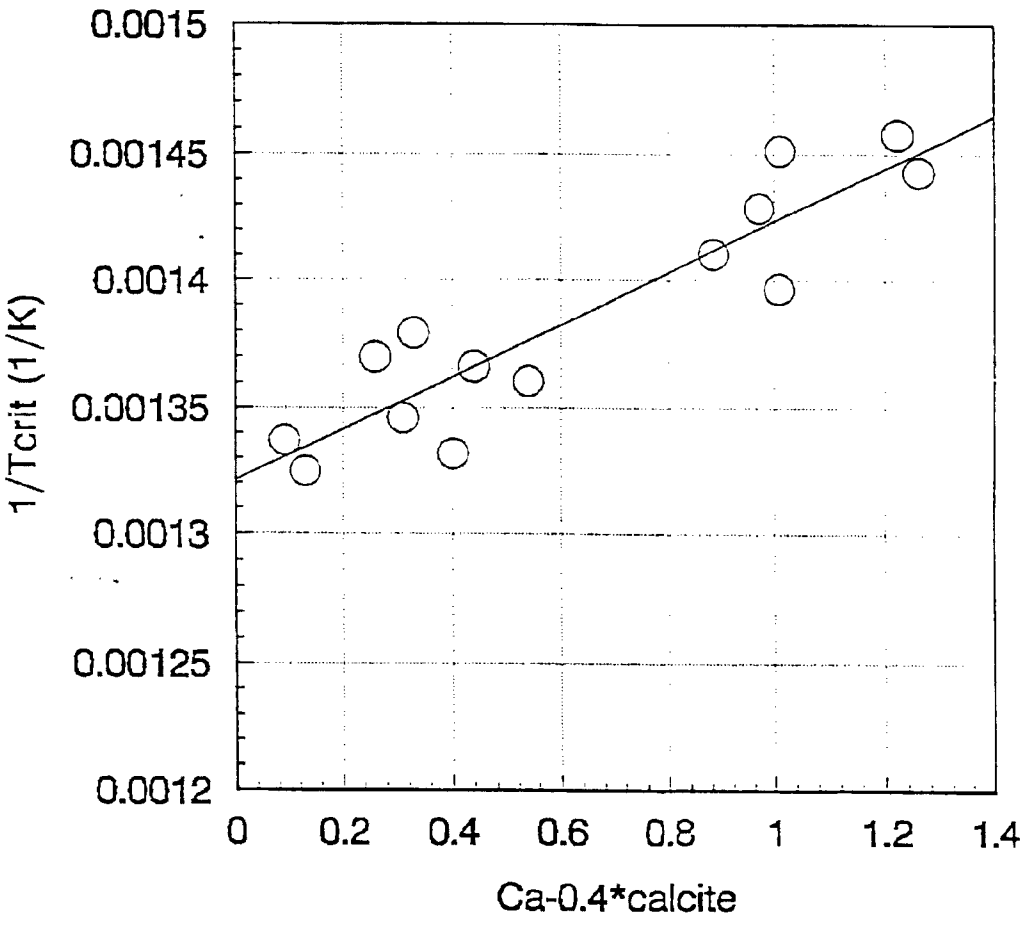

Figure II.A-17. Correlation of of $1/T_{crit}$ with the Amount of Dispersed Calcium (%).

constant (in the range 0.8-0.9), as well as S. At T_{crit}, the rate of weight loss reaches the value of 0.065/min, which can be written:

$$0.065 = A_{HRC} f(H_{char}) g(O_{coal}) \exp \frac{-E}{RT_{crit}} (1-X) S_o \frac{1}{1-\epsilon_o} \sqrt{1-\psi \ln(1-X)} \qquad \text{(II.A-10)}$$

for high rank coals, and

$$0.065 = A_{LRC} f(H_{char}) g(O_{coal}) h(Ca_d) \exp \frac{-E}{RT_{crit}} (1-X)\ S_o \frac{1}{1-\epsilon_o} \qquad \text{(II.A-11)}$$

for low rank coals.

Case of High Rank Coals: (O_{coal} < 13%)

Replacing $1/T_{crit}$ in Eq. II.A-10 by Eq. II.A-8 leads to the following expression:

$$0.065 = A_{HRC}\, f(H_{char})\, g(O_{coal}) \exp \frac{-E}{R} (aH_{char} + bO_{coal} + d)\, (1-X)\, S_o \frac{1}{1-\epsilon_o} \sqrt{1-\psi \ln(1-X)} \qquad \text{(II.A-12)}$$

Assuming an activation energy of 30 kcal, the functions $f(H_{char})$ and $g(O_{coal})$ can be taken as follows:

$$f(H_{char}) = \exp(E/R\ a \cdot H_{char}) = \exp(1.4 \cdot H_{char}) \qquad \text{(II.A-13)}$$

$$g(O_{coal}) = \exp(E/R\ b \cdot O_{coal}) = \exp(0.237 \cdot O_{coal}) \qquad \text{(II.A-14)}$$

Using a factor of 1.3 to take into account the fact that T_{crit} is measured at the limit of the diffusion regime, and assuming 1-X=0.85, Ψ = 0, ϵ_o = 0.3 and S_o=3.9 x 10^8 m^2/m^3 (corresponding to 300 m^2/g), the preexponential factor A_{HRC} can be taken as:

$$A_{HRC} = 0.065 \exp\left(\frac{E}{R} d\right) \frac{1}{1-X} \frac{1}{S_o} (1-\epsilon_o) \frac{1}{\sqrt{1-\psi \ln(1-X)}} \cdot \frac{1}{60} \cdot 1.3 = 9.75 \times 10^6 \qquad \text{(II.A-15)}$$

which transforms equation (II.A-6) into:

$$\frac{dX}{dt} = 9.75 \times 10^6 \exp \frac{-15000}{T} \exp(1.4\ H_{char}) \exp(0.237\ O_{coal})\ S_o (1-X) \frac{1}{1-\epsilon_o} \sqrt{1-\psi \ln(1-X)}\ \ 1/\rho \qquad \text{(II.A-16)}$$

Case of Low Rank Coals: (O_{coal} > 13%)

For low rank coals we have:

$$0.065 = A_{LRC} f(H_{char}) g(O_{coal}) h(Ca_o) \exp \frac{-E}{R} (a\, H_{char} - b\, O_{coal} + cM + d')\,(1-X)\, S_o \qquad \text{(II.A-17)}$$

The function h(M) can be taken as:

$$h(M) = \exp(E/R\, c\, M) = \exp\ (1.54 \cdot M) \qquad \text{(II.A-18)}$$

and the preexponential factor is given by:

$$A_{LRC} = 0.065 \exp\left(\frac{E}{R}\, d'\right) \frac{1}{1-X} \frac{1}{S_o} (1-\epsilon_o) \cdot \frac{1}{60} \times 1.3 = 4.8 \times 10^{-4} \qquad \text{(II.A-19)}$$

which leads to the final expression:

$$\frac{dX}{dt} = 4.8 \times 10^{-4} \exp \frac{-15000}{T} \exp\,(1.4\, H_{char}) \exp\,(1.54\, M)\, S_o\,(1-X)\ \ 1/p \qquad \text{(II.A-20)}$$

More data points with coals of oxygen content between 13% and 16% will be needed in order to accurately interface the two models. The values of the rates as expressed in (II.A-16) and (II.A-20) are valid for an oxygen pressure of 0.13 atm.

Correlation results - Separate correlations plots gave a precision range of about: ±20 °C. Parity plots of the results from the simultaneous correlations using H_{char}, O_{ccal}, and M are shown in Figure II.A-18. The range of precision can be estimated as ± 40 °C. Using the correlation based on the hydrogen content and adjusting arbitrarily one of the others (one adjustable parameter) led to a much better prediction of the data, with a range of precision of ±20 °C as shown in Figure II.A-19. It should also be noted that the range of precision of determination of T_{crit} is ± 10 °C.

Deviations from correlations - Several assumptions have been made in order to determine the correlating functions: the char surface area is supposed to be relatively constant, as well as the burnoff value at which T_{crit} is measured. The parameters A and E are also assumed to be constant over the range of coals and chars studied. Any small variations of those factors can lead to variations in reactivity which would be measured as variations in T_{crit}.

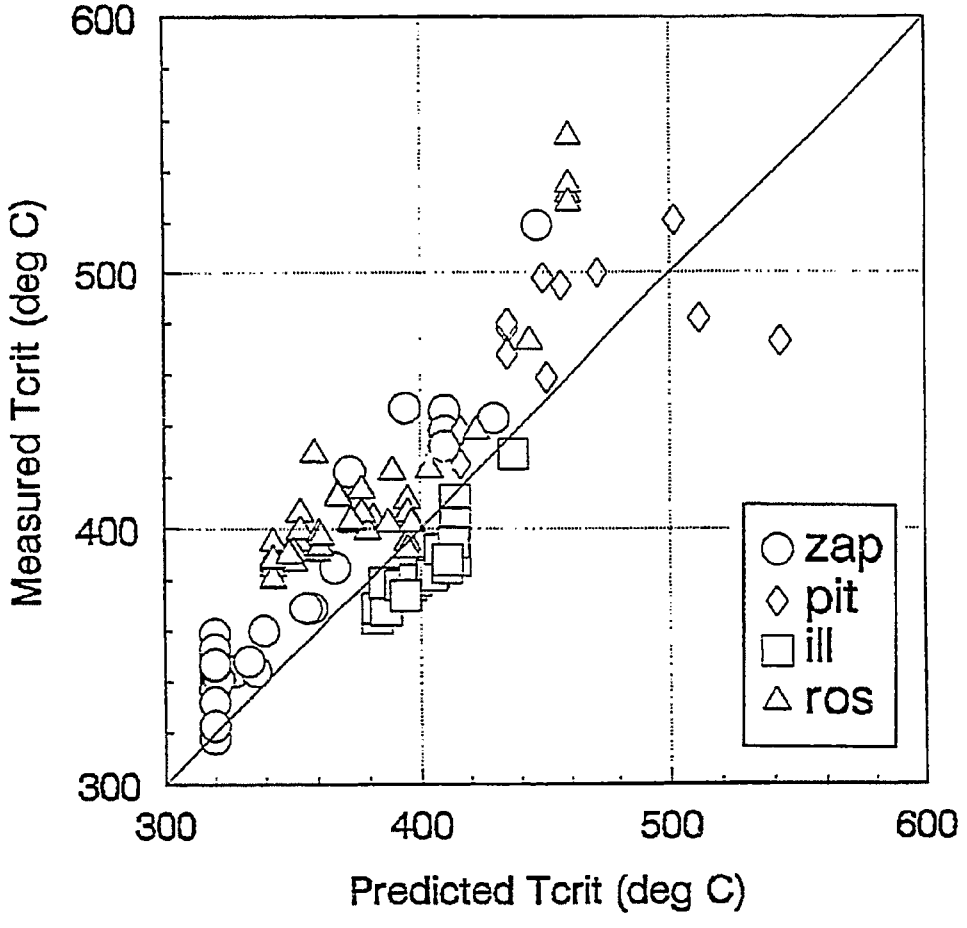

Figure II.A-18. Measured T_{crit} vs. Predicted T_{crit} using Three Correlations Simultaneously and No Adjusting Parameters.

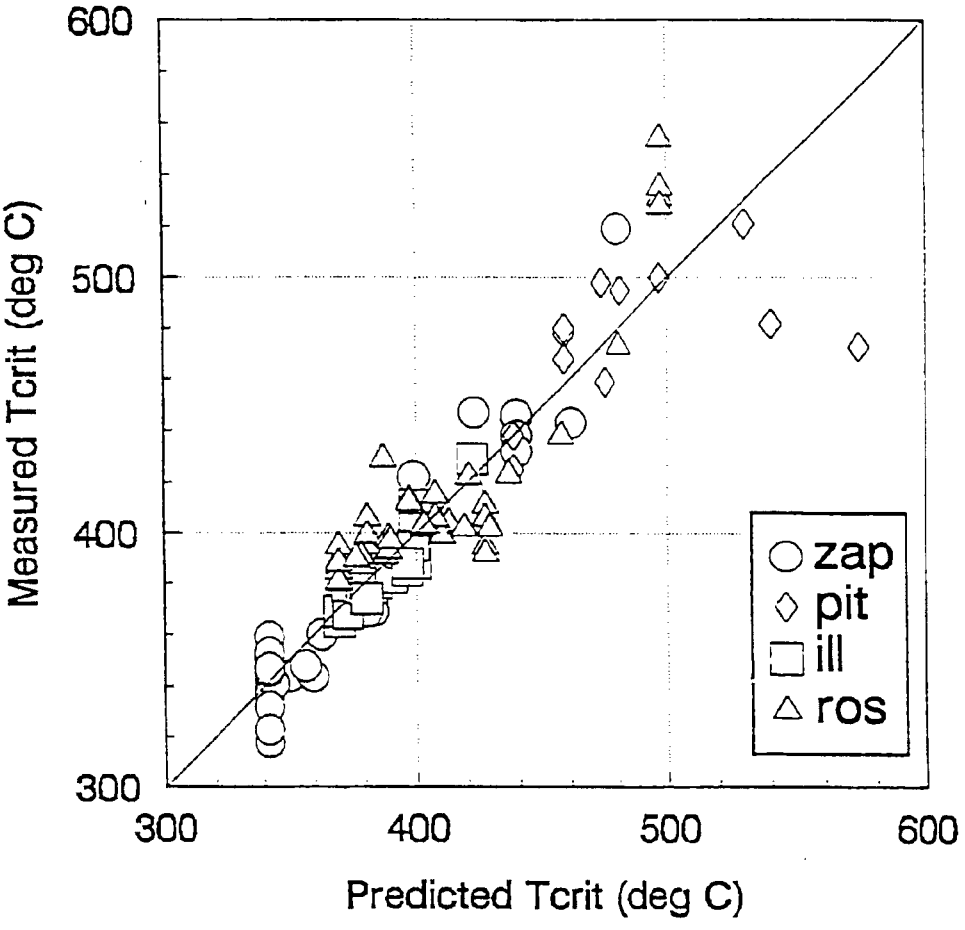

Figure II.A-19. Measured T_{crit} vs. Predicted T_{crit} using Three Correlations Simultaneously and One Adjusting Parameters.

The choice of the correlating parameters used in this study (i.e. H_{char}, O_{coal}, M) may also present some limitations in giving an accurate representation of the active site concentration. For example, in the case of the mineral correlation for low rank coals, reactivity has been found to correlate with the amount of dispersed calcium. Unfortunately, this value cannot be easily measured. Calcium can be found under several forms, which are not all catalytically active: well dispersed calcium substituted on carboxylic groups effectively acts as a catalyst, while calcium in the carbonate form ($CaCO_3$), usually present in large chunks, seems to have no influence on reactivity. In this study, the total amount of calcium was measured with SEM while the carbonate amount was obtained using FT-IR. The difference between the two values gives an estimate of the well-dispersed calcium and is the value which was used in the correlation. A difficulty arises in that FT-IR cannot differentiate between several kinds of carbonates ($CaCO_3$, Na_2CO_3, K_2CO_3). Although calcium carbonate is probably the most important fraction, the others types may also be present in significant amounts. This means that the amount of calcium acting as catalyst, calculated as mentioned above, may not be very accurate. Moreover, the degree of dispersion of substituted calcium could vary significantly with the coal, and would induce variations in reactivity. A more elaborate model should include the effects of both the amount and degree of dispersion of calcium.

The correlation with initial coal oxygen content also is approximate since the oxygen content is not always an accurate measure of coal rank. This would be especially true of coals which had similar oxygen contents, but significantly different hydrogen or heteroatom (nitrogen and sulfur) contents.

It should also be noted that the oxygen and mineral correlations are based on T_{crit} measurements over chars produced primarily at one condition (900 °C), which may not give a fully consistent picture with others chars. Moreover, since several correlations are used and not all data points fall on the derived curves, errors can add and lead to predictions which are far off the measured values. This points out the difficulty in using results for separate correlations without an adjustable parameter.

To overcome those uncertainties, it is probably reasonable to assume that one parameter (A for example) can be adjustable in a range to be specified later.

Predictions in the kinetic regime - T_{crit} measurements, even though performed for some coals in a partly diffusion limited regime, are believed to give an accurate representation of relative changes in active site concentration. In order to verify this assumption, we will need to apply the predictions derived from T_{crit} correlations to the kinetic regime. The determination of the preexponential factor A will be necessary since it is going to be slightly different than the one calculated from T_{crit} data. If the correlations derived using T_{crit} are valid in any regime, changes in reactivity in the kinetic regime between different chars should be predicted.

Plans

Complete work on the fluidity model and optical properties model. Continue work on the models for swelling, char reactivity and the evolution of sulfur and nitrogen species. Deliver PCGC-2 submodels for swelling and char reactivity.

II.B. SUBTASK 2.B. - FUNDAMENTAL HIGH-PRESSURE REACTIONRATE DATA

Senior Investigators - Geoffrey J. Germane and Angus U. Blackham
Brigham Young University
Provo, Utah 84602
(801) 378-2355 and 6536

Student Research Assistants - Chuck R. Monson, Gary Pehrson, and Ken Bateman

Objectives

The overall objectives of this subtask are to measure and correlate fundamental reaction rate coefficients for pulverized-coal char particles as a function of char burnout in oxygen at high temperature. The effect of high pressure will be investigated.

The specific objectives for the past year include:

1. Review appropriate literature in pertinent areas.
2. Complete and characterize the HPCP reactor and support systems for char preparation and oxidation studies.
3. Continue the preparation and characterization of chars from the coals selected for this study, using the HPCP for char production.
4. Review and continue to develop the final char oxidation test plan.
5. Conduct oxidation tests in the HPCP reactor with chars produced from several of the coals selected for study.

Accomplishments

Three components of the subtask have been identified to accomplish the objectives outlined above: 1) design and construct a laminar-flow, high-pressure, controlled-profile (HPCP) reactor, 2) prepare char at high temperature

and high pressure, and 3) determine the kinetics of char-oxygen reactions at high pressure.

The original proposed program schedule called for completion of the high-pressure, char oxidation studies by October, 1990. The completion date was extended with no increase in budget since the funds originally allocated for this subtask were not depleted at the end of the fourth year. The HPCP reactor, capable of functioning at 400 psi (27 atmospheres), has been constructed and successfully instrumented to perform the fundamental reaction rate measurements required for the study. For the determination of kinetic parameters, data will be included from a char oxidation study conducted with an atmospheric pressure reactor constructed under independent funding.

HPCP Reactor and Instrumentation Development

Reactor Development – A number of final modifications were performed on the HPCP reactor during the reporting period. Computer software was written to support the data acquisition and heater control hardware that was previously interfaced to the reactor instrumentation and heaters. The program allows the microcomputer to record and provide readout of reactor temperature, pressure and gas flow rates. These data, along with other information pertaining to a given test, are written periodically to an electronic file during the test. The program also provides control of the reactor heaters. The four heat zones are controlled concurrently. In addition to maintaining the desired reactor temperature, the control algorithm checks for inaccurate thermocouple measurements, ensures that the heaters stay below their maximum allowable temperature, and controls the rate of temperature change to prevent thermal shock breakage of ceramics in the reactor. The control system reduces temperature deviation during a test and improves repeatability of reactor conditions for duplicate tests.

Modifications were made to the preheater to improve its capacity. The preheater heating element is now surrounded by a 12.7-cm-ID alumina tube. The secondary gas flows through a packed bed of alumina that fills the void between the alumina tube and the preheater insulation. The large increase in available heat transfer area in the bed significantly improves the preheater capacity.

Under separate funding, the gas mixing station was assembled and interfaced with the data acquisition system. The station consists of the hardware necessary to meter and mix two gas flows. Nitrogen and air are mixed during char oxidation experiments to provide oxygen concentrations from 0 to 21% for the primary and secondary gas flows.

Optical Instrumentation – Work continued during the reporting period on the pyrometer. The optical instrument has been successfully operated using both Spherocarb and coal char.

The accuracy of the char kinetic parameters derived from the HPCP reactor experiments will depend to a large degree on the reliable measurement of particle temperature, velocity and size. Researchers at Sandia National Laboratories have developed an optical pyrometry technique to measure these parameters and have applied it to char oxidation experiments in a transparent-wall, flat-flame burner (Tichenor et al., 1984). This pyrometry technique has been modified and implemented on the HPCP reactor.

Pyrometer Description - The pyrometry technique differs from conventional two-color pyrometry in that it uses an image-plane, coded aperture to obtain simultaneous, in-situ measurements of the temperature, size and velocity of individual reacting particles. Incandescent particles moving along the centerline of the reactor are imaged at actual size onto a coded aperture by a pair of lenses. This coded aperture is composed of a number of windows and blackouts that pass or block the light emitted from the particle. The light transmitted through the aperture is split into two wavelength bands which are detected by a pair of photomultiplier tubes (PMT's) and recorded by a high-speed, digitizing oscilloscope. The result is a pair of traces or a signature of the particle that contains information describing the particle temperature, size and velocity.

Figure II.B-1 is a schematic of the pyrometer. In addition to the particle-imaging system discussed above, the complete instrument consists of trigger and calibration systems. A laser beam, normal to the centerline of the optics and immediately upstream of the sample volume, acts as the trigger. A

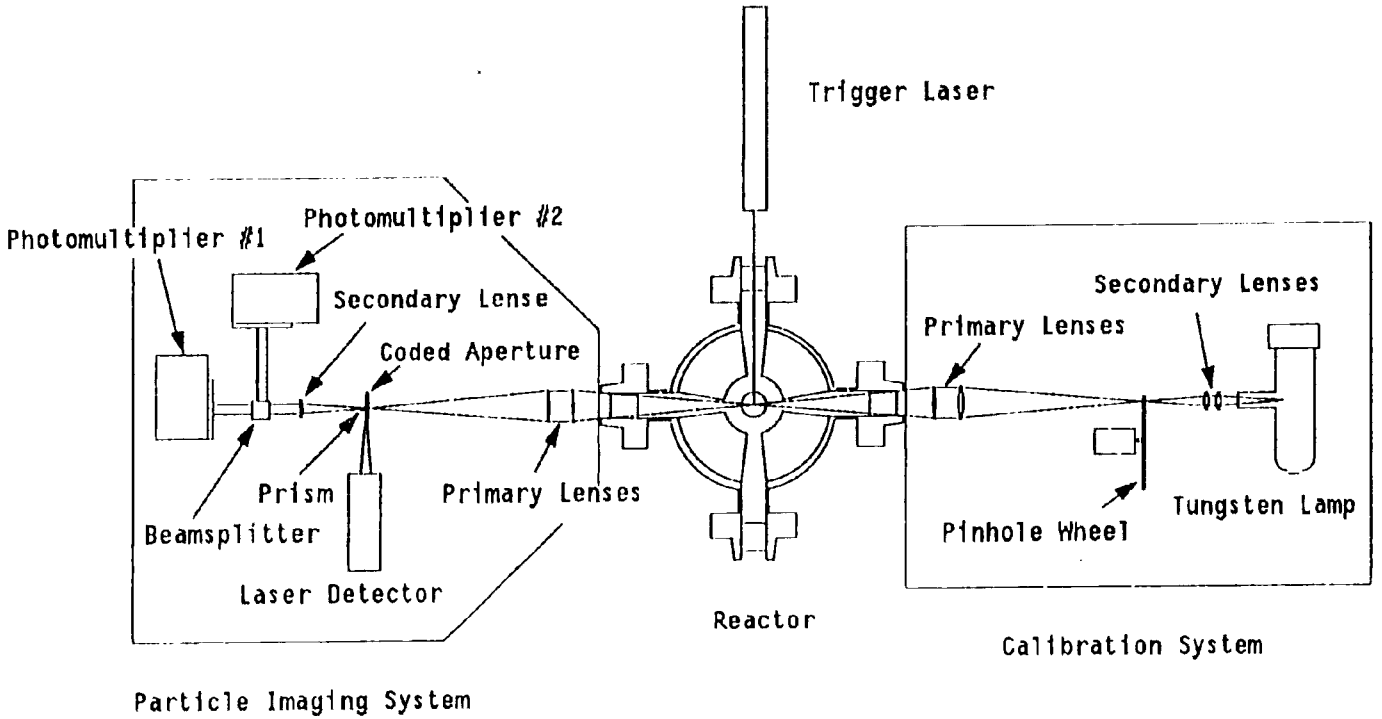

Figure II.B-1. Pyrometer for making in-situ measurements of particle temperature, size, and velocity in the HPCP reactor.

particle moving down the centerline of the reactor passes through the laser beam, scattering the laser light. A portion of this scattered light travels through the optics to the laser detector, generating a trigger pulse to begin sampling by the digital oscilloscope. The trigger system prevents errors in the measured particle size by ensuring that a sampled particle is in focus and centered on the coded aperture. The calibration system is built into the pyrometer to provide temperature, velocity and diameter standards for calibrating the instrument. During calibration, a false particle image is projected into the sample volume of the reactor. The image is formed by focusing a tungsten strip lamp of known temperature onto a series of pinholes that are mounted on a rotating disc. The pinholes chop the lamp light and lenses focus the false particle image into the sample volume.

Coded Aperture - The coded aperture, shown in Figure II.B-2, contains a series of carefully sized blackouts and windows. The narrow window is part of the trigger system, and the large window, in which a particle is fully visible, allows determination of the particle temperature and speed. The three consecutive occlusions facilitate particle size measurement. Traces generated from the aperture, representative of a 100-μm particle, are also displayed in Figure II.B-2. Although the traces appear somewhat irregular because of optical and electronic noise, several features are readily apparent. Five major peaks and four valleys are prominent. All five peaks are relatively flat, indicating that the projected particle was completely visible in each of the aperture's five windows. The four valleys, which correspond to blackouts between the windows, indicate that different amounts of the particle image were occluded by each blackout. The large blackout between the first windows completely occluded the 100-μm particle and thus caused the signal voltage to return to the baseline. The fraction of the particle that was occluded by the 70-, 25- and 10- μm blackouts decreased with blackout size, as evidenced by the decreasing depth of the corresponding valleys.

Particle Temperature, Size and Velocity - Particle temperature and velocity are determined from the traces in a manner similar to that used by researchers at Sandia. The wide plateau of each of the traces is used to determine the particle temperature by two-color pyrometry (500 and 700 nm). The

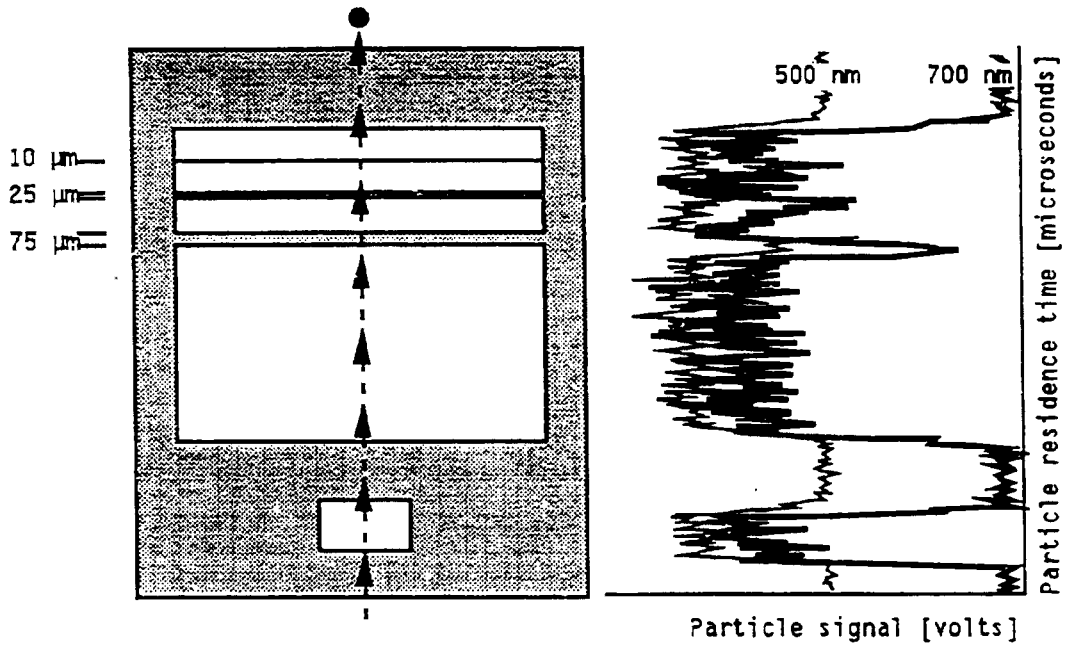

Figure II.B-2. The BYU Coded Aperture and a Representative Particle Trace.

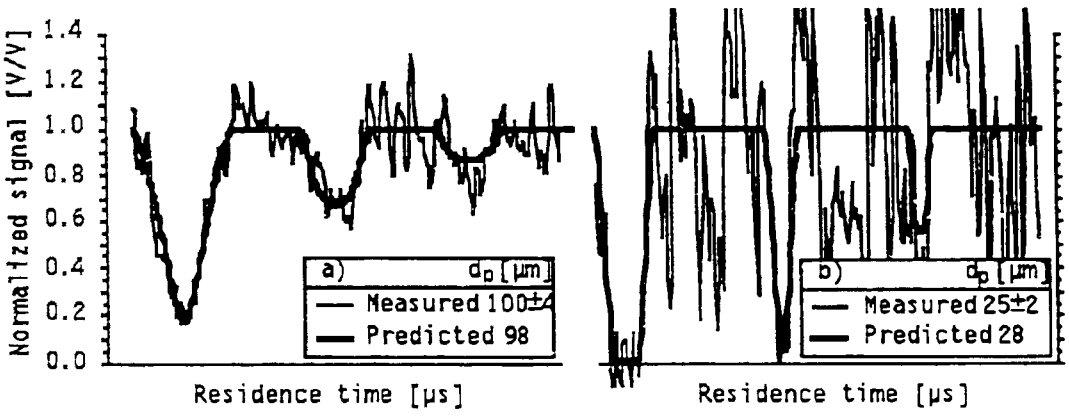

Figure II.B-3. Portions of Corresponding Measured and Predicted Particle Traces.

ratio of the two wavelength intensities is used in conjunction with Wien's law and the gray body assumption to calculate the particle temperature. The particle speed is determined from the time taken for the particle to traverse the aperture's largest window. Particle size is extracted from the signal by means of a unique fitting technique. An initial estimate of the particle diameter is obtained by lowpass digital filtering of the traces at about 25 kHz to remove excess noise. The general shape of the filtered traces is first examined to ensure that it represents a single particle traversing the coded aperture. The magnitudes of the occluded and unoccluded signals (peak height versus valley depths) in the filtered, 700 nm trace are then used to calculate the estimated diameter in a manner similar to the Sandia size measurements.

The estimated diameter is subsequently refined by a geometric/statistical fitting technique. In the technique, a geometric model uses the particle's velocity and estimated diameter to generate a predicted particle trace. The magnitude of the predicted trace is directly proportional to the fraction of the particle's projected area that is not occluded by the coded aperture. An optimization program (Parkinson et al., 1984) is used to determine the particle diameter that produces the best agreement between the predicted trace and the measured (unfiltered) 700 nm trace. Agreement is quantified by using the sum of the squared differences between the two traces. In this manner the entire particle signature is used to determine the particle size, and the random noise in the measured signal is removed by the fitting process. The entire trace analysis (determination of particle temperature, velocity, and size) requires approximately 3 seconds on the microcomputer.

Figure II.B-3 shows portions of the measured and predicted particle traces obtained from 100-μm and 25-μm particles. The 100-μm particle produced a much stronger signal than the 25-μm particle (6.07 V as opposed to 0.38 V), but the traces were normalized for purposes of comparison. Since the measured trace obtained for the 100-μm particle contains little noise, it may yield a successful particle size determination by merely comparing the occluded and unoccluded signals, as done by other researchers. In the trace generated from the 25-μm particle, however, the noise (magnitude and frequency) in the measured 25-μm trace is similar to the particle signal itself. Since lowpass filtering

cannot smooth the trace without affecting the valley depths, an accurate measure of the occluded and unoccluded signals cannot be obtained and particle size cannot be determined. The geometric/statistical sizing technique, however, fit this noisy trace and accurately determined the particle diameter. This technique extends the lower limit of the pyrometer, allowing the size determination of smaller/lower temperature particles of inherently lower light emission.

Adaptation of the Pyrometer to the HPCP Reactor - A number of problems were encountered in applying the particle sizing pyrometer to the HPCP reactor, the most significant resulting from emissions generated by the glowing reactor wall. Diametrically opposed view ports provide a clear view through the reactor, ensuring that the particle is viewed against a cold background. However, diffuse light from the glowing reactor tube can enter the instrument optical path resulting in an increase in measurement noise. If not minimized, this noise can completely overpower the relatively low signal from a char particle. A number of steps have been taken to reduce the amount of stray light entering the optical path. The access holes in the reaction tube have been enlarged (to 2 cm), alignment of the pyrometer has been optimized, and masking has been accomplished with iris apertures, one (water-cooled, 1 cm I.D.) inside the reactor view port near the reaction tube and another external to the reactor near the primary lenses. These steps have signifigantly reduced the background noise level from the glowing reactor tube.

Another concern in applying the pyrometer to the heated-wall furnace is the possibility of particle temperature measurement errors due to reactor wall reflections off of char particles. In order to quantify this effect, an analysis was performed using Wien's approximation of Planck's law in conjunction with the standard, two-color pyrometry approximation of gray body particles. The emissivity of a char particle was taken as 0.8, while that of the reactor wall was set at 0.4. A worst-case analysis was performed assuming that full reflectance occurred. The results are shown in Figure II.B-4. Measured particle temperature is plotted against reactor wall temperature for four actual particle temperatures. It is seen that at lower wall temperatures, the measured and specified values are essentially the same. As the wall temperature is increased above that of the particle, the measured particle temperature

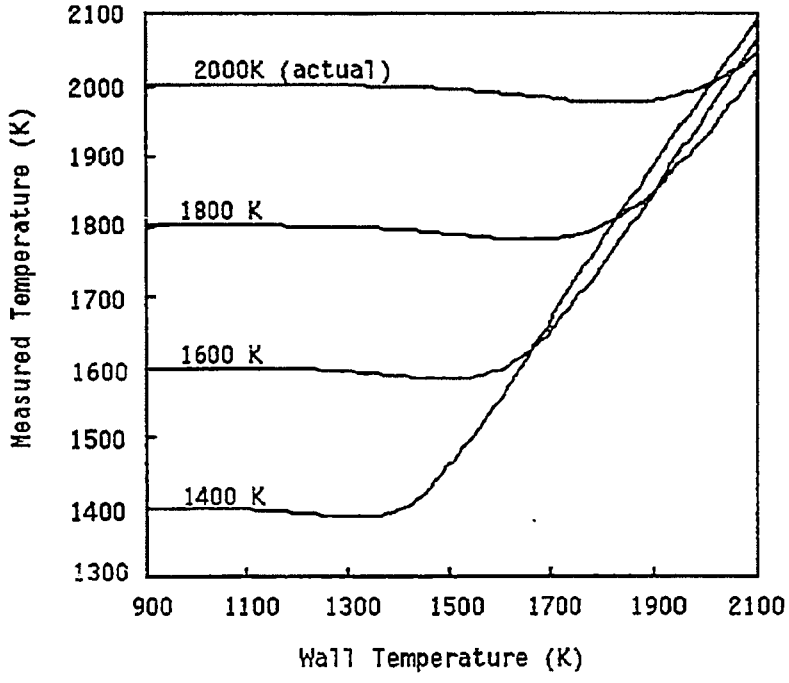

Figure II.B-4. Measured Temperature Error Calculated From Full Wall Reflectance.

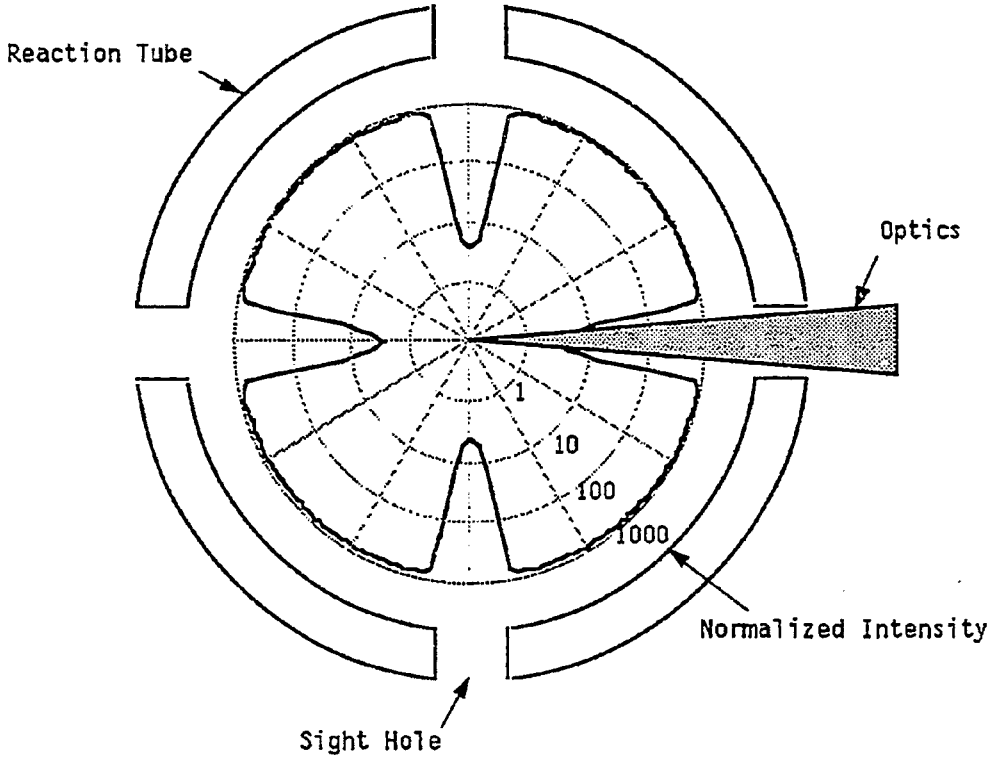

Figure II.B-5. Total Radiation Scatter Plot for a 25-μm Particle (at 700 nm) at the Sampling Plane of the HPCP Reactor.

gradually approaches the wall temperature and large errors are introduced. As long as the particle is hotter than the wall, the measured temperature is only slightly low, with the maximum error (about 25 K at a particle temperature of 2000 K) occurring when the wall is about 100 K cooler than the particle temperature.

The preceding analysis was performed assuming that full reflectance occurred. Further analysis was performed to determine how much reflectance would actually occur. The scattering behavior of a char particle was determined using a program (Bohnen and Huffman, 1983) to solve the Maxwell electromagnetic equations governing a particle's radiation field. It was assumed that the particle was spherical with a complex refractive index of $2.0 - i\ 1.0$ (Mengüc and Viskanta, 1987). The radiation scatter plots generated by the Maxwell analysis show that nearly all of the radiation leaves a char particle in the forward direction. Figure II.B-5 shows the radiation field for a 25-μm particle (at 700 nm) as it passes through the optical plane of the elevated-pressure reactor. It was obtained by integrating the radiation scatter plot around the reaction tube, allowing no radiation to be emitted from the tube sight holes. Very little radiation originating from the reactor wall is collected in the optical instrument lenses. In fact, the maximum temperature errors computed above, assuming full wall reflectance, are decreased by over two orders of magnitude. Hence, wall reflections from char particles have little effect on the pyrometry measurements.

Pyrometer Characterization - The calibration system of the pyrometer was used to investigate the performance characteristics of the instrument. Figure II.B-6 shows the output signal level of the 700-nm channel for a range of temperatures and particle sizes. As expected from Planck's law, the signal has an exponential relationship with the particle temperature and a squared dependence on the particle diameter. The signal increases by two orders of magnitude when a 100-μm particle is heated from 1450 to 2100 K. The lowest signal level shown, about 100 mV (where the noise amplitude is on the order of half the signal level), corresponds to the lowest temperature particle trace that could by analyzed automatically by the trace analysis routine. The

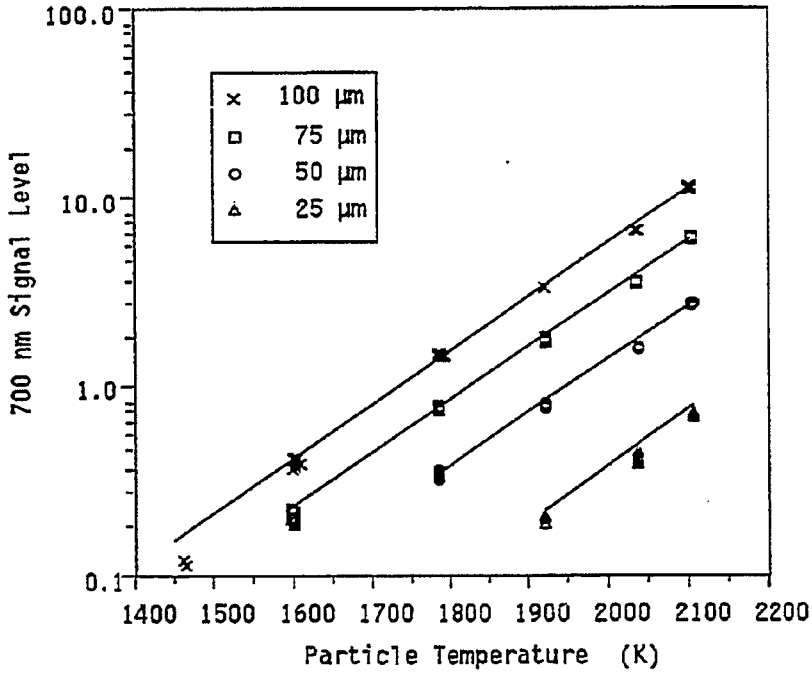

Figure II.B-6. Red Channel Output as Functions of Particle Temperature and Size.

analysis routine can be operated with user interaction to extend the limit to about 50 mV, resulting in a lower temperature limit that depends on particle size as follows:

100 µm	-	1200 K
75 µm	-	1300 K
50 µm	-	1400 K
25 µm	-	1600 K

Figure II.B-7 contains the results from a number of calibration runs, illustrating the precision and accuracy associated with each of the pyrometer measurements. Each point represents an average of ten analyzed particle traces (with the exception of the 100 µm, 1460 K point that was generated from two traces). The errors in the temperature and velocity are low and within an acceptable range. Because the particle is not imaged onto the coded aperture perfectly and because of aberrations in the optical elements, the particle diameter measurements have a positive offset. This offset is accounted for in measurements with a calibration equation.

Proper operation of the pyrometer was examined using oxidizing Spherocarb and North Dakota lignite. Figure II.B-8 shows a representative Spherocarb trace with its associated parameters, and Figure II.B-9 plots particle temperature vs. size for the lignite char. It was discovered that the trigger was not functioning properly during the lignite runs, resulting in the capture of out-of-focus particles. The measured particle sizes are, therefore, larger than the actual particle. The temperature and velocity measurements that do not rely on a finely focused particle image are accurate. Work is proceeding to more effectively distinguish the trigger signal.

Char Preparation at High Temperature and High Pressure

During the reporting period, emphasis continued to decrease the particle size range of the fractions of the selected coals and to produce sufficient coal in the desired size ranges for the char oxidation tests. Presently, Pitt. HVA, UT Blind Canyon HVB, Wyodak SUBC, and Beulah-Zap LIGA have been sized in sufficient quantities in the large particle range (64-75 µm) for the test program.

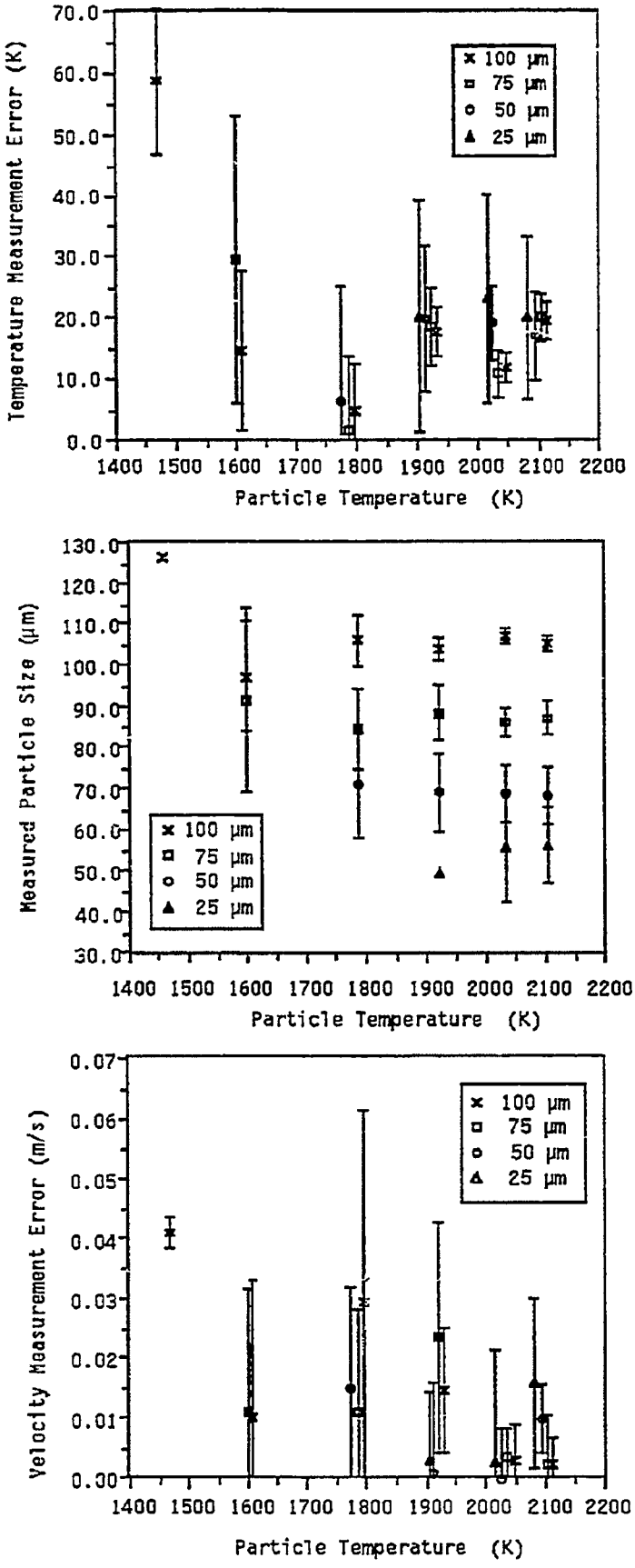

Figure II.B-7. Characterization of the Pyrometer by the Calibration System.

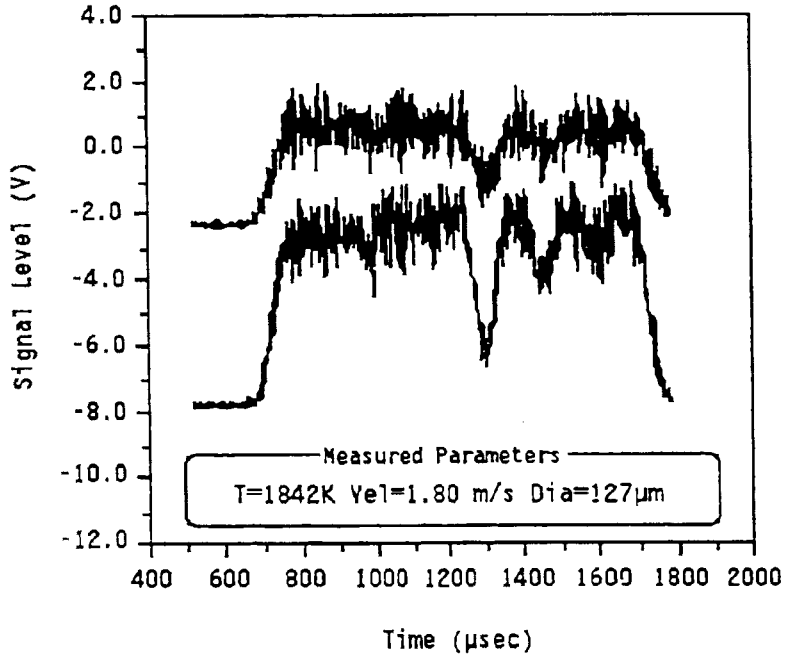

Figure II.B-8. Representative Traces from a Spherocarb Particle.

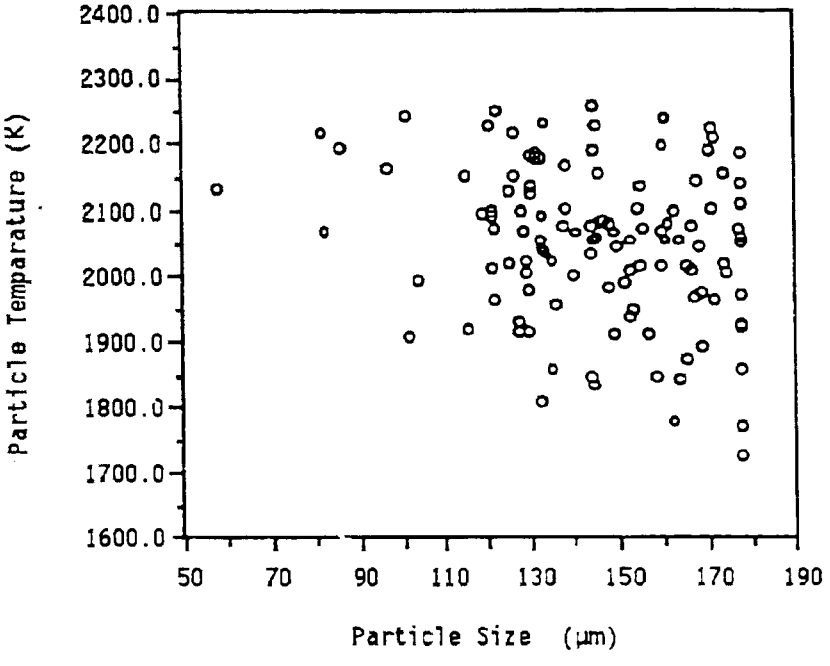

Figure II.B-9. N. Dakota Lignite Char Temperature and Size Measurements.

A sample of Utah bituminous coal was studied with a scanning electron microscope to classify the size distribution of the coal particles. The coal had been sieved to a range of 64-75 μm but there was some uncertainty as to whether any fine particles (<10 μm) had adhered to the larger coal particles of the desired range. Scanning electron micrographs (SEM) showed a range of particle size of about 60-80 μm with so few smaller particles that their possible effect on devolatilization and subsequent oxidation is considered to be insignificant.

Accuracy of Titanium Analyses – In a related project in which the extent of char burnout is measured using a calculation based on the titanium content of the char, the accuracy of the titanium measurements by ICP was questioned because of the observations that calcium and sodium measurements of chars appeared to increase with the sample size. However, this behavior is not observed for measurements of titanium, silicon and aluminum with the ICP. Faires, Apel and Niemczyk (1983) reported on a complex solution matrix effect for alkali and alkaline earth elements when analyzed with the inductively coupled plasma (ICP) technique. They concluded that the alkali elements only interfere significantly with other alkali elements in the observed emission signal. This interference is called an intra-alkali matrix effect and appears to enhance the analyte emission at positions low in the plasma and depress the emission high in the plasma. There is a "crossover" point in the plasma where enhancement changes to depression. At this vertical position in the plasma there appears to be no net effect on analyte emission intensity due to an alkali matrix. In our calculations of kinetic parameters no alkali or alkaline earth elements will be involved and there should be no significant matrix effects from alkali elements on the concentrations of Ti, Si and Al.

Kinetics of Char-Oxygen Reactions at High Pressure

Char oxidation experiments will be performed with five coals varying in rank from lignite to high-volatile bituminous: Pitt. HVA, UT Blind Canyon HVB, IL #6 HVC, Wyodak SUBC, and Beulah-Zap LIGA. These are all relatively common U.S. coals that have been used in char oxidation studies. All of the coals are included in the Penn State, the Department of Energy and the Argonne National Laboratory coal banks.

Char preperation – Samples of these coals are in the process of being ground and size-classified with a combination of sieving and aerodynamic techniques to produce tight size fractions of 64-75 μm and 37-44 μm. The size fractions are being verified by scanning electron microscope and Coulter counter measurements.

Chars for the oxidation experiments will be prepared in the HPCP furnace in a nitrogen environment. Since devolatilization conditions greatly affect char characteristics, all of the chars will be prepared at the same reactor conditions. These conditions will also be more extreme than those expected for the oxidation experiments to ensure that no further devolatilization occurs during the char oxidation tests. Char preparation conditions will be as follows: atmospheric pressure, wall and gas temperatures of 1700 K, an initial particle heating rate of 10^4k/s (calculated using gas and wall temperature measurements), and a particle residence time of 300 ms.

Char Oxidation Tests – In order to obtain accurate results, a number of conditions must be met during the char oxidation experiments. The first of these is concerned with the particle temperature history. In the analysis of the results, it is assumed that the particle temperature is constant as it passes through the reaction zone. In order to approach this in the experiments, the gas temperature must be carefully controlled. The preheated secondary flow should enter the reaction zone somewhat hotter than the desired gas temperature to provide a rapid heatup of the primary gases and particles. The temperature of the gas and particles must also rapidly drop at the end of the reaction zone, upon entry into the collection probe. For each of the experimental conditions, the preheater temperature and the wall heater zone settings that provide the most isothermal gas temperature profile (measured with the gas suction pyrometer) will be found. The quench gas flow rate required to significantly drop the temperature at the collection probe entrance will also be determined (a 20% decrease in gas temperature corresponds to about a 90% decrease in reaction rate for the temperature range in the experimental plan). The particle temperature history is also required to be the same for all of the particles. Since the gas motion is developing from a plug to a laminar flow, the gas and particle velocities at the reaction tube axis will be greater than at some off-

axis location. Particle dispersion must be held to a minimum if all particles are to experience the same residence time. This will be monitored by visual observation at the reactor optical accesses. Another requirement for reliable measurements is a constant oxygen concentration in the bulk gas. In order to ensure that this concentration is not affected by particle reactions, the char feed rate should be at least 100 times smaller than the stoichiometric gas flow rate (Annamalai and Ramalingham, 1987). This is easily accomplished and is also a requirement for proper functioning of the optical instrument.

Other conditions necessary for meaningful results include bounds on the ratio (c) of the measured burning rate to the diffusion limited rate, and the char burnout. Mitchell (1989) found that the chemical reactivity of a char remains constant during burnoff until the final stages when the percentage of ash in a particle becomes large. Thus, the upper bound on char burnout will be set at 90% to prevent errors due to the ash component. The lowest acceptable burnout will be 10%, since large uncertainties are associated with the analyses and reaction rate calculations when only minimal reaction has occurred. Only those experiments producing char burnouts between 10 and 90% will be included in the reaction rate determinations. The acceptable range for c will be 0.1 to 0.85. When reaction rates are slower than this, low burnouts are produced and large uncertainties result. For oxidation conditions where c is larger than 0.85, the reaction is nearly completely controlled by bulk diffusion and chemical reaction rates cannot be determined.

Table II.B-1 shows the experimental plan for the Utah Blind Canyon coal char oxidation tests. Gas temperatures will be varied from 1000 to 1500 K and total gas pressure will range from 1 to 25 atm. Oxygen concentration will be varied from 4 to 21% in nitrogen (corresponding to oxygen partial pressures between 0.1 and 1.0) to allow determination of the reaction order. The effect of total pressure with constant O_2 concentration will be examined by comparing tests 1-3, 10-12, and 16-17 as well as with tests 7-9, 13-15, and 19-21. The

effects of total pressure and oxygen partial pressure will be distinguished by comparing tests 4-6 with tests 7-9 , tests 10-12 with tests 13-15 and tests 16-18 with tests 19-21. In these runs, total pressure will be increased while holding oxygen partial pressure and other test variables constant. In a few

Test	Gas Temp (°K)	Press (atm)	O_2 Conc (%)	O_2 Press (atm)	Res Time (ms)	Diameter (μm)
1	1000	1	10	0.1	100	70
2	1200	1	10	0.1	100	70
3	1500	1	10	0.1	100	70
4	1000	1	20	0.2	100	70
5	1200	1	20	0.2	100	70
6	1500	1	20	0.2	100	70
7	1000	5	4	0.2	100	70
8	1200	5	4	0.2	100	70
9	1500	5	4	0.2	100	70
10	1000	5	10	0.5	100	70
11	1200	5	10	0.5	100	70
12	1500	5	10	0.5	100	70
13	1000	10	5	0.5	100	70
14	1200	10	5	0.5	100	70
15	1500	10	5	0.5	100	70
16	1000	10	10	1.0	100	70
17	1200	10	10	1.0	100	70
18	1500	10	10	1.0	100	70
19	1000	25	4	1.0	100	70
20	1200	25	4	1.0	100	70
21	1500	25	4	1.0	100	70
22	1200	1	20	0.2	50	70
23	1200	1	20	0.2	150	70
24	1200	10	5	0.5	50	70
25	1200	10	5	0.5	150	70
26	1000	1	20	0.2	100	40
27	1500	1	20	0.2	100	40
28	1000	10	5	0.5	100	40
29	1500	10	5	0.5	100	40

Table II.B-1. Experimental Plan for UT Blind Canyon Coal.

tests, particle residence time will be varied in order to quantify pore surface area changes with burnoff. These will be carried out at atmospheric and 10 atm pressure to determine the effect of total pressure on the particle surface area. Tests will also be conducted with the smaller size fraction to help determine the controlling regime. A few tests will be conducted with raw coal to determine the effect of pressure on combined devolatilization and oxidation.

This full test set will be performed with char produced from the Utah Blind Canyon coal. This will quantify the effects of pressure on not only the mass reactivity and reaction rates of the char but also on the char's physical characteristics. Subsequent to the analysis of the residue from these initial tests, a reduced test set will be carried out for the remaining coals. Use of this smaller test set will allow the determination of the general effects of pressure for a range of coals without performing an impractical number of tests. The reduced test sets will cover the same pressure range as the full test set, but contain fewer intermediate points. Also, the effect of burnout will not be examined and the temperature ranges will be adjusted to correspond to the reactivity of the chars; temperature ranges for the Beulah-Zap and Illinois #6 chars will most likely be lowered to prevent complete burnout of the samples.

Char Analysis - The following analyses and calculations will be performed for each char:

Analyses: *In-situ* particle temperature, size and velocity; elemental - ICP, CHN; size - SEM, Coulter Counter; density - bulk, apparent and true; N_2 surface area.

Calculations: Burnout; mass reactivity; global reaction rate parameters - reaction order, frequency factor, activation energy.

The burnout (dry, ash free) of a sample will be determined using titanium as a tracer (Pace, 1982) by

$$B = \frac{x_{T_i}\left(1 - x_{a_f}\right)}{x_{T_f}\left(1 - x_{a_i}\right)} \qquad \text{(II.B-1)}$$

x_{a_i} = mass fraction of ash in the original char

x_{a_f} = mass fraction of ash in the oxidized char

x_{T_i} = mass fraction of titanium in the original char

x_{T_f} = mass fraction of titanium in the oxidized char

The titanium content of a sample will be determined from elemental analysis, using an inductively coupled plasma (ICP). Ash content will also be determined as part of the ICP analysis.

The mass reactivity of a given sample will be calculated from the following expression:

$$\rho_m = \frac{B}{t_r} \qquad \left[\frac{g}{g\text{-}s}\right] \qquad \text{(II.B-2)}$$

t_r = particle residence time

The global reaction rate coefficient will be calculated by

$$k_c = \frac{\rho_m}{P_g^n (1-x)^n} \qquad \left[\frac{g}{cm^2\text{-}s}\right]\left[\frac{1}{atm}\right]^n \qquad \text{(II.B-3)}$$

P_g = oxygen partial pressure in the bulk gas

n = reaction order

x = ratio of the actual burning rate to the maximum rate possible

The reaction rate coefficient, k_c, follows the Arrhenius form:

$$K_c = A \exp\left(-E/RT_p\right) \qquad \left[\frac{g}{cm^2\text{-}s}\right]\left[\frac{1}{atm}\right]^n \qquad \text{(II.B-4)}$$

A = frequency factor
E = activation energy
T_p = particle temperature
R = gas constant

The activation energy and frequency factor at a given total pressure will be determined by relating calculated values of k_c with the corresponding measured particle temperatures. The range of oxygen partial pressures in the experimental plan will make possible the calculation of reaction order. The approach taken in these calculations will follow that of Young and Smith (1981), since it results in the best statistical fit of the data to the Arrhenius expression. At a given total pressure, values of k_c will be calculated for a number of values of n, in the range 0 to 1. At each value of n the relation between k_c and T_p will be determined in the Arrhenius form using a least-squares analysis. This will result in a sum of the squared residuals (Sr^2) for each value of assumed n. The best fit for the Arrhenius relation, with corresponding E, A and n, will be taken as that exhibiting the minimum Sr^2.

The effect of total pressure on the mass reactivity, global reaction rate parameters and controlling regime will be examined for all of the coal chars. In addition, the effect of total pressure on the pore structure of the Utah Blind Canyon char will also be examined.

Plans

Work will continue to carefully prepare the remaining IL #6 HVC coal samples prior to char preparation and oxidation. With the successful development of the optical particle imaging and thermometry system, the char preparation and oxidation tests will begin according to the plan outlined above.

II.C. SUBTASK 2.c. - SECONDARY REACTION OF PYROLYSIS PRODUCTS AND CHAR BURNOUT

SUBMODEL DEVELOPMENT AND EVALUATION

Senior Investigator - James R. Markham and Michael A. Serio
Advanced Fuel Research, Inc.
87 Church Street, East Hartford, CT 06108
(203) 528-9806

Objective

The objective of this subtask is to develop and evaluate by comparison with laboratory experiments, an integrated and compatible submodel to describe the secondary reactions of volatile pyrolysis products and char burnout during coal conversion processes. Experiments on tar cracking, soot formation, tar/gas reactions, char burnout, and ignition will continue during Phase II to allow validation of submodels.

Accomplishments

Discussions were held with BYU on the future direction of the work on modeling the tomography data from the TWR coal flame experiments. Some discrepancies exist in the measured and predicted particle temperatures which could result from problems with the measurements and/or the model. A rate limiting step in comparing the model with the data is the generation of suitable plots. A new approach which involves output of the predictions of the model into a spreadsheet format was agreed upon.

Under this subtask, models for ignition and soot formation will be delivered. An outline of the proposed particle ignition submodel is shown in Fig. II.C-1. The essential ingredients of the ignition model are already in PCGC-2. What is needed is to refine the assumptions regarding the fraction of CO_2 formed at the surface, as opposed to the gas phase, and the amount of energy feedback to the particle from the oxidation reaction of CO. These are related questions.

Input	Ignition Model	Output
Particle Temperature (PCGC-2) Char Reactivity Volatile Evolution (FG-DVC) Emissivity Oxygen Concentration (PCGC-2)	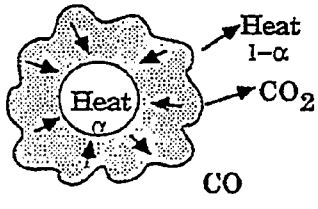	Particle Temperature Particle Reactivity Rate

Figure II.C-1. Outline of Particle Ignition Submodel

An outline of the proposed soot submodel is shown in Fig. II.C-2. The soot formation model, to date, is a calculation of the equilibrium amount of condensed carbon. This does a good job of predicting the location of the soot maximum but not the magnitude or the burnout. What is needed is a kinetic model for soot formation and destruction.

During the past year, work was done on developing a radiative model for soot as part of the soot submodel and the results were sent to BYU. The inputs will be the volume fraction of soot and the temperature. The output will be the average soot emissivity. The main difficulty will be to correct for the presence of CO_2 and H_2O. This work is being done jointly with BYU since the radiation model is an integral part of PCGC-2. A literature correlation is being used (Kent and Honnery) to make predictions of the average soot emissivity. Correlations from Hottel and Sarofim (1967) are being used to correct for the contributions of water and CO_2. Based on comparisons to an actual measured soot, water and CO_2 spectrum, it appears that these corrections are accurate to within 5%.

A primary concern was to correct for the effect of the water and CO_2 bands. It turns out that these bands are sufficiently close to the location of the average wavelength of the soot radiation that the soot acts like a grey body.

The work on the soot radiative properties submodel was completed and these changes have already been implemented into PCGC-2. This includes a correction factor due to the overlap of the soot continuum with spectral lines for H_2O and CO_2.

Soot Radiative Properties

In previous work, equations II.C-1a and 1b were developed to describe the soot radiative properties as a function of temperature. However, these equations did not have a correction factor due to the overlap of the soot continuum with $_2O$ and CO_2 lines. The equations were of extinction coefficients, as follows:

Input	Model	Output
Equilibrium Carbon (unoxidized)	Carbon $\Longrightarrow$ Soot	Soot Concentration
Temperature	Soot + O_2 $\overset{k_{ox}}{\Longrightarrow}$ CO_2	

Figure II.C-2. Outline of Soot Formation Submodel.

$$K_{soot\ em} = (1.9 \times 10^3 \times f_v \times T_e\ (m^{-1}) \qquad \text{(II.C-1a)}$$

$$K_{soot\ abs} = (1.9 \times 10^3 \times f_v \times T_b\ (m^{-1}) \qquad \text{(II.C-1b)}$$

where f_v is the volume fraction, and T_e, T_b are the appropriate temperatures, in Kelvin, for emission and absorption, respectively. The correction terms for the overlap of soot and vapor radiation features are described below.

Hottel and Sarofim (1967) describe a correction due to such overlap, $\Delta\epsilon$, (their Eq. 6-58) as

$$\Delta\epsilon = \sum_i \epsilon_i - [1 - \pi_i\ (1-\epsilon_i)] \qquad \text{(II.C-2)}$$

With a three component model for flame radiation (soot, H_2O, and CO_2), and with the correction due to the overlap of CO_2 and H_2O lines already included in PCGC-2, the additional correction simplifies to two pairwise corrections, for soot-CO_2 and soot-H_2O, respectively.

In that case, Eq. II.C-2 simplifies to

$$\Delta\epsilon_{soot,\ CO2} = \epsilon_{soot} \times \epsilon_{CO2} \qquad \text{(II.C-3)}$$

and

$$\Delta\epsilon_{soot,\ H2O} = \epsilon_{soot} \times \epsilon_{H2O} \qquad \text{(II.C-4)}$$

However, Eq. II.C-2 only applies if all but one of the species is a grey-body radiator; not the case for soot. In this section, the proper calculation for the correction term is described, and it is shown that Eqs. II.C-3 and II.C-4 calculate the correction to within 4% for all temperatures and concentrations of interest.

The optical constants of soot from Habib and Vervisch (1988) were used them to calculate the soot absorption constant, k

$$k_{v,s} = \frac{36\pi \; x \; n_v \; K_v \;\; v}{(n_v^2 - k_v^2 + 2)^2 + 4 \; n_v^2 \; k_v^2} \qquad \text{(II.C-5)}$$

and the emissivity, ϵ for eight values of f_v between 5 X 10 $^{-6}$ and 5 X 10^{-4}.

$$\epsilon_{v,s}(f) = 1 - e\,[\,- k_{v,s} \; x \; f_v] \qquad \text{(II.C-6)}$$

For each f_v, "average" (as opposed to "spectral") quantities were calculated.

$$\epsilon_s(F) = \frac{\int \epsilon_{v,s}(f) \; R^b{}_v \; d_v}{\int R^b{}_v \; dv} \qquad \text{(II.C-7)}$$

where $R^b{}_v$ is the Planck function. These ϵ's were calculated for temperatures of 1500 K, 1800 K and 2100 K.

From measured absorbance spectra of water, A_v, and seven values of water concentration, X_ω, the emissivity of water vapor was calculated.

$$\epsilon_{v,s-w} = 1 - \exp\,[-K_{v,s} f_v + A_{v,\omega} \; X_\omega] \qquad \text{(II.C-8)}$$

and hence average emissivity

$$\frac{\epsilon_\omega = \int \epsilon_{v,\omega} \; R^b{}_v \; d_v}{\int R^b{}_v \; d_v} \qquad \text{(II.C-9)}$$

In similar fashion $\epsilon_{v,\,CO2}$ and ϵ_{CO2} for carbon dioxide were calculated. Finally, the emissivities, $\epsilon_{s,\omega}$ and $\epsilon_{s,CO2}$, for soot-water and soot-CO_2, respectively, were calculated.

For soot-water:

$$\epsilon_{v,s-w} = 1 - \exp\,[-\; K_{v,s} \; f_v + A_{v,\omega} \; X_\omega] \qquad \text{(II.C-10)}$$

$$\epsilon_{av,s-w} = \frac{\int \epsilon_{v,s-w} R^b{}_v \, d_v}{\int R^b{}_v \, d_v} \qquad \text{(II.C-11}$$

The correction,

$$\Delta \epsilon_{s-w} = \epsilon_{av,s-w} - \epsilon_{soot} - \epsilon_{water} \qquad \text{(II.C-12)}$$

and this correction was compared with the prediction of Eq. II.C-4 by taking the ratio

$$\Delta\epsilon_{s-w} / \Delta \epsilon_{soot-H2O} = \Delta\epsilon_{s-w} / \epsilon_{CO2} X \epsilon_{soot} \qquad \text{(II.C-13)}$$

A similar calculation was done for soot-H_2O.

The ratios are plotted as "spectra" with the x-value representing different combinations of f_v, X (or ϵ_{soot}, ϵ_{CO2}) in Figs. II.C-3 and II.C-4. For one value of X_{CO2}, f_v is changed over its range, giving rise to the down sloping line at the left of Fig. II.C-3. Then a new value of X_{CO2} is chosen, and the cycle of f_v repeated for this value, and so on for the seven values of X_{CO2}. The results show that the simple correction of Eqs. II.C-3 and II.C-4 is correct to within 5%, and that is the correction which we recommend. It turns out that the water and CO_2 bands are sufficiently close to the location of the average wavelength of the soot radiation that the soot acts like a grey-body.

Plans

Continue work with BYU on modeling the TWR coal flame experiments. Complete definition of submodels for ignition and soot formation.

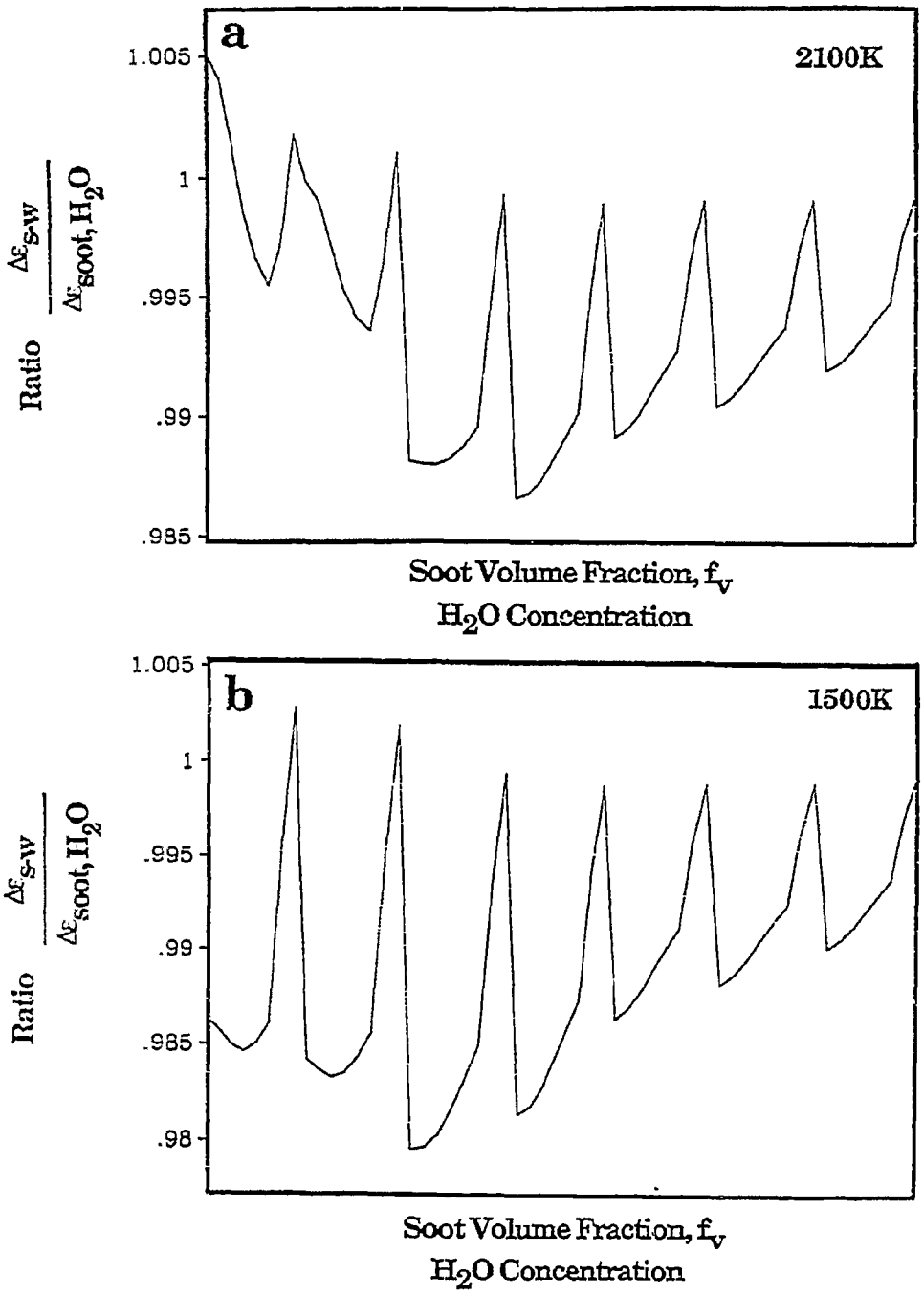

Figure II.C-3. Ratio of Correction Factors for Soot and CO_2 at a) 2100K and b) 1500K

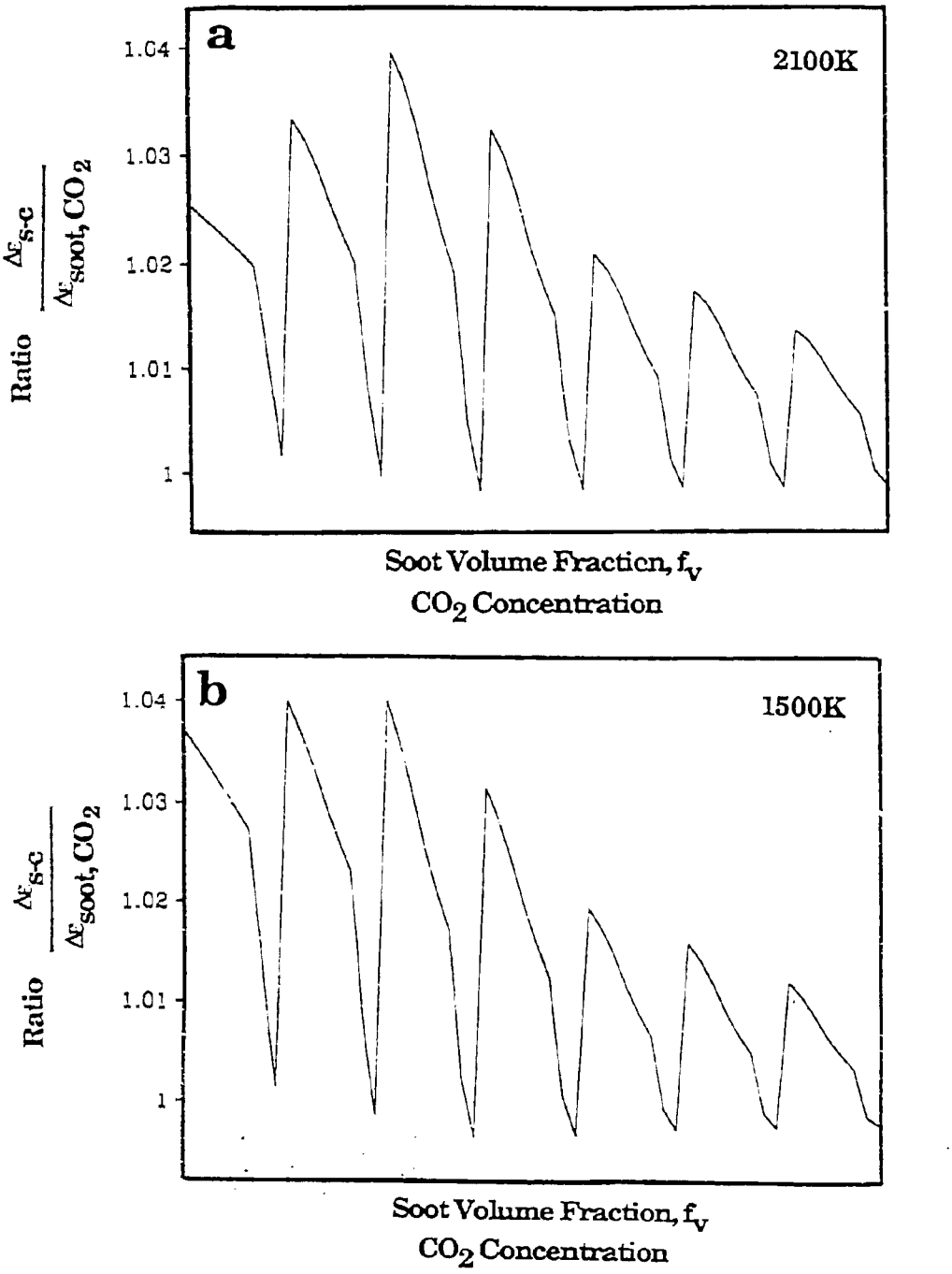

Figure II.C-4. Ratio of Correction Factors for Soot and H_2O at a) 2100K and b) 1500K.

II.D. SUBTASK 2.d. - ASH PHYSICS AND CHEMISTRY SUBMODEL

Senior Investigator - James Markham
Advanced Fuel Research, Inc.
87 Church Street, East Hartford, CT 06108
(203) 528-9806

Objective

The objective of this task is to develop and validate, by comparison with laboratory experiments, an integrated and compatible submodel to describe the ash physics and chemistry during coal conversion processes. AFR will provide the submodel to BYU together with assistance for its implementation into the BYU PCGC-2 comprehensive code. To accomplish the overall objective, the following specific objectives are: 1) to develop an understanding of the mineral matter phase transformations during ashing and slagging in coal conversion; 2) to investigate the catalytic effect of mineral matter on coal conversion processes.

Accomplishments

Under this subtask, a model for ash chemistry and physics was outlined. The inputs will be the starting mineral concentrations and size distributions while the outputs will be the composition and size distribution of the fly ash. An outline of the proposed submodel for ash chemistry and physics is shown in Fig. II.D-1. Because of the complexity of this problem and the large amount of DOE and NSF supported work being done elsewhere, this submodel will primarily be an integration of work done outside AFR.

Plans

Continue work on submodel for ash chemistry and physics.

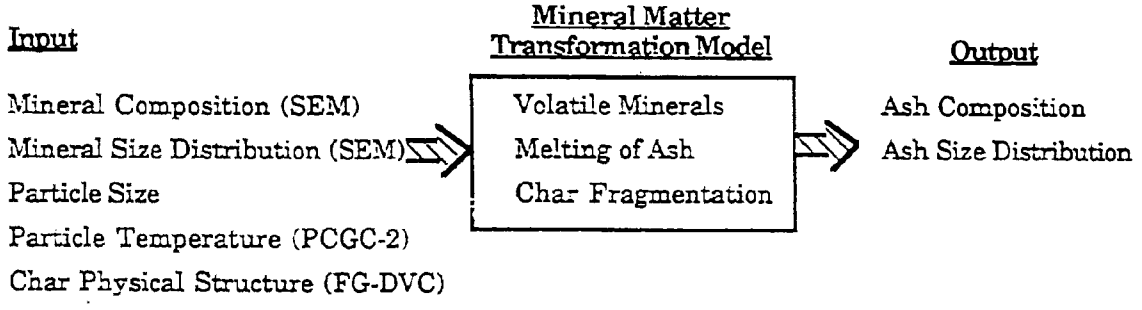

Figure II.D-1. Outline of Ash Physics And Chemistry Submodel.

II.E. SUBTASK 2.e. - LARGE PARTICLE/THICK BED SUBMODELS

Senior Investigator - Michael A. Serio
Advanced Fuel Research, Inc.
87 Church Street
East Hartford, CT 06108
(203) 528-9806

Objective

The objectives of this task are to develop or adapt advanced physics and chemistry submodels for the reactions of "large" coal particles (i.e., particles with significant heat and/or mass transport limitations) as well as thick beds (multiple particle layers) and to validate the submodels by comparison with laboratory scale experiments. The result will be coal chemistry and physics submodels which can be integrated into the fixed-bed (or moving-bed) gasifier code to be developed by BYU in Subtask 3.b. Consequently, this task will be closely coordinated with Subtask 3.b.

Accomplishments

The work on the modified AFR fixed-bed reactor (FBR) system continued. It includes two independently heated stages. The reactor system was assembled and tested and was used for lignin pyrolysis experiments under independent funding. It appears to work as planned. A redesign of the upper reactor chamber was required in order to eliminate a tar deposition problem. As expected, the quantitation of gas and tar is much better than in the old system and a wider range of sample sizes and flow rates can be used. Some problems were encountered with the software used to quantify the IR data, but these appear to have been resolved.

In the latter part of the year, a problem occurred with the FT-IR spectrometer that is being used to monitor volatiles evolution for the fixed bed reactor system. The spectrometer sustained some water damage to the beam splitters due to water being present in the purge lines. However, we should still be able to use the reactor system to generate validation data for the tar repolymerization model since the tar yield can be determined gravimetrically.

Under this subtask, a model for the repolymerization of tar in fixed bed gasifiers will be developed. The relatively low yield of tar from these systems is believed to be the result of recondensation of tar in the top of the bed which carries the tars back into the bed where they can be repolymerized into char or cracked into gas. A key parameter will be the gas exit temperature at the top of the bed. The model to be developed will be based on experimental data from the above-mentioned two-stage fixed-bed reactor system at AFR, as well as data from the literature. The model inputs will be the tar yield and tar molecular weight distribution (MWD) from the standard FG-DVC model. The outputs will be the actual tar yield, tar MWD, char yield and gas yield as a function of the bed conditions. The model is being formulated based on an analogy to gas adsorption processes in fixed beds. The primary difference in the case of a moving bed gasifier is the relatively large temperature difference between the gas and solid phases and the fact that the bed is not stationary. Work was completed on a compilation of literature data that can be used to help validate the tar repolymerization model.

Tar Repolymerization Submodel

Under this subtask, a model for the repolymerization of tar (Fig. II.E-1) in fixed bed gasifiers will be developed. The relatively low yield of tar from these systems is believed to be the result of recondensation of tar in the top of the bed which carries the tars back into the bed where they can be repolymerized into char or cracked into gas. A key parameter will be the gas exit temperature at the top of the bed. The model to be developed will be based on experimental data from a recently developed two-stage fixed-bed reactor system at AFR, as well as data from the literature. The model inputs will be the tar yield and tar molecular weight distribution (MWD) from the standard FG-DVC model. The outputs will be the actual tar yield, tar MWD, char yield and gas yield as a function of the bed conditions. The model is being formulated based on an analogy to gas adsorption processes in fixed beds. The primary difference in the case of a moving bed gasifier is the relatively large temperature difference between the gas and solid phases and the fact that the bed is not stationary.

The basis for the model approach will be the theory that has been developed to describe the operation of fixed-bed sorption devices for purification of gas

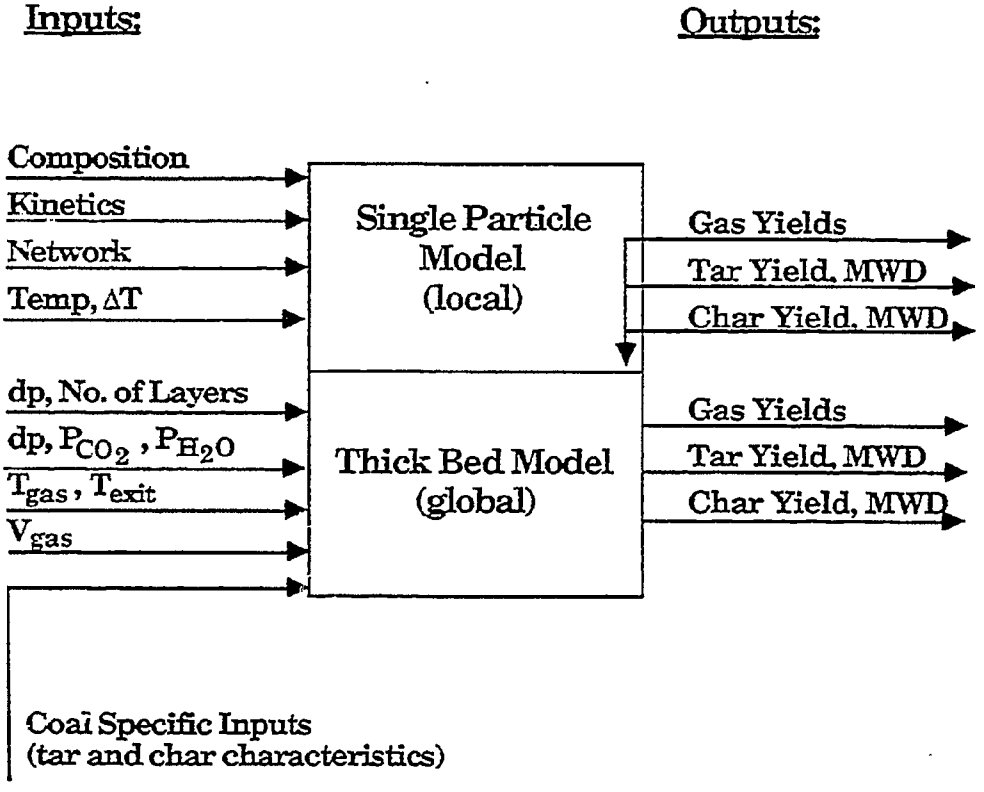

Figure II.E-1. Outline of Tar Repolymerization Submodel.

and liquid streams. The additional complications are that the bed is not isothermal and the particles are devolatilizing to produce additional material which can readsorb downstream. An important parameter is the gas temperature since this determines whether the tar will condense to form an aerosol. Once the tar is in this form, it can be removed by "filtration" on the bed particles. If the tar is in the vapor phase it must physically absorb onto the particle surface, a process which can be described (at equilibrium) by the Langmuir isotherm. The key physical processes based on our current understanding are summarized in Figure II.E-2.

The condensation/evaporation cycles of the tar in the bed are similar to what occurs in a reflux column. As a first approximation, the amount of tar which should be in the liquid phase at the top of the bed will be calculated and the assumption will be made that all of it is removed. How well this works will depend on how accurately the vapor-liquid equilibrium for tar is described and the efficiency of the tar aerosol filtration process that occurs in the bed.

A compilation was made of literature data that can be used to help validate the model. The focus has been on data for the Pittsburgh seam coal which shows the change in tar yield and/or composition with variations in heating rate, bed depth, flow rate, particle size, and reactor type.

Plans

Complete development of tar repolymerization submodel. Continue development of single particle model with BYU.

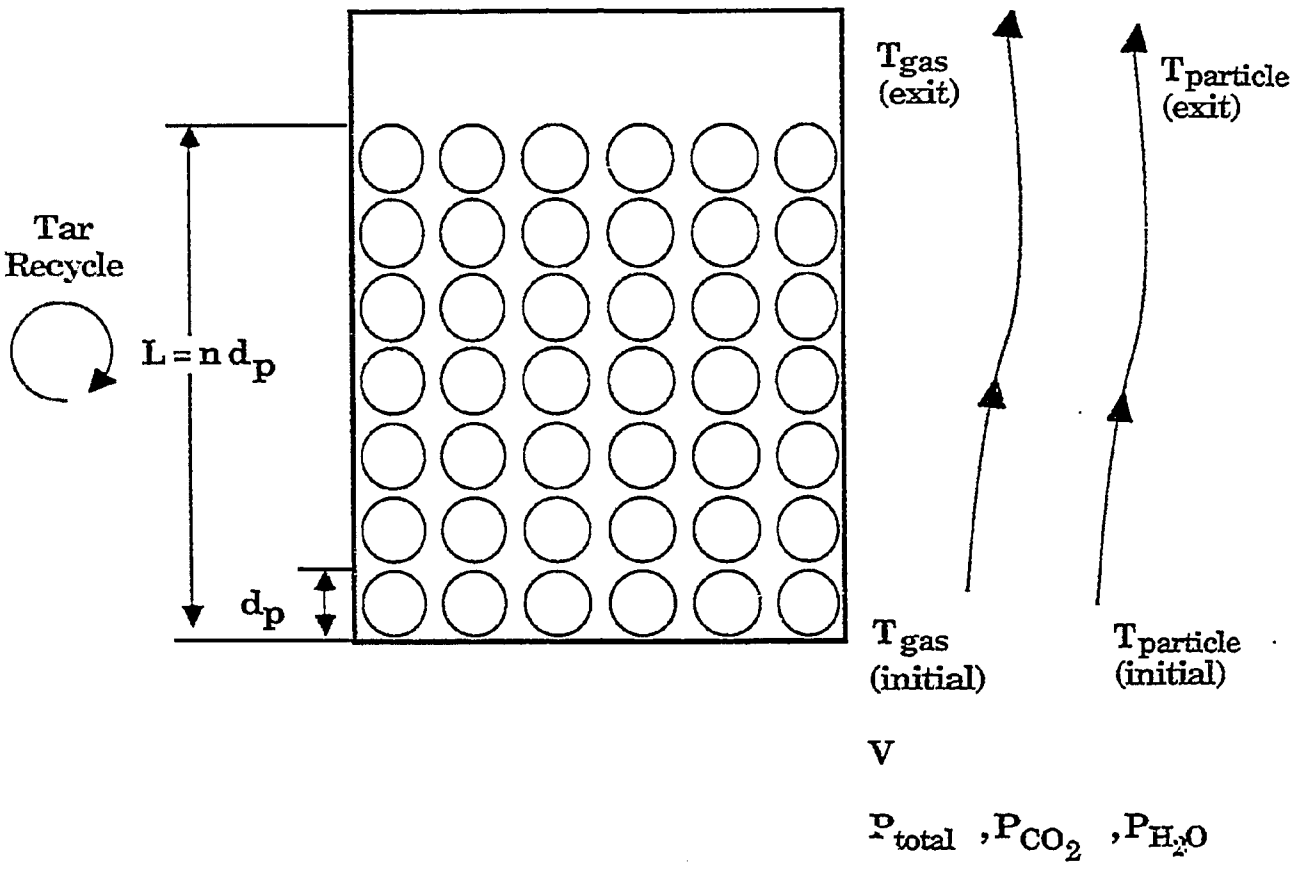

Figure II.E-2. Devolatilization in Fixed-Bed Reactors.

II.F. SUBTASK 2.F. - LARGE PARTICLE OXIDATION AT HIGH PRESSURES

Senior Investigators: Angus U. Blackham and Geoffrey J. Germane
Brigham Young University
Provo, Utah 84602
(801) 378-2355 and 6536

Student Research Assistants: Ken Bateman, Gary Pehrson and Wade Riser

Objectives

The overall objective for this subtask is to provide data for the reaction rates of large char particles of interest to fixed-bed coal gasification and combustion systems operating at pressure.

The specific objectives for this past year include:

1. Review appropriate literature.
2. Design and initiate the construction of the cantilever beam insert.
3. Continue evaluation of analytical procedures.
4. Conduct additional preliminary oxidation experiments.

Accomplishments

The two components of this subtask are: 1) reactor design, fabrication, and preliminary data; 2) experimental reaction rate data for chars from five coals. The decision was made to develop a cantilever beam insert to be connected to an optical access port of the HPCP reactor.

During this past year, a ceramic tube was attached to the force transducer discussed in earlier reports. To the other end of the ceramic tube was attached a platinum balance pan for supporting the large char particle. A two-axis slide was considered for moving this cantilever beam assembly so that char particle is properly positioned in the flow path of the reactor gas. The design details of the pressure chamber to house this assembly were completed and the necessary materials are being assembled.

A simple reactor system to operate at atmospheric pressure was assembled to perform preliminary tests of the force transducer and cantilever beam unit. The reactor consists of a quartz tube (2.5 cm diameter) with a 2 cm x 3 cm rectangular window through which the platinum balance pan can pass. This quartz tube was placed in a tube furnace mounted vertically. The experimental run made with this system was not successful because a sufficiently high temperature could not be maintained to oxidize the char particle and follow its mass loss.

A different arrangement was used to follow the response of the force transducer to mass loss. A small pipet from which alumina particles could drop was supported at the end of the cantilever beam. The mass loss was then followed by the response of the force transducer. Satisfactory response was obtained.

Some additional preliminary oxidation runs in platinum crucibles were also made. In addition to the runs previously made with a Utah bituminous coal, runs this year were made with five additional coals--North Dakota lignite, Wyoming subbituminous, Illinois #6, Pittsburgh #8, and a Colorado coal.

Reactor Design

Cantilever Beam Insert – The cantilever beam insert (CBI) was designed to give mass loss readings and to precisely locate the sample during oxidation experiments using 0.5-1.0 cm char particles. The three components of the CBI are: a) a balance unit; b) a two-axis slide; and c) a heat-shielded, water-cooled valve. The entire assembly will be bolted directly to the HPCP reactor of Subtask 2b.

The balance unit measures the mass loss of the particles as they oxidize in the HPCP reactor. It consists of a force transducer, a ceramic cantilever beam, and a platinum, wire-mesh, sample basket. The basket is secured to the cantilever beam and extends into the reactor tube through one of the optical access ports of the HPCP reactor.

In order to test multiple samples during each run, a mechanism has been designed to insert and retract the samples from the reactor tube. The balance unit is mounted on a mobile platform. This platform is capable of moving along two axes. First, the entire platform moves toward and away from the reactor tube. This motion, accurate to $\pm$ 0.001 in, allows for sample insertion into and retraction from the reactive environment. The second motion is perpendicular to the first and in the vertical direction. With this capability, the particle can be moved while being oxidized, thus permitting several temperature readings along the surface of the particle. Both movements will be accomplished through the use of motor-driven ball screws.

An aluminum, water-cooled gate valve will be mounted between the HPCP reactor and CBI housing. With the valve in the open position, the cantilever beam and platinum-mesh basket can extend through the opening.

Force Transducer – A few tests were made with the load cell (force transducer) to study its properties. Measurements of maximum load, stability, and sensitivity were made as functions of lever arm length. Lever arms of 10, 15 and 20 cm were studied. The maximum loads measured were 25, 22 and 19 g,

respectively. The drift of the transducer was a maximum at 10 mg/hr, showing good stability at maximum loads. The sensitivity was approximately 3 mg per division at each length.

A simple reactor system to operate at atmospheric pressure was then assembled as shown schematically in Figure II.F-1. The purpose of this system was to provide information and experience with the force transducer-cantilever beam unit while the high-pressure housing was being constructed. Some experience with this simple system was obtained with the gas flowing at ambient temperature, which showed the response from the transducer to be sufficiently stable. However, when the quartz tube was heated, the heat loss below the end of the furnace was too much to maintain a temperature high enough for oxidation of a supported char particle placed through the window in the quartz tube. Therefore, there was no loss of mass for the force transducer to measure. Accordingly, it was necessary to use a different experimental setup to show that the transducer could perform mass-loss measurements at the desired sensitivity and accuracy.

Mass-loss tests were then performed on the force transducer by hanging a small pipet on the end of the cantilever beam. One end of the cantilever beam was inserted into a stainless steel block fixed in the side of the force transducer. The block was necessary to eliminate problems that arose due to twisting the strain gauges in the transducer. The twist caused the transducer to give incorrect mass readings. In order to perform the tests, a quantity of dense alumina was placed in the pipet. A reading on the transducer was recorded, and the alumina was then allowed to fall from the pipet. The alumina was then measured, and another reading was taken on the transducer. Thus, the total mass of alumina that escaped the pipette was known, and the total number of counts read by the transducer was determined from the before and after readings. The results of tests performed at 10 cm from the transducer are recorded in Table II.F-1. The counts/gram at the two different scale factor settings of the instrument is within 3% for triplicate measurements.

Table II. F-1. Experimental results from transducer mass-loss tests.

Scale Factor	Total Mass of Alumina (grams)	Total Counts on Transducer	Counts/gram
1	3.333	395	118.5
1	1.670	202	120.9
1	1.270	154	121.2
2	3.318	818	246.5
2	4.111	1000	243.2
2	2.525	614	243.1

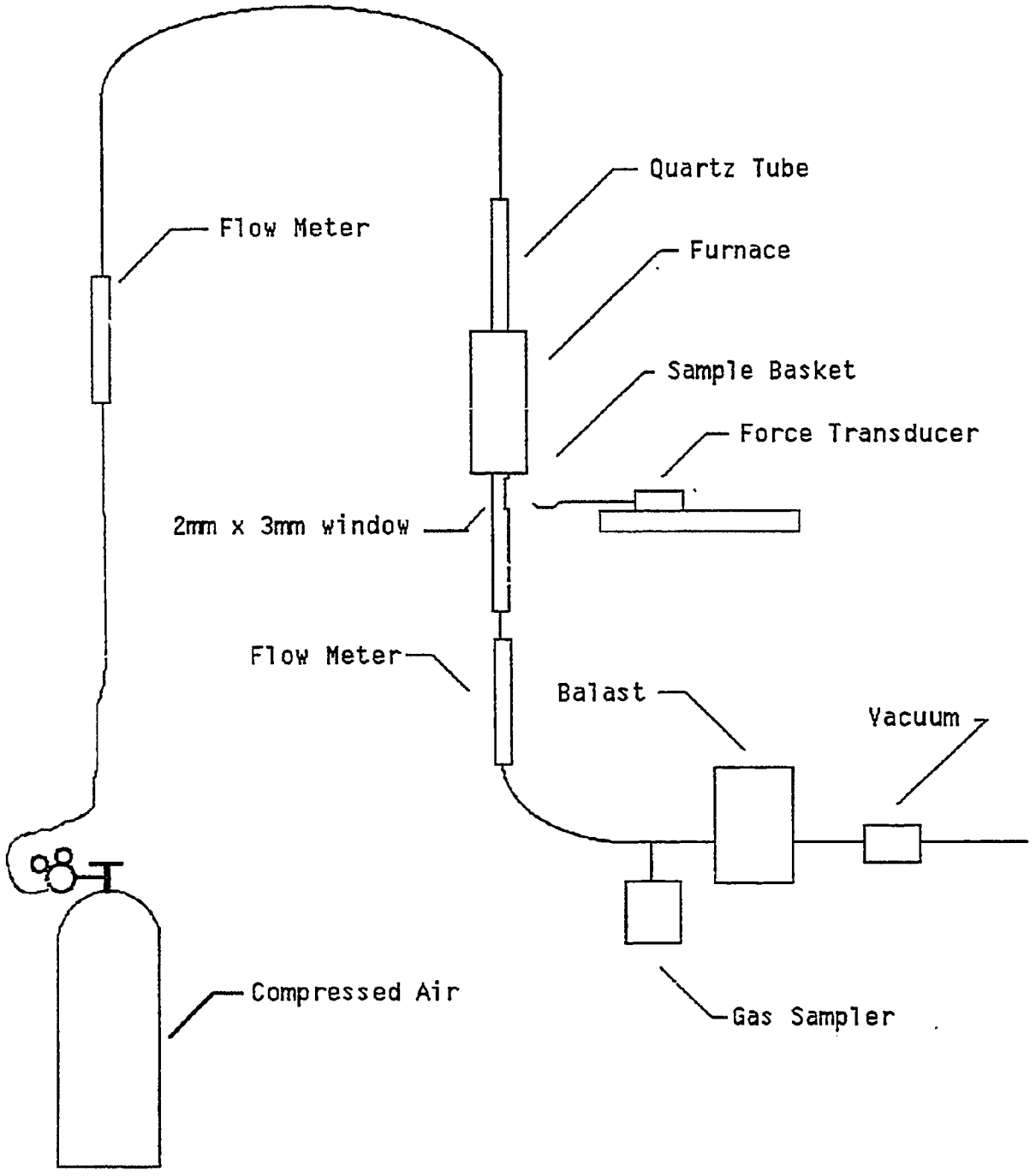

Figure II.F-1 A simple reactor system at atmospheric pressure for oxidizing large char particles.

Analytical Methods - The analysis of CO and CO_2 can now be performed at room temperature using a chromatographic column consisting of concentric columns. This column was tested on a Varian 3200 gas chromatograph with a standard comprised of known volumes of CO, CO_2, CH_4, and H_2 gases. The column successfully separated all peaks associated with the standard. Therefore, CO and CO_2 can be determined at the concentrations of interest in this study.

Oxidation Measurements

Preliminary Large Particle Oxidation Measurements - For the principal purpose of providing experience in experimental procedures associated with large coal particles, a series of sets of large particles of a Utah bituminous coal have been devolatilized and oxidized in platinum crucibles in air. These results were given in the Fourth Annual Report (Solomon, et. al, 1990). A lump of coal was crushed to provide some particles with dimensions of about 0.5-1.0 cm on a side. The first set (six particles) were heated with Meker burners. A second set (six particles) were heated in a muffle furnace. Then four sets of samples (four particles in each set) were heated at different temperatures in the muffle furnace.

An additional study of the data of these last four sets was made resulting in a correlation not noted in the earlier report. Graphs of each of the four sets of data were prepared with the log of the normalized mass remaining for each particle plotted against the time of oxidation. The slope of each curve, therefore, is an indication of mass reactivity. The average mass reactivities for the sixteen particles reported in Table II.F-2 of the Fourth Annual Report are included in Figure II.F-2 along with the initial mass of each large particle. Our expectation was that average mass reactivity would correlate somewhat with temperature of oxidation. There was a slight indication of this, because the highest observed mass reactivity was at the highest oxidation temperature (0.112 min^{-1} at 1420-1470 K). However the spread in reactivities of the four particles in this temperature range was quite broad (0.041 to 0.112 min^{-1}) and appeared to be a function of the initial particle mass. When the average mass reactivity for all sixteen particles was plotted against initial particle mass, the correlation presented in Figure II.F-3 was obtained. All four temperature ranges are represented in the cluster of points for initial masses greater than 1 gram. Therefore in the overall temperature range for these oxidation tests, mass reactivity does not appear to change significantly with temperature but decreases with increasing particle mass. This observation suggests that the factor of most influence under these conditions is the movement of gas through the developing ash residue. This results indicates that further experiments of this preliminary nature with platinum crucibles at

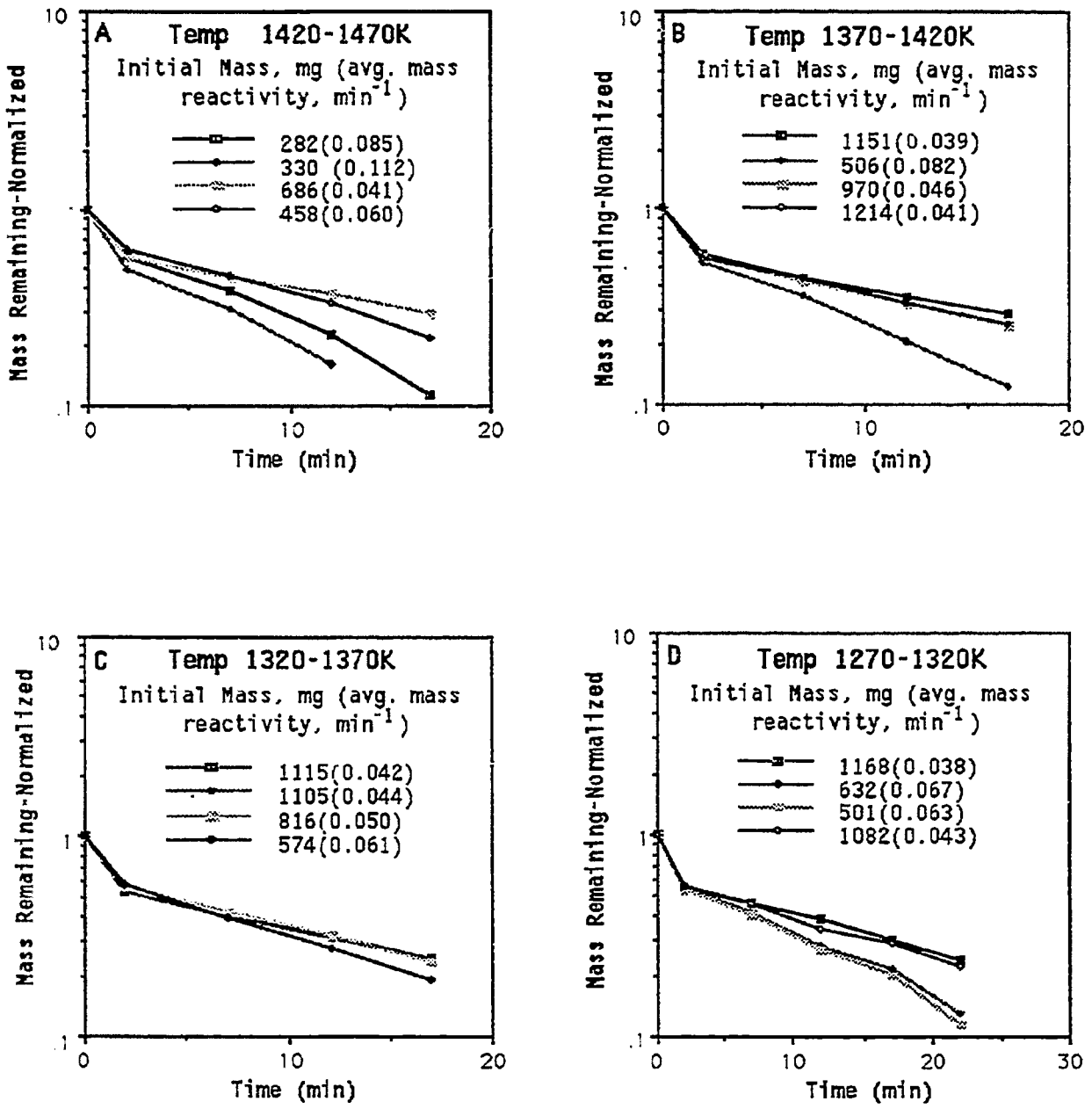

Figure II.F-2 Mass loss for large particles of utah bituminous coal devolatilizing and oxidizing in air at atmospheric pressure.

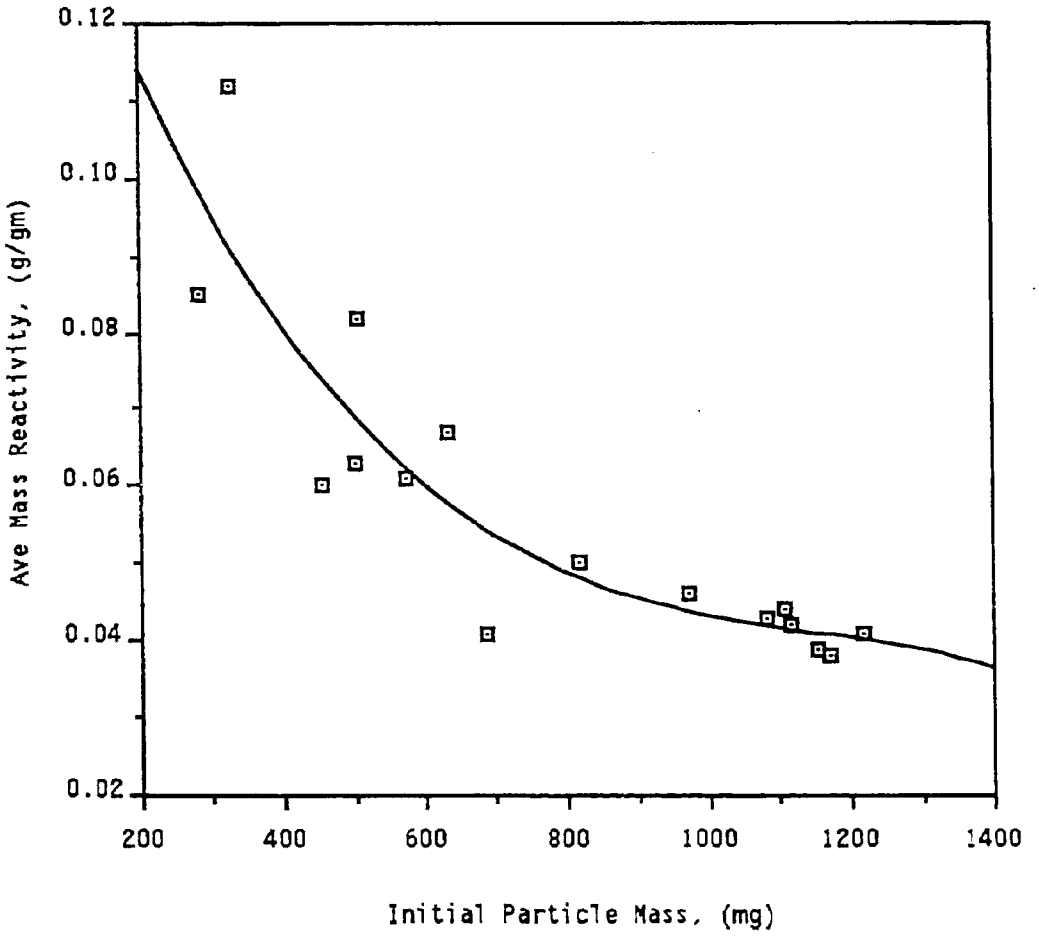

Figure II.F-3 Effect of Initial Mass of Utah Bituminous Coal Particles on Average Mass Reactivity

atmospheric pressure will help in determining the issues that need to be considered as plans are being made for measurements at high pressure in the facility to be constructed for this subtask.

Later, similar measurements were extended to additional coals. A set of three particles of a Colorado coal was devolatilized and oxidized in air with Meker burners. A set of three particles, one from each of North Dakota lignite, Wyoming subbituminous and Illinois #6 coals, was devolatilized and oxidized in air with Meker burners. An additional run was made with a large particle pressed into a thick disk about 1 cm in diameter and 0.5 cm high from a sample of pulverized Pittsburgh #8 coal. The rationale for measurements of pressed pulverized coal particles is to be able to prepare large particles of somewhat uniform composition of a single coal or char if needed. Some difficulty was experienced while removing the disk from the die, and it cracked. However, a piece of sufficient size was obtained to devolatilize it to a swollen char particle for the oxidation run.

The results of these additional tests are given in Figure II.F-4. The average mass reactivities of the Colorado coal chars are similar to those of the Utah bituminous coal reported previously and also show the same dependance of mass reactivity on particle size--the smaller particles having a larger mass reactivity. The large particles of the North Dakota lignite and the Wyoming subbituminous coals show results similar to the Utah bituminous coal. However, the particle of the Illinois #6 coal is distinctly lower in reactivity. For this coal, the developing ash particle maintained the same shape as the char particle as the burnout progressed, rather than crumbling as the other coals did.

Plans

During the next quarter, the cantilever beam insert will be tested for its accuracy and reproducibility in positioning the sample char particle in the reactor. The initial measurements of rates of oxidation of the selected chars will then be made at pressures above atmospheric pressure. Additional preliminary oxidation runs will be made in air in platinum crucibles.

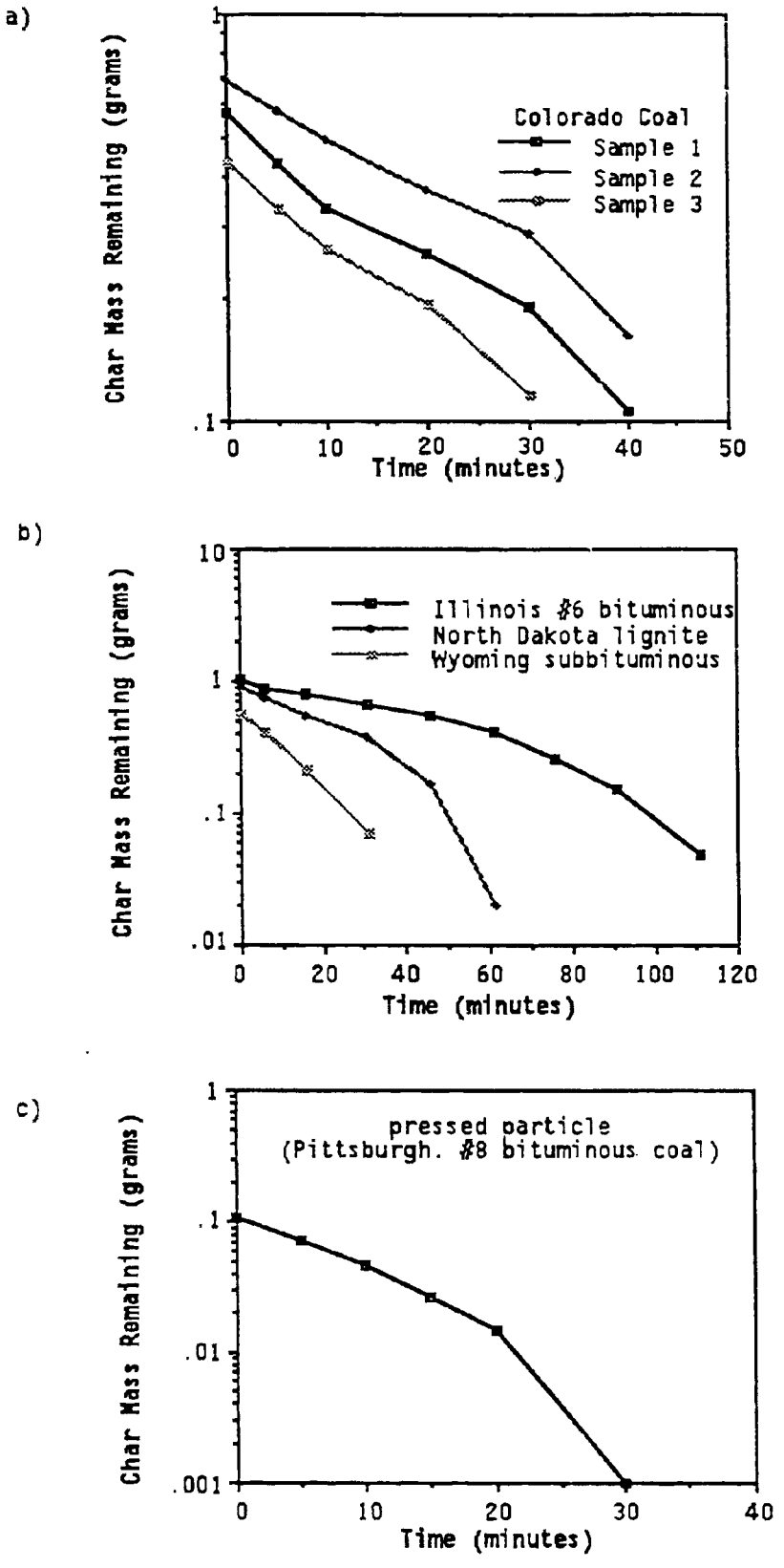

Figure II.F-4 Mass loss for large devolatilized coal particles oxidizing in air at 1150 K.

II.G. SUBTASK 2.G. - SO_x/NO_x SUBMODEL DEVELOPMENT

Senior Investigators: L. Douglas Smoot and B. Scott Brewster
Brigham Young University
Provo, Utah 84602
(801) 378-4326 and (801) 378-6240

Research Assistant: Richard D. Boardman

Objectives

The objectives of this subtask are 1) to extend an existing pollutant submodel in PCGC-2 for predicting NO_x formation and destruction to include thermal NO, 2) to extend the submodel to include SO_x reactions and SO_x-sorbent reactions, and 3) to consider the effects of fuel-rich conditions and high pressure on sulfur and nitrogen chemistry in pulverized-fuel systems.

Accomplishments

During the last year, the NO_x and SO_x/sorbent reactions submodels were incorporated into the final product code version. Additional insight into the thermal NO submodel was obtained. Evaluation of the SO_x/sorbent reactions submodel was initiated. A benchmark case was used to demonstrate the sorbent capture submodel and to investigate the effects of Ca/S ratio on SO_2 reduction efficiency. Coal graphics routines were modified to include sorbent particles.

Thermal NO

The expression used to estimate oxygen atom concentration which is required by the following simplified Zel'dovich mechanism for thermal NO formation (Westenberg, 1971) was further evaluated:

$$\frac{d[NO]}{dt} = 2k_{A6}[O][N_2] \quad \text{gmole cm}^{-3}\,\text{s}^{-1} \qquad \text{(II.G-1)}$$

This expression is obtained by assuming the formation reactions of the three-step Zel'dovich mechanism are irreversible and OH concentrations are small.

Two quasi-equilibrium expressions have been evaluated in the submodel for calculating oxygen atom concentration. Oxygen equilibrium (Eq. II.G-2) has been recommended for fuel-lean zones in the combustor while carbon equilibrium (Eq.

II.G-3) has been suggested for fuel-rich regions where primary fuel oxidation occurs.

$$[O] = \{K_{eq}[O_2]\}^{1/2} \qquad \text{(II.G-2)}$$

$$[O] = K_{eq} \frac{[O_2][CO]}{[CO_2]} \qquad \text{(II.G-3)}$$

The sensitivity of the model to these expressions was evaluated. Figure II.G-1 compares the predicted NO concentrations with the experimental values measured (with independent funding) in the ACERC controlled-profile reactor over a narrow range of overall fuel-to-oxidizer equivalence ratios with a secondary air swirl number of 1.5. Predictions used either oxygen equilibrium (Eq. II.G-2) or carbon equilibrium (Eq. II.G-3) to predict oxygen atom concentration. Thermal NO is overpredicted at lower equivalence ratios (fuel-lean conditions) when carbon equilibrium is assumed. When oxygen equilibrium is assumed, thermal NO is slightly underpredicted. Predictions were not made for higher equivalence ratios where carbon equilibrium may give more accurate predictions. However, these results should provide guidance for using the NO model for practical burner conditions, which are normally fuel-lean. Further work is needed for fuel-rich conditions.

SO_x/Sorbent Reactions

General Description - The SO_x/sorbent reactions submodel consists of three components: 1) SO_2 formation, 2) sorbent particle injection and tracking, and 3) SO_2 capture. A brief description of the submodel was given in the 4th Annual Report (Boardman et al., 1990). Figure II.G-2 illustrates the solution algorithm, which is called after converging the major gas and particle equations. As individual sorbent particle trajectories are calculated, the SO_2 capture at each time step is predicted by the shrinking-core grain model of Silcox (1985). Figure II.G-3 shows the steps contained in the sulfation model, which uses the equations listed in Table II.G-1. The reaction of sorbent with SO_2 is given by:

$$CaO + SO_2 + 1/2O_2 \rightarrow CaSO_4 \qquad \text{(II.G-4)}$$

The submodel predicts the loss (or sink) of SO_2 for each computational cell. A continuity equation for SO_2 gives a revised concentration field. Concentrations

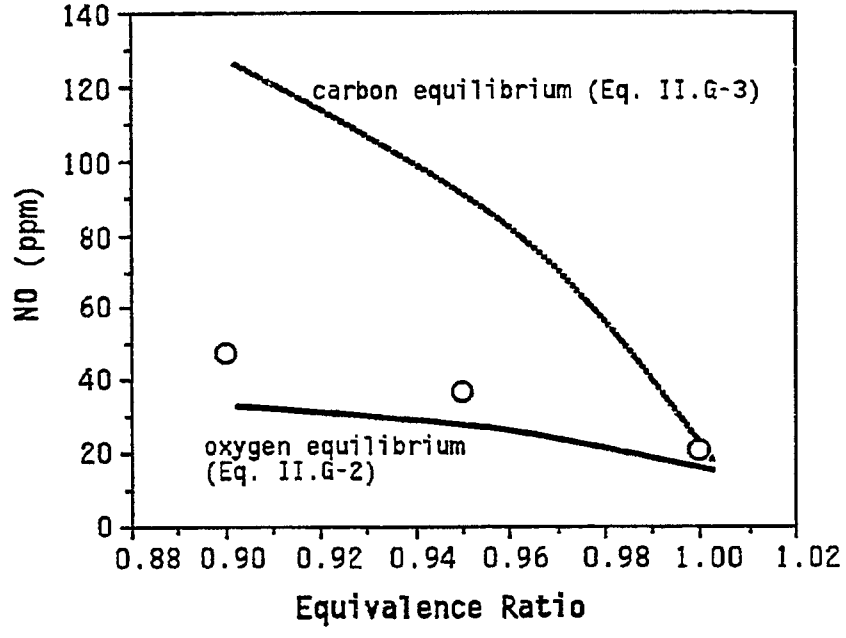

Figure II. G-1. Comparison of prediction methods used to estimate atomic oxygen concentrations with measured data (circles) for natural gas combustion in the ACERC controlled-profile reactor: Secondary swirl no. = 1.5; heating rate = 147 kW.

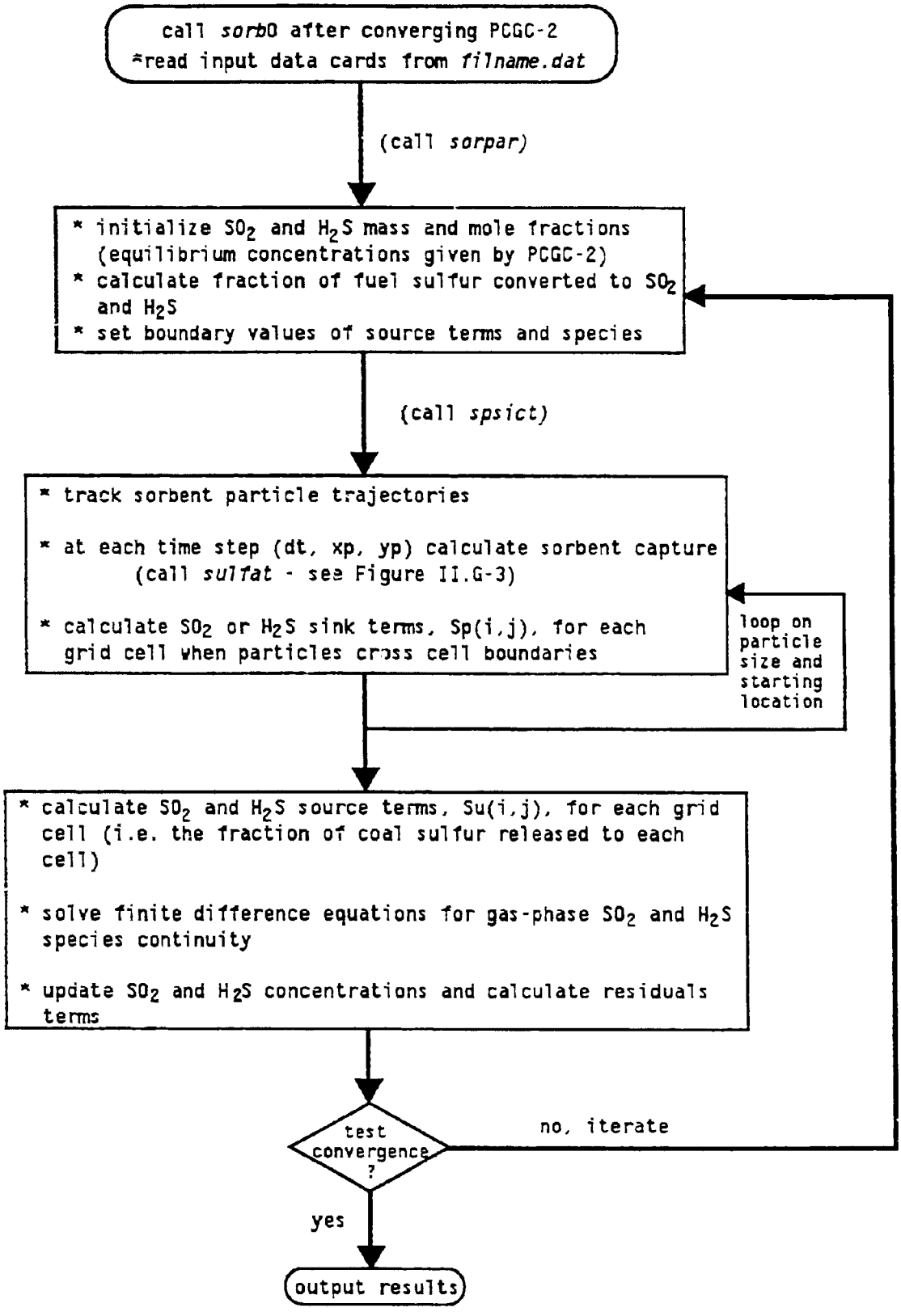

Figure II.G-2. SO_x/sorbent reaction submodel solution algorithm.

sulfat (calculation of sorbent sulfation)
Called from *spsict* at time step along particle trajectory path

initialization
* select number of subshells to describe sorbent particles
* calculate the radius of grains based on BET surface area of sorbent particles
* at each particle starting location, set initial conversion of grains to 1E-20 to avoid division by zero at first time step
  Also, set radius of unreacted CaO to (1E-20)*(initial grain radius) for each subshell and assign the concentration profiles of SO_2 and H_2S through the particles
* select order of sulfation reaction

at each time step (xp, yp, dt)
* calculate gas temperature, $[SO_2]$, and $[H_2S]$ by 2-D interpolation
* set the concentration of SO_2 and H_2S at the sorbent particles surface (node n) equal to $[SO_2]$, and $[H_2S]$, the local gas concentration
* calculate the interfacial area available for reaction at each subshell
* calculate the particle void fraction as a function of sorbent particle radius
* calculate the extended grain radius (due to increase in the molar volume of $CaSO_4$ product) at each subshell
* calculate bulk and Knudsen diffusivity at each subshell
* calculate the effective diffusivity at each subshell
* calculate product layer diffusivity at each subshell
* calculate the reaction rate constant (assumed to be constant throughout the sorbent particle since particles are isothermal)

calculate new concentration profiles through the sorbent particle using material balance differential equation

first-order reaction
* assemble coefficients for matrix solution
* use Thomas algorithm to solve tri-diagonal system of equation

half-order reaction
* assemble coefficents for matrix solution
* use Newton-Raphson technique to calculate concentration at each sorbent particle subshell

determine sorbent particle conversion due to reaction occurring during dt (differential time step)
* calculate change in grain radius due to reaction
* calculate conversion for each subshell
* obtain overall conversion for sorbent particle by summing individual subshell conversions
  conversion (integration procedure used)

return to *spsict*

Figure II.G-3. Sulfation model procedure outline. (See Table II.G-1 for equations).

Table II.G-1. Sorbent-Reaction Submodel Equation Set

Equation	Definition	Eq. No.§
$\frac{d^2[SO_2]}{dR^2}+\left(\frac{2}{R}+\frac{1}{D_{eff}}\frac{dD_{eff}}{dR}\right)\frac{d[SO_2]}{dR}-\frac{N}{D_{eff}}=0.$	Material balance on SO_2 in a spherical shell. Used to calculate $[SO_2]$ at each sorbent particle subshell.	4.7
$@R=0.;\ \frac{d[SO_2]}{dR}=0.$ $@R=R_p;\ [SO_2]_{R_p}=[SO_2]_{sp,yp,dt}$	Boundary conditions	4.9
$N=k_{1/2}A[SO_2]^{\frac{1}{2}}_{r_{cor(i)}}$	Half-order volumetric consumption rate	4.10
$N=k_1A[SO_2]^{1}_{r_{cor(i)}}$	First-order volumetric consumption rate	4.11
$A=3z(1-e_c)\frac{r^3}{r^3_{cor(i)}}$	Interfacial area available for reaction at ith subshell	4.15
$z=\left\{\frac{\rho_{CaO}}{\rho_{MgO}}\left(\frac{1}{W}-1\right)+1\right\}^{-1}$	Fraction of grains which are CaO	4.16
$W=\left\{1+\left(\frac{1-Y}{Y}\right)\left(\frac{M_{MgO}M_{CaCO_3}}{M_{MgCO_3}M_{CaO}}\right)\right\}^{-1}$	Weight fraction of CaO in the calcine on an "impurity-free" basis	4.17
$\frac{dr_{cor(i)}}{dt}=\left(\frac{-M_{CaO}}{\rho_{CaO}}\right)K_n[SO_2]^n_{r_{cor(i)}}$	Material balance on CaO at product-Ca? interface for nth order reaction	4.13 4.14
$[SO_2]_{r_{cor(i)}}=\frac{D_{sp}[SO_2]_{R_{(i)}}}{D_{sp}+K_1r_{cor(i)}\left(1-\frac{r_{cor(i)}}{r_{ext(i)}}\right)}$	Interfacial concentration for ith subshell for first-order reaction rate	4.23
$[SO_2]_{r_{cor(i)}}=\frac{2[SO_2]_{R_{(i)}}-\alpha-\left(-4[SO_2]_{R_{(i)}}\alpha+\alpha^2\right)^{\frac{1}{2}}}{2}$ $where,\ \alpha=-\left(\frac{K_{1/2}r_{cor(i)}}{D_{sp}}\right)^2\left(1-\frac{r_{cor(i)}}{r_{ext(i)}}\right)^2$	Interfacial concentration for ith subshell for half-order reaction rate	4.24
$r_{ext(i)}=\left\{\left(\frac{r_g^3-r_{cor(i)}}{1-e_s}\right)\left(\frac{\rho_{CaO}M_{CaSO_4}}{\rho_{CaSO_4}M_{CaO}}\right)+r^3_{cor(i)}\right\}^{\frac{1}{3}}$	Extended grain radius	4.26

Table II.G-1. Continued

Equation	Definition	Eq. No.§
$r_g = \frac{3}{\rho_{CaO}(BET\ surface\ area)}$	Initial grain radius	4.84
$e_x = 1-(1-e_s)\left\{1+\left(\frac{\left(\frac{a}{1-e_s}-1\right)X}{1+\frac{\rho_{CaO}(1-W)}{\rho_{MgO}W}}\right)\right\}$	Particle void fraction	4.28
$X_{R(i)} = 1-\left(\frac{r_{cor(i)}}{r_g}\right)^3$	Extent of grain conversion at ith subshell	4.27
$X(t) = \frac{3}{R_p^3}\int_0^{R_p} R_{(i)}^2 X_{R(i)} dR$	Overall conversion of sorbent particle	4.44
$K_1 = 291\exp\left(\frac{-7510}{T}\right) \quad cm\,sec^{-1}$	First-order reaction rate constant	4.79a
$K_{1/2} = 0.0307\exp\left(\frac{-6970}{T}\right) \quad gmol^{\frac{1}{2}}\,cm^{-\frac{1}{2}}\,sec^{-1}$	Half-order reaction rate constant	4.79b
$D_{eff} = \left(\frac{1}{\frac{1}{D_M}+\frac{1}{D_K}}\right)e_x^2$	Effective diffusivity	4.80
$D_M = \exp(1.66\ln(T)-11.3) \quad cm^2\,sec^{-1}$	Bulk diffusivity for SO_2-air binary-pair	-
$D_K = 19{,}400\frac{e_c}{\rho_{CaO}(\text{BET surface area})}\sqrt{\frac{T}{M_{SO_2}}} \quad cm^{-2}\,sec^{-1}$	Knudsen diffusion coefficient	4.82
$D_S = 0.0124\exp\left(\frac{-12{,}200}{T}\right) \quad cm^2\,sec^{-1}$	Product layer diffusion coefficient**	4.83

§ Equations reference number in Silcox (1985). Rate constants and diffusion coefficients derived by Silcox from experimental data as cited by Silcox (1985)
** Also see Table II.G-4 for product layer diffusion coefficient

of major species are assumed constant. The algorithm is iterative since the sulfation submodel is dependent on the concentration of SO_2.

A list of Fortran subroutines is given in Table II.G-2. A description of input data is given in Table II.G-3.

Key Assumptions - Key assumptions include the following:

1. Sulfur is released from the coal at a rate proportional to the total coal mass loss.

2. The gas (including sulfur species) is in local instantaneous equilibrium prior to SO_2 capture.

3. The sorbent particles are instantaneously calcined to CaO. Calcination gas (CO_2 in the case of $CaCO_3$ or H_2O in the case of $Ca(OH)_2$) may be added separately to the carrier gas.

4. Particle/gas slip is neglected in the convective component of sorbent particle velocity; the effects of the sorbent particles on gas velocity are neglected.

5. The sorbent particles are isothermal and in thermal equilibrium with the local gas; the effects of sorbent particles on the radiation fluxes are ignored.

6. Reaction of CaO with SO_2 is irreversible, either half- or first-order with respect to SO_2, and zero-order with respect to O_2.

7. As SO_2 is captured, its concentration is reduced correspondingly, but the remaining gas composition is not affected.

The assumption of instantaneous particle calcination deserves further comment. Silcox (1985) showed that this is a reasonable assumption for sorbents injected into high-temperature regions. His calculations showed that particle heat-up and calcination occur over a short period of time relative to the time required for sulfation by SO_2. Silcox also noted that thermodynamic considerations rule out simultaneous calcination and sulfation if the sorbent is injected into the burner zone. If the sorbent is injected downstream of the burner zone in cooler flame regions, then simultaneous calcination and sulfation can occur. A model to predict joint calcination and sulfation was developed by Milne et al. (1990), and the feasibility of including this model is being

Table II.G-2. Subroutines in the SO_x/Sorbent-Reaction Submodel

Subroutines	
Subroutine	**Description**
calcsj	Calculates sorbent particle number density
calso2	Solves finite difference equation for H_2S species continuity
calh2s	Solves finite difference equation for H_2S species continuity
sorb0	Reads in input data from *filename*.dat and initializes sorbent particle number density
sorpar	Main submodel driver, calculates source terms for SO_2 and H_2S (sulfur entering with the coal or gas inlet streams), determines if convergence is obtained prints out final results
spsict	Performs particle trajectory integration and calculates the capture of SO_2 and H_2S in each computational cell, also calculates sink terms for SO_2 and H_2S species continuity
sulfat	Calculates the change in conversion of calcined $CaCo_3$ particles to $CaSo_4$ according to the shrinking-core model of Silcox (1985)

Table II.G-3. SO_x/Sorbent-Reactions Submodel Data Input Description

Input in PCGC-2 *filename.dat*

```
****************************   PCSORB   ****************************
****************** SOX/H2S-SORBENT REACTIONS SUBMODEL ****************
     ***************************          ***********************
   3,1                                        !NSLS,NPSS
   0.0200, 1340.                              !SPLOAD,SPDEN
   0.0000,0.0000,0.0000,                      !YPS(ISL),ISL = 1,5
   20.00E-06,                                 !PDS(IPS),IPS = 1,3
   1.0000,                                    !PMFS(IPS),IPS = 1,5
   F    F                                     !LSPBUG,LYPS
   0.9500,0.0200,                             !YPSH,YPSL
   0.3500,                                    !PRKS(IPS),IPS = 1,5
```

Definition of Input data

Variable	Description
NSLS	number of starting location for sorbent particles
NPSS	number of particle sizes for sorbent particles
SPLOAD	sorbent particle loading (ratio of sorbent particle mass to the mass of gas in the primary inlet) (kg s^{-1})
SPDEN	sorbent particle density (*i.e.*, density of CaO) (kg m^{-3})
YPS(ISL)	paricle starting location for isl particle trajectory
PDS(IPS)	particle diameter for ips particle size
PMFS(IPS)	particle mass fraction (fraction of sorbent mass) for ips particle size
LSPBUG	logical to specify intermediate debugging printout
LYPS	flag for specifiying particle starting locations
YPSH	normalized upper bound for particle starting locations (v/R)
YPSL	normalized lower bound for particle starting locations (v/R)
PRK(IPS)	turbulent Prandtl-Schmidt number for sorbent particles
NSUBSH	number of sorbent particle subshell (specified in PARAMETER.INC)
NSNODE	number of sorbent particle nodes (specified in PARAMETER.INC)
IORDER	order of sorbent particle reaction with respect to SO_2 (assigned in *sulfat.F*) iorder = 1; first order reaction iorder = 2; half order reaction

considered. The major concern is the added complexity of the mathematical formulation and the corresponding difficulty in obtaining numerical solutions. A simple sulfation delay mechanism based on temperature is also being considered to simulate the effects of calcination.

Sample Prediction - A hypothetical case for combustion of subbituminous coal was simulated to demonstrate the model. The case corresponds to the conditions of Asay (1982), although no sorbent was injected in the experiments. Figure II.G-4 shows the predicted particle trajectories for sorbents injected with the coal feed and the predicted effects of sorbent capture on SO_2 concentration at two aft locations for a Ca/S mole ratio of 2.2. The capture of SO_2 is evident.

The effect of Ca/S mole ratio was studied to determine if the submodel yields results consistent with experimental observations. Figure II.G-5 shows the scrbent submodel's predicted percent of SO_2 captured for Ca/S mole ratios ranging from 0.8 to 2.2. The predicted SO_2 capture is approximately linearly dependent on Ca/S mole ratio. Both the trend and the magnitude are in agreement with isothermal measurements and prediction of Newton et al. (1986).

Model Parameters - A literature review was conducted to identify values for physical and kinetics parameters for the sulfation model. Values currently identified are shown in Table II.G-4. The model shows varying degrees of sensitivity to each parameter. The greatest sensitivity is to changes in the sulfite product layer diffusion coefficient. Solid state diffusion appears to be the controlling resistance.

Fuel-Rich Conditions - A sulfation model for H_2S is needed to extend the submodel to fuel-rich applications. The controlling resistances in the particle must be examined and intrinsic reaction rates must be correlated. There is a general lack of information in the open literature to elucidate the H_2S capture rates and important physical processes. Experimental data are currently being sought in the open literature to complete this objective.

Plans

During the upcoming quarter, an examination of the sorbent capture submodel will continue. The parameters and stream variables listed in Table II.G-5 will be examined to demonstrate the utility of the model. The predictions will be compared to published results.

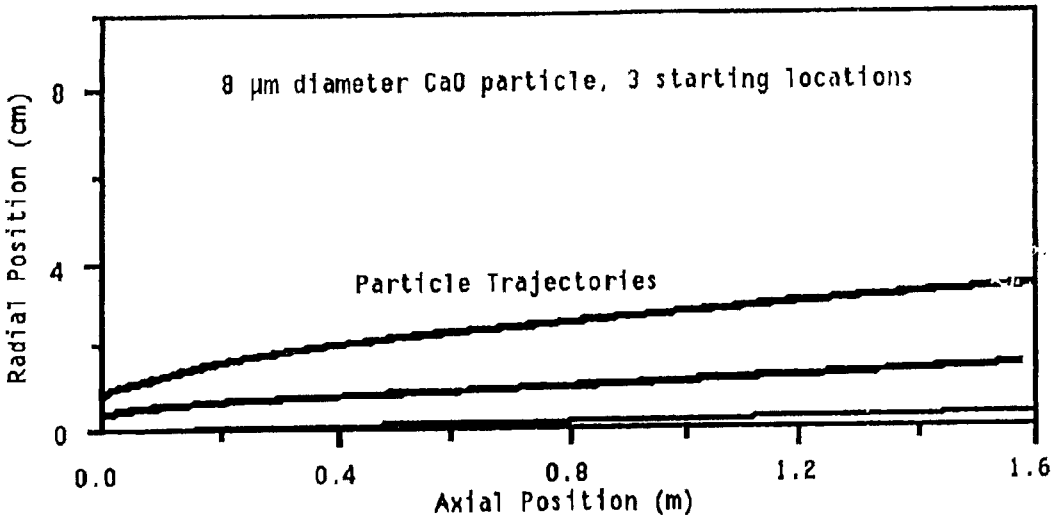

Ca/S mole ratio = 2.2
BET surface area = 100 m^2/g
Sorbent particle diameter = 8 μm

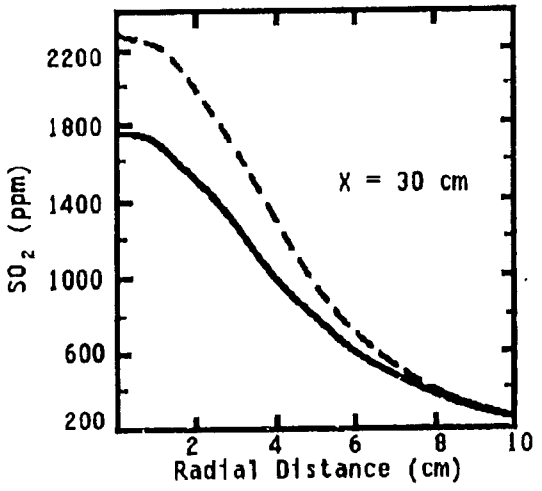

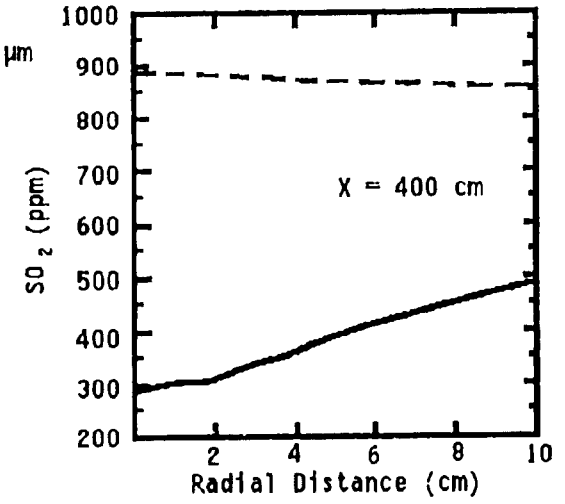

Figure II.G-4. Predicted sorbent particle trajectories and SO_2 concentration radial profiles near the burner (30 cm) and at the reactor exit (400 cm) for combustion of Wyoming subbituminous coal (1:10 sorbent/coal feed)

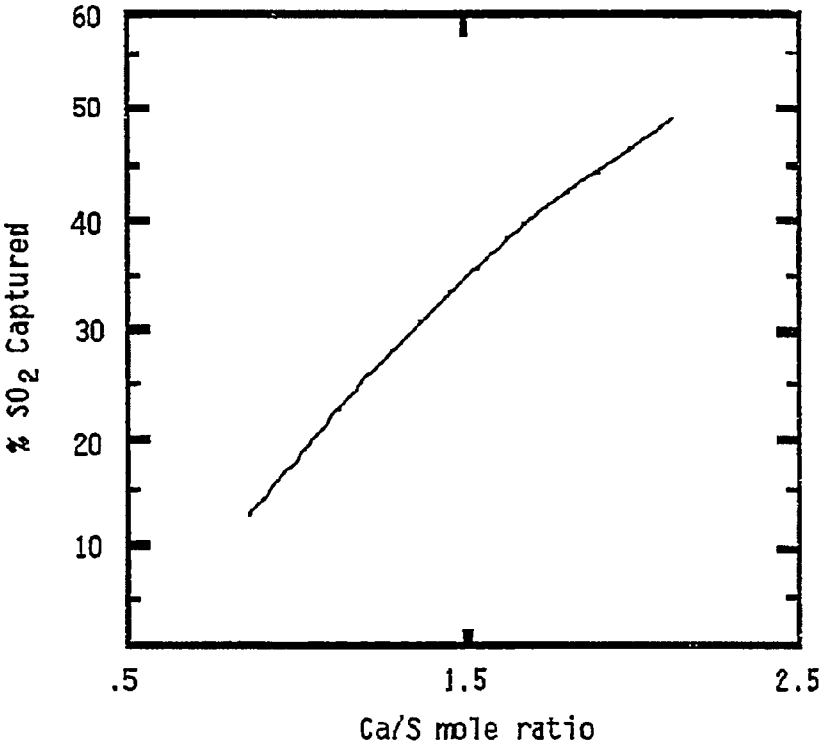

Figure II.G-5. Predicted effect of Ca/S mole ratio on SO_2 capture for combustion of Wyoming subbituminous coal.

Bet surface area = 100 m^2/g, sorbent particle diameter = 8 μm

Table II.G-5. Parameters and Stream Variables to be Investigated with the Sorbent Capture Submodel

Parameter	Range of variable
BET surface area	10-100 m^2/g
sorbent particle diameter	2-40 μm
gas phase temperature	± 200 K (benchmark case)
SO_2 gas phase concentrations	± 1000 ppm (benchmark case)
particle injection location	primary and tertiary
kinetic parameters	
D_{sp}	(.01-100)*D_{sp} recommended
k_{first}	(0.1-100)*k_{first} recommended

Table II.G-4. Sulfation Submodel Parameters

Parameter	Value[1]	Comments
BET Surface area	20 m^2/g	For calcined dolomite and/or hydrated lime
Particle diameter	8 μm[3]	Particle size for crushed dolomite or hydrated lime
Ca/S ratio	2.0 by mass[4]	Sorbent loading ratio
$D_{sp} = D_o exp(-E/RT)$		Product layer diffusivity
D_o	0.36	For all T
E	5.1 kcal[5]	For $T < 775$ K
	33 kcal	For $T \geq 775$ K
$k = k_o exp(-E/RT)$	$291exp(-7510/T)$[6]	Sulfation reaction rate constant correlated to experimental data
Particle void	0.54[7]	Typical void for pure CaO caline
Sulfite product void	0.00[7]	Assumed value

[1]Values are chosen based on the references given in the footnotes.

[2]Haji-Sulaiman and Scaroni, 1991; Gullet and Bruce, 1987; Newton et al., 1986; Borgwardt et al., 1987; Borgwardt and Bruce, 1986; Davini et al., 1991.

[3]Gullet and Bruce, 1987; Borgwardt et al., 1987; Borgwardt and Bruce, 1986.

[4]Newton et al., 1986.

[5]Gopalakrishnan and Seehra, 1990; Kocaefe et al., 1987; Borgwardt et al., 1987.

[6]Gorgwardt and Bruce, 1986.

[7]Davini et al., 1991.